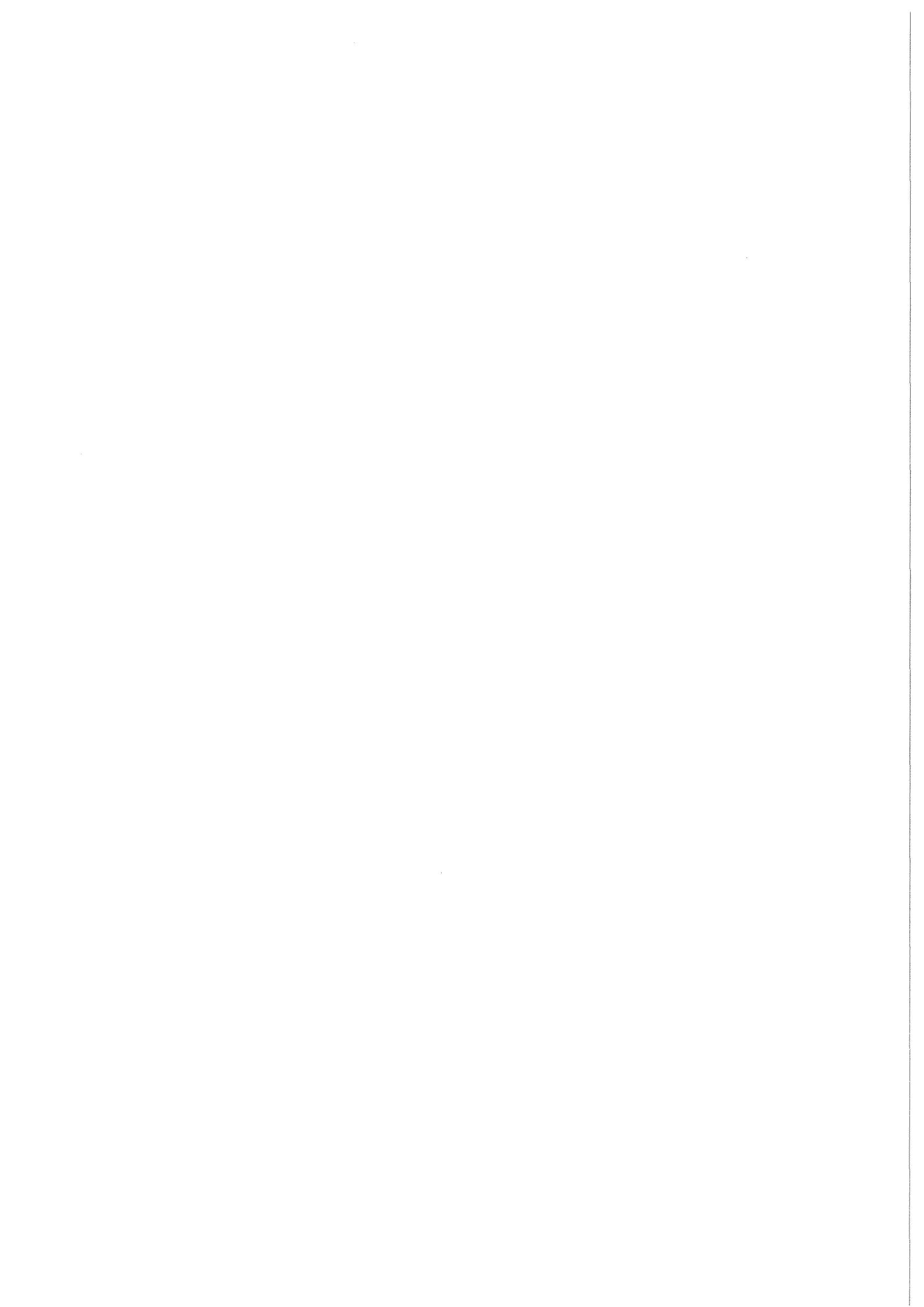


KfK 4601
August 1989

Epitaxial Growth and Properties of YBaCuO Thin Films

J. Geerk, G. Linker, O. Meyer
Institut für Nukleare Festkörperphysik

Kernforschungszentrum Karlsruhe



KERNFORSCHUNGSZENTRUM KARLSRUHE

Institut für Nukleare Festkörperphysik

KfK 4601

**EPITAXIAL GROWTH AND PROPERTIES
OF YBaCuO THIN FILMS**

J. Geerk, G. Linker, and O. Meyer

Kernforschungszentrum Karlsruhe GmbH, Karlsruhe

Als Manuskript vervielfältigt
Für diesen Bericht behalten wir uns alle Rechte vor

Kernforschungszentrum Karlsruhe GmbH
Postfach 3640, 7500 Karlsruhe 1

ISSN 0303-4003

ABSTRACT

The growth quality of YBaCuO thin films deposited by sputtering on different substrates (Al_2O_3 , MgO, SrTiO_3 , $\text{Zr}(\text{Y})\text{O}_2$) has been studied by X-ray diffraction and channeling experiments as a function of the deposition temperature. Besides the substrate orientation, the substrate temperature is the parameter determining whether films grow in c -, a -, (110) or mixed directions. Epitaxial growth correlates with high critical current values in the films of up to $5.5 \times 10^6 \text{ A/cm}^2$ at 77 K. Ultrathin films with thicknesses down to 2 nm were grown revealing three-dimensional superconducting behaviour. Films on (100) SrTiO_3 of 9 nm thickness and below are partially strained indicating commensurate growth. From the analysis of the surface disorder 1 displaced Ba atom per Ba_2Y row was obtained indicating that the disordered layer thickness is about 0.6 nm. Tunnel junctions fabricated on these films reveal gap-like structures near $\pm 16 \text{ mV}$ and $\pm 30 \text{ mV}$.

Epitaktisches Wachstum und Eigenschaften dünner Schichten des Hochtemperatur-Supraleiters YBaCuO

ZUSAMMENFASSUNG

Das Verfahren der Magnetron-Kathodenzerstäubung wurde zur Abscheidung dünner YBaCuO-Schichten auf verschiedenen Substraten (Al_2O_3 , MgO, SrTiO_3 , $\text{Zr}(\text{Y})\text{O}_2$) optimiert. Die Wachstumsrichtung und die kristalline Güte der Schichten wurde in Abhängigkeit von der Substrat-Oberflächengüte, der Orientierung und der Temperatur mittels Ionenchanneling und Röntgendiffraktion untersucht. Der Grad der Epitaxie und die Mosaik-Verbreiterung bestimmen den kritischen Transportstrom mit Werten bis zu $5.5 \cdot 10^6 \text{ A/cm}^2$ bei 77 K. Selbst in ultradünnen Schichten mit einer minimalen Dicke von bis zu 2 nm zeigt das supraleitende Verhalten 3-dimensionalen Charakter. Schichten auf (100) SrTiO_3 mit Dicken kleiner etwa 9 nm sind teilweise zur Unterlage verspannt, was auf kommensurables Wachstum hinweist. Die Channeling-Analyse der Schichtoberfläche ergibt in günstigen Fällen eine Verlagerung von nur 1 Ba-Atom pro Ba_2Y -Kette, was einer maximalen Dicke der gestörten Oberfläche von etwa 0.6 nm entspricht. Auf diesen Schichten präparierte Tunneldioden zeigen Strukturen mit einer Energielücke in der Nähe von $\pm 16 \text{ mV}$ und $\pm 30 \text{ mV}$.

LIST OF CONTENTS

1. INTRODUCTION	1
2. THIN FILM SYNTHESIS	5
2.1 The 3-step and the 2-step preparation procedure	5
2.2 Deposition apparatus for HTSC thin film preparation by the 2-step procedure	8
2.3 The preparation of HTSC thin films by inverted cylindrical magnetron sputtering	15
3. X-RAY DIFFRACTION ANALYSIS	22
3.1 Films on strontiumtitanate, SrTiO ₃	23
3.2 Films on (100)-magnesiumoxide, MgO	28
3.3 Films on yttrium stabilized zirconia, Zr(Y)O ₂	30
3.4 Films on sapphire, Al ₂ O ₃	32
3.5 Comparison of film growth on different substrates	34
3.6 Ultra-thin films	37
4. EPITAXIAL GROWTH ANALYSIS BY ION CHANNELING	39
4.1 Analysis concepts	40
4.1.1 Surface peak analysis	44
4.1.2 Disorder analysis	46
4.2 Substrate surface preparation and analysis	47
4.3 YBaCuO thin films: growth performance and disorder	52
4.4 Growth on strontiumtitanate, SrTiO ₃	53
4.5 Mosaic spread in films with polycrystalline fractions	56
4.6 Growth on (100) yttrium stabilized zirconia, Zr(Y)O ₂	57
4.7 Growth on (100) magnesiumoxide, MgO	59
4.8 Intrinsic defect structures	61
4.9 Disorder in the tetragonal phase	64
4.11 Misfit strain and misfit dislocations	68
4.12 Concluding remarks	71

5. SUPERCONDUCTING PROPERTIES	73
5.1 Transition temperatures and transport properties	73
5.2 Superconducting properties of ultrathin films	77
5.3 Electron tunneling	79
REFERENCES	90

1. INTRODUCTION

In the past thin films have played an important role in superconductivity research from the basic and applied point of view. In this regard the relations of important length parameters such as the penetration depth of magnetic fields and the coherence length with film thickness are worth mentioning. Thus the behaviour of magnetic fields in thin films was used to study the consequences of nonlocal electrodynamics. Proximity effect experiments have been conducted on the diffusion of Cooper pairs from the superconductor to the normal metal considering the effects of film thickness and electron mean free path. Tunneling junctions are the most sensitive probe for the microscopic properties of superconductors. The problems of material synthesis and surface quality for the preparation of tunneling junctions were solved by preparing the superconductor in form of thin films under high or ultrahigh vacuum conditions. The films were deposited onto heated substrates such that they grew up in the correct crystalline structure. Josephson junction devices are produced applying thin films. Such devices have been used for circuit applications in RF signal generation for electromagnetic wave detection and mixing, parametric amplification and frequency conversion, and in high sensitive magnetometry and switching.

An enhanced interest in thin films synthesis arose after the discovery of the high transition temperature superconducting oxides [1] when it was shown that in contrast to bulk material high critical current densities, J_c , are obtainable in thin films at the boiling point of liquid nitrogen [2]. It soon became apparent that high J_c values in the range of 10^6 A/cm² are closely related to the growth quality of the films. In general, it turned out that polycrystalline films in contrast to different structural classes of the "classical" superconductors revealed degraded normal-conducting and superconducting properties. This probably is due to a granular nature of such films where high T_c grains are surrounded by deteriorated material which may be oxygen deficient. Films having such an inhomogeneous structure are also less suited for basic research experiments, like, e.g. for irradiation studies where the investigation of defect structures is of interest, or for application in electronic device technology where high potentialities are expected for the use of the new oxide superconductors. Therefore all attempts in thin film preparation concentrated on the deposition of highly oriented, textured films with the aim to achieve single crystalline growth in order to fulfill all the requirements imposed by special needs.

Quite a number of different deposition techniques has been applied for the preparation of thin films of the superconducting oxides. For basic studies of the

epitaxial growth a reliable and reproducible technique is required such that the structure and the properties of the films can be studied as a function of the deposition parameters which are essential for epitaxial growth. Besides the deposition parameters the choice of the substrate material is important for growth studies for two reasons: first, at the substrate temperatures applied during deposition, substrate-film reactions should be avoided, and second, a good lattice matching between the growing film and the substrate surface which is beneficial for epitaxial growth should be achieved. A high quality substrate surface finish is another prerequisite for epitaxial growth.

Different methods may be applied for the structural characterization of the growth quality of epitaxial films. With respect to diffraction methods X-ray diffraction is most commonly used as a fast and simple technique because the use of reflection geometries does not require special sample preparation. The growth direction of films, the mosaic spread or admixtures of grains with different crystallographic orientations are easily determined from diffraction experiments. The drawback of X-ray measurements is their relative insensitivity to intrinsic defects and the lack of depth resolution. These drawbacks are compensated by ion channeling combined with Rutherford backscattering or nuclear reactions. This technique is not only very sensitive to intrinsic deviations from perfect growth but also provides depth resolution allowing special studies of interface or surface effects. A very powerful technique for the growth characterization also is high resolution electron microscopy which, however, needs special sample preparation and therefore cannot be applied nondestructively.

Though basic studies of epitaxial film growth are of interest in itself the large activity in the investigation of the perovskite-structure like oxide films doubtless is due to the fact that high transition temperature superconductivity occurs in this class of materials. It is therefore of interest to correlate the conducting and superconducting properties like the transition temperature or the critical current density with the growth quality. Such relations naturally can be only of qualitative nature, but if they exist they may provide direct hints how to proceed in the preparation process for property improvement or may explain either degraded or improved properties by special growth appearance. In addition to the interest in relationships between growth and properties a complete characterization of films is also an important requirement for the reliability of the results of further physical investigations using such films. A large number of publications describing the preparation, characterization and the properties of thin films of high T_c oxides like LaSrCuO, 1-2-3 compounds, Bi- and Tl-

compounds has appeared in the literature. Most of the work had concentrated on the investigation of the 1-2-3 compound $\text{YBa}_2\text{Cu}_3\text{O}_7$.

In this paper we review the results of preparation and investigation of $\text{YBa}_2\text{Cu}_3\text{O}_7$ films elaborated in the thin film group at the INFP of the Kernforschungszentrum Karlsruhe. We have used single target inverted cylindrical magnetron sputtering for film preparation which turned out as a very reliable technique delivering high quality films in a 2-step preparation procedure. Details of the deposition apparatus, of the deposition technique and sample preparation in comparison to other preparation procedures are presented in chapter 2 of this review.

The substrate temperature, T_s , during deposition was one of the most important parameters determining the growth and the properties of the films. We have deposited films at different T_s on the commonly used single crystalline substrates like Al_2O_3 , MgO , Si , SrTiO_3 , ZrO_2 . The structure of the films vs. T_s was mainly studied by X-ray diffraction. These data are presented in chapter 3 after a short description of the methods applied. Highly textured growth has been observed on Al_2O_3 , MgO , SrTiO_3 , ZrO_2 . On Si so far only polycrystalline growth ($T_{c0} = 86 \text{ K}$) occurred which will not be discussed in this review.

A detailed analysis of the epitaxial growth by ion channeling of films deposited on (100) oriented MgO , SrTiO_3 and ZrO_2 substrates at optimized deposition conditions is described in chapter 4. This chapter also includes the analytical concepts of ion channeling, the experimental determination of the quality of substrate surface finish and deals with special effects occurring at the substrate-film interface and at the film surfaces.

In the last chapter 5 we discuss the properties of the films on different substrates as a function of the deposition temperature. This allows a comparison with the X-ray results and in some cases may explain the behaviour of the transition temperature or transport properties at different T_s . The chapter includes results obtained for ultrathin films with thicknesses down to 2 nm (standard thickness was 300 nm). It concludes with tunneling data from SNS junctions where the junction preparation profited from the reliable and controllable film deposition. We should remark that the results presented in this review reflect the present status of investigation in our group. Excellent films could be produced also by other methods like laser ablation [3]. Intensive research in this area proceeds very fast. A variety of other substrate materials especially with respect to good lattice matching or to practical applications is under investigation. The lowering of the maximum temperature applied in the

preparation process and the achievement of smooth surfaces is an ambitious goal similar to the preparation of heterostructures which are attempted not only in the 1-2-3 compounds like YBaCuO but also in the other high T_c compounds. In this respect our data represent the status of investigation just at the beginning of a development of epitaxial film growth in a new class of materials.

2. THIN FILM SYNTHESIS

The synthesis of thin films of high T_c superconductors (HTSC) generally involves problems which only in rare cases (e.g. in the case of Chevrel phases) had to be encountered before in the class of traditional superconductors. The first problem is the high number of metallic constituents which have to be deposited at well controlled rates. For the 1-2-3 materials these are 3 elements like Y, Ba and Cu; for the layered compounds exceeding a superconducting transition temperature of 100 K these are 4 or even 5 elements like in the case of the Bi-Pb-Sr-Ca-Cu oxides. The second severe problem mainly arises if the experimenter desires to grow films directly in the correct structure at elevated substrate temperature. We shall discuss below, that this process usually is the most effective one for thin film preparation. In this case a partial pressure of oxygen has to be maintained at the film surface during growth. It has to be high enough to allow the existence of the desired perovskite like structure at the applied substrate temperature. These oxygen partial pressures have been recently determined by Bormann and Nölting [4] to be in the region of about 10^{-2} Torr and are thus in strong contrast to the high vacuum conditions necessary for the reliable operation of many of the thin film deposition equipments used for conventional superconductors (e.g. mass spectrometer controlled electron beam deposition). In the following we will first discuss the procedures of HTSC thin film preparation, then we will point out the importance of the direct growth process and finally, after discussion of the possible technical solutions for the above problems, we will present a simple deposition device, based on the sputter deposition method, which allows the reliable direct growth at least for the HTSC of the 1-2-3 family.

2.1 The 3-step and the 2-step preparation procedure

Immediately after the discovery of the HTSC oxides and the announcement of their composition and structure many groups (most of them were involved before in thin film research of the conventional superconductors) switched their research and development efforts towards these new exciting materials. The first success for thin film preparation of the HTSC of the La-Ba(Sr)-Cu-O and the Y-Ba-Cu-O groups of materials was achieved by such groups (e.g. IBM, Stanford, AT&T Bell, KfK) applying a procedure which formally included 3 preparation steps. The

upper part of Fig. 2.1 demonstrates this 3-step procedure in the form of a sample temperature versus time diagram. In the first step the metallic elements (e.g. Y, Ba, Cu) are codeposited at the correct concentration ratios usually by rate controlled multi source deposition. The substrate temperature is kept below 400°C such that the material condenses on the substrate in the amorphous state. It was found to be favourable if some oxygen is already incorporated into the film at this stage. This was achieved by keeping an oxygen pressure of 10^{-5} Torr in the vacuum chamber during deposition, which is low enough not to affect the function of the sources and the rate control system. After deposition the samples were removed from the system and underwent a heat treatment in a suitable oven at an oxygen partial pressure of about one atmosphere. As indicated in Fig. 2.1 the samples were first heated to temperatures near 900°C to convert the film structure from the amorphous to the perovskite like one. At this high formation temperature and at an oxygen pressure of 1 atmosphere the films usually attain a perovskite-like structure strongly related to the desired one but with a high degree of oxygen deficiency, e.g. in the case of the orthorhombic $Y_1Ba_2Cu_3O_7$ superconductor the material is tetragonal with a composition of $Y_1Ba_2Cu_3O_6$. The missing oxygen is taken up by the sample in the course of a third preparation step which is a heat treatment at lower temperatures, e.g. 400°C, at the same oxygen pressure. Obviously, the oxygen take up can also be accomplished by cooling the sample from the formation temperature down to RT slowly enough (e.g. within 0.5 h, dashed line). Summarizing, this 3-step procedure consists of the deposition-, the formation- and the oxygen intercalation step. Using the 3-step procedure the group at IBM followed by the Stanford group could prepare epitaxial films of the 1-2-3 material and demonstrate their sensational high critical currents [2]. The quick success of these groups mainly relied on one advantage of the 3-step procedure that is the low oxygen partial pressure required during deposition. Thus any state of the art multiple source deposition system could be used without considerable technical alterations. The severe drawback of the 3-step procedure is the high formation temperature during the second step, which favours severe reactions of the films with the substrate materials and thus generally excludes many substrates, like Si or Al_2O_3 , which may become important for future technical applications. Another disadvantage is that a formation starting from an amorphous state usually is an unfavorable process for epitaxial growth as crystallites possibly start growing throughout the film with random orientations and not only in the desired directed growth at the film substrate interface.

From the many years of experience in semiconductor as well as superconductor thin film synthesis it is well known, that optimum films are obtained if the deposition parameters, mainly the substrate temperature and the partial pressure of possible gaseous constituents of the compound to be synthesized, are adjusted such that the desired compound grows up already during deposition. Prominent examples of the past were the conventional superconductors Nb_3Sn ,

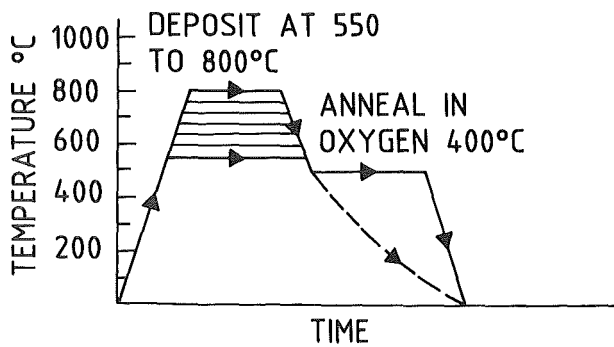
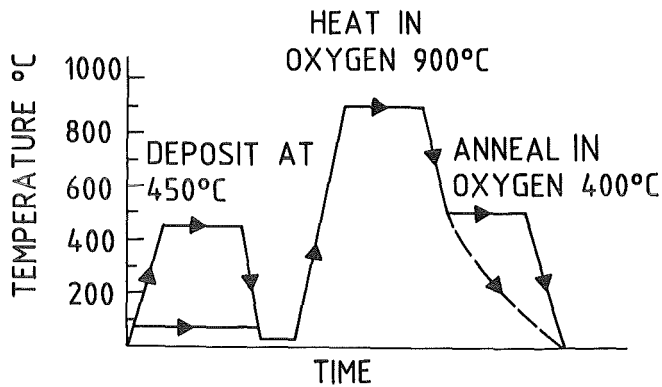


Fig. 2.1

Heat treatments for the formation of $YBaCuO$ thin films.

Upper: The sample is deposited in the amorphous state at temperatures $\leq 450^\circ C$ and has to be converted to the desired crystalline perovskite like structure by a subsequent high temperature treatment followed by a low temperature treatment to obtain full stoichiometry with respect to the oxygen content (3-step procedure).

Lower: The sample is deposited at an elevated substrate temperature in an oxygen atmosphere such that it grows in the perovskite-like structure. The last step again is a low temperature treatment to complete the oxygen stoichiometry (2-step procedure, in-situ process, direct production).

V_3Si , YB_6 , and Nb_3Ge . The latter case was the record holder concerning the transition temperature till the discovery of the copper oxide materials and could only be synthesized in this way. The HT superconductors contain a gaseous element, oxygen, in their structure and a certain partial pressure of this element has to be maintained during deposition in the vicinity of the substrates. The required substrate temperatures so far are known to be in the region of $650^\circ C$ till $750^\circ C$. For the deposition of the 1-2-3 material $YBa_2Cu_3O_x$ ($x=7$) at these temperatures the oxygen partial pressure should be higher than 1000

atmospheres as one can extrapolate from data of Kishio et al. [5] who determined the correlation between composition and oxygen partial pressure of this compound. Except for the case of the chemical vapor deposition method the actual deposition processes, however, require pressures below 1 Torr, because fortunately, in this parameter field of temperature and pressure the interesting perovskite like materials are still existent but with a reduced oxygen content, e.g. $x=6$ and correspondingly small changes in lattice parameter and structure [4]. Therefore, the preparation procedure for the crystalline growth during deposition consists of 2 steps of sample treatment which are illustrated in the lower part of Fig. 2.1. Following the deposition step at say 700°C the sample undergoes an intercalation step at lower temperatures which is essentially identical to the third step of the 3 step method. Also here some experimenters accomplish the second step by slowly cooling the sample in the sputter gas or at somewhat higher oxygen pressure which leads essentially to the same results. Probably in the rush for new exciting results and processes some experimenters claim that they do not need a second step. This is misleading in so far as a true 1-step procedure implies that the films grow up at elevated temperatures with the correct stoichiometry ($x=7$). For the substrate temperatures usually applied this requires the extreme high pressure conditions specified above. For the low pressures (1 Torr or lower) enforced by the common deposition techniques substrate temperatures should not exceed 350°C following again the data of Kishio et al. [5]. But at such low temperatures the HTSC oxides grow up in the amorphous structure and not in the perovskite-like one. Thus the present deposition techniques do not allow the direct growth of the 1-2-3 materials with correct oxygen stoichiometry and a second preparation step for oxygen intercalation is in principle always necessary. In the literature on conventional thin film growth, for the direct growth at elevated substrate temperatures there was no specific expression in use to characterize this type of preparation procedure. In the case of HTSC thin films many different terms such as "in situ preparation, direct growth, direct production, low temperature process, 2-step procedure" are used by the authors to distinguish this procedure from the 3-step process. In this paper we will stick in the following to the designation "2-step procedure".

2.2 Deposition apparatus for HTSC thin film preparation by the 2-step procedure

In Fig. 2.2 we illustrate four examples of thin film deposition devices in use today for the preparation of the 1-2-3 material. In all four cases the substrate

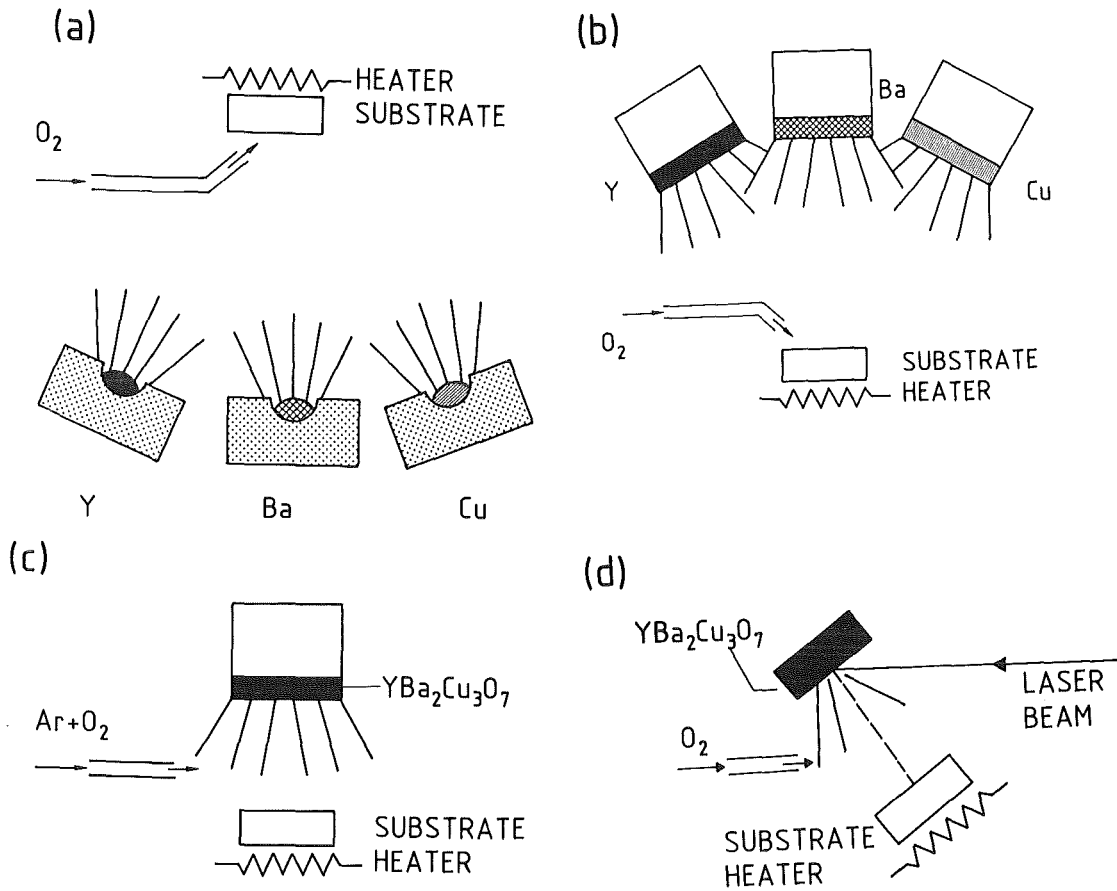


Fig. 2.2 Schematic illustration of the different technical possibilities of in-situ preparation of YBaCuO films.

- Evaporation of the metallic constituents from independent sources, e.g. electron-guns or crucibles
- Sputtering of the metallic constituents from independent sputter targets.
- Single target deposition using a sputter gun with a composite target.
- Single target deposition by an ablation process generated by a pulsed laser or particle beam.

temperature is achieved by an external heater. Fig. 2.2a shows schematically the evaporation from 3 sources. Usually, e-beam guns with independent rate control and feedback are used [6]. Severe technical difficulties arise by the high oxygen partial pressure which is maintained via a gas inlet tube placed near the substrates. It causes an increase of O_2 -pressure in the whole vacuum system depending on gas flux dynamics and pumping speeds. Thus it affects the function of the e-beam guns by arcing and by oxidation of the e-beam cathodes. Furthermore, a high O_2 -pressure may severely disturb rate control systems such as quadrupole mass spectrometers or oscillating crystal monitors. A common technical solution to these problems is additional differential pumping on the rate monitors and the e-beam sources. New developments are, e.g. rate control

systems which work at high oxygen partial pressures such as light absorption rate control or the economizing of the oxygen supply by offering it to the film surface in a highly reactive form [6]. This can be done, e.g. by an RF field maintained near the substrates [7] by passing the oxygen through a microwave cavity or by replacing the oxygen by ozone [8]. These examples show that in any case the rate controlled e-gun systems which were often used before for deposition of films like $Nb_3(GeAl)$ or other compound systems have to be equipped with additional technical means if HTSC films shall be prepared in the 2-step process. On the one hand this offers to the experimenter the fascinating opportunity to study the growth of these materials in dependence of all possible physical parameters. On the other hand, these machines attain such a high degree of complication, that at present we are aware of only a few cases where they work reliably. A very interesting simplification of the 3 source evaporation type of machine has been published by Berberich et al. [9]. These authors successfully operate a system where the 3 elements Y, Ba and Cu are evaporated from simple metallic boats regulated by feedback from oscillating crystal monitors. These boats are heated ohmically and operate with a much slower and less sophisticated feedback control. Thus they are much less susceptible to high oxygen partial pressure than e-guns.

The best rate control is offered by the sputter deposition method. If non-reactive gases are used then the deposition rate of a sputter gun is almost proportional to the power spent into the electrical discharge and no feedback loop is needed to control the gun during a deposition run. Thus a multi source sputter deposition system as illustrated in Fig. 2.2b represents a remarkable simplification compared to the multi source evaporator. Its severe drawback on the other hand arises when reactive gases like oxygen are fed into the system. At an oxygen partial pressure as low as 10^{-4} Torr the target surfaces of the Ba and Y sources already start to oxidize and the sputter coefficient may change (usually decrease) by orders of magnitude, depending on the ratio of power and the oxygen partial pressure. These changes differ from one material to the other so the addition of oxygen results in an almost uncontrollable influence on the relative deposition rates. Possible counter measures are again a strong differential pumping in the vicinity of the substrates. An interesting variation of the multi source sputtering of the 1-2-3 material is a two sputtergun system with the application of the alloy targets YCu and BaCu [10]. These alloys are less reactive than the pure elements Y and Ba and thus may also be less sensitive in their relative change of deposition ratio if oxygen is fed into the system.

Fig. 2.2c shows the presumably most simple solution of the HTSC deposition problem, the sputtering from a single target which contains all the elements needed in a film. As pointed out in many publications [11] sputtering from an alloy or compound target results (after a short period of presputtering for "conditioning" of the target surface) in a flux of sputtered material which contains the elements in the same ratio as the bulk of the target. The target then in principle can be manufactured from an alloy of the metallic constituents, e.g. $Y_1Ba_2Cu_3$ or from the complete superconductor material in form of a ceramic target. The alloy target is preferable due to its much higher sputtering rate. Unfortunately, the 1-2-3 alloy seems not to form at least with Y as the rare earth component. So the usual choice is the ceramic target. In this case besides the reduced sputter coefficient difficulties may arise due to its low heat conductivity. Care has to be taken not to overheat the target surface as the ceramic material easily decomposes into non-electrical conducting oxides.

The most severe problem of sputtering from an oxide target or from a metallic target in an oxygen atmosphere is illustrated in Fig. 2.3. The figure shows the lateral distributions of Y, Ba and Cu resulting from sputter deposition on substrates facing the ceramic sputter cathode in the usual way. We see strong deviations from stoichiometry on most of the substrate area, which contradicts our statement from above concerning the similarity of the target composition and that of the sputtered particle flux. One observes further in Fig. 2.3 that especially

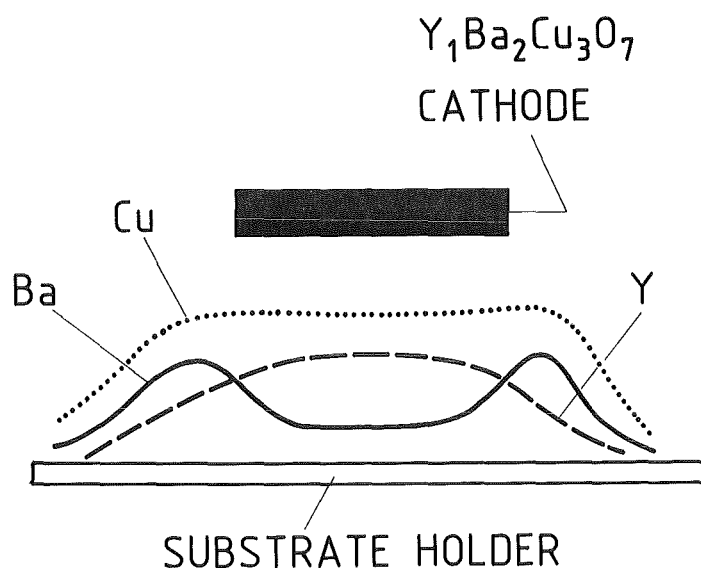


Fig. 2.3 Typical lateral distributions of the elements Y, Ba and Cu in a sputter deposition experiment using an oxide target and pressures below 0.02 Torr.

the Ba distribution correlates with the target geometry in the way that it seems to be pushed away from the area which directly faces the cathode . From the sputter deposition of other oxides the reason for these peculiar elemental distributions is well known. It is due to a bombardment effect of the substrates during deposition by negatively charged particles emerging from the cathode [12] . Such particles (e.g. O^- , O_2^- , BaO^-) are generated at the surface of the cathode simply due to the fact that many of the sputtered species containing oxygen leave the cathode surface in a negatively charged state due to their strong electronegativity. A more detailed investigation by Plog and Gerhard [13] shows that a sputtered cluster or molecule is in principle neutral directly after its generation but on leaving the surface potential it splits into a positively and a negatively charged radical. The negatively charged species then are accelerated away from the cathode by the voltage gap of the cathode dark space in the sputtering discharge. In other words: The negative ions bombard the film surface with the same energy as the argon ions bombard the target surface. Thus it is often observed, that during sputtering of oxides the substrates are strongly etched on their surface instead of being covered with a film. The most simple and obvious possibility to reduce the bombardment effects is to increase the pressure of the sputtering gas. In Fig. 2.4 we show data which represent an extrapolation to high pressures of data published by Westwood [11]. The data provide a hint for the sputtering gas pressures needed to thermalize energetic particles within a given distance which for our problem is the distance between the target and the film surface. We see that for distances in the regime of 1-3 cm the pressure should exceed 10^{-1} Torr to ensure complete thermalization of fast particles. The data of Fig. 2.3 were taken from samples deposited at 2×10^{-2} Torr of an argon-oxygen mixture. When the substrates were held at room temperature during deposition, substrate etching effects were not very pronounced. The distribution of the 3 metallic elements was almost homogeneous and the film composition was nearly stoichiometric . The strong deviations from stoichiometry as illustrated in Fig. 2.3 were only found for films deposited at substrate temperatures above $400^\circ C$. We believe that these effects are still caused by particle bombardment. Though the particles are slowed down to prevent direct sputtering at the film surface, at high substrate temperatures they may still cause effects like radiation enhanced surface diffusion of certain elements (in our case of Ba). When we used planar magnetron sputtering devices at even higher pressures (4×10^{-1} Torr Ar + 2×10^{-1} Torr O_2) we still observed redistribution effects at substrate positions directly facing the plasma ring as indicated in Fig. 2.5. In this region the bombardment effects are most pronounced.

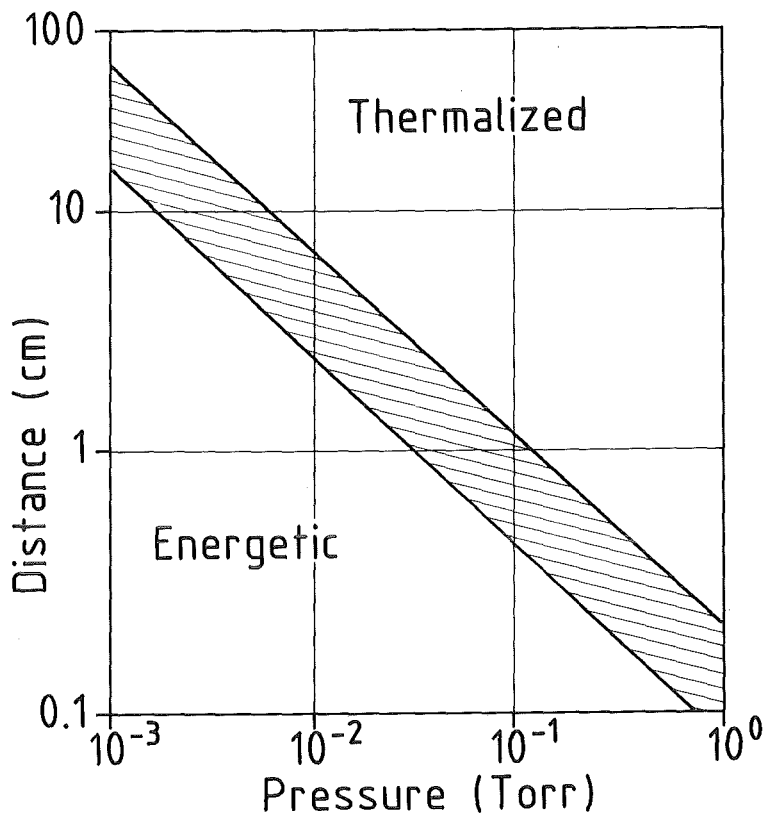


Fig. 2.4 Cathode-substrate distance vers. pressure diagram describing the conditions in a sputter deposition experiment with strong bombardment of the substrates (energetic) and with fast particles emerging from the cathode being thermalized before reaching the substrates.

From these findings obviously another kind of countermeasure of the bombardment problem can be deduced and that is a proper choice of the substrate position. More strictly speaking the substrate position is optimum at locations where the ratio of bombardment rate and deposition rate is minimized. For the planar magnetron many experimenters found these positions to be in the center of the plasma ring with the substrates facing the target plane. Another possibility is to place the substrates outside the plasma ring at a suitable angle to maximize the deposition rate (Fig. 2.5) [14]. A geometry related to the latter case is the sputtering from two opposed planar targets with the substrates placed outside the region between the targets [15]. In this case the negative particles from one target are sputtering the opposite one and thus at least at very low pressures may increase the deposition rate. It should be noted, however, that the negative particles if they would keep their charge could not surmount the potential well at the opposing cathode. But on their way through the discharge gas they easily are

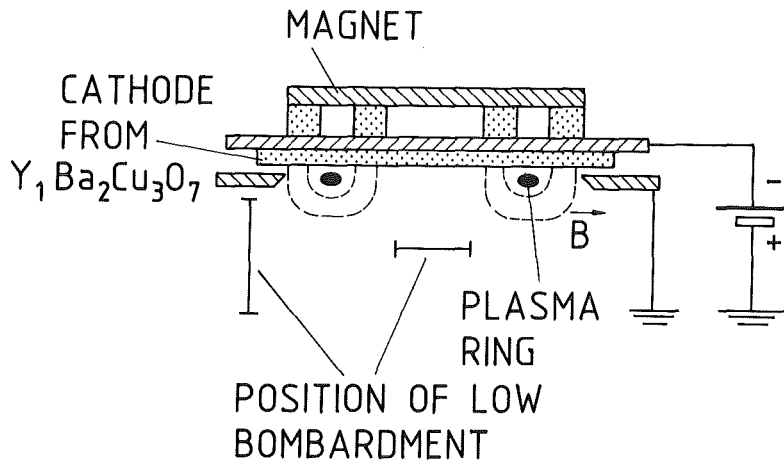


Fig. 2.5 Favorable substrate locations of low negative ion bombardment rate for planar magnetron deposition of films from a composite oxide target.

neutralized by stripping and they proceed as neutral particles which are no longer influenced by electric or magnetic fields. The natural extension of this geometrical solution is to place many opposing targets on a circle. The result is a tube like target and the corresponding sputter geometry is called "hollow cathode" or, if a magnetic field is used to increase the sputtering rate, the "Inverted Cylindrical Magnetron" (ICM). The preparation of HTSC thin films using an ICM device is described in the next section.

Fig. 2.2d illustrates the principle of HTSC thin film preparation by ablation of ceramic targets using pulsed beams of energetic particles. So far it turned out that UV laser pulses are very well suited for such purposes. After it was first demonstrated by Dijkkamp et al. [3] that this deposition method yields good films of the 1-2-3 material in the 2-step procedure at surprisingly low substrate temperatures near 650°C, many laboratories adopted this method for routine HTSC film preparation. Usually an excimer laser of the rare gas-fluoride type generates the laser pulses at rates between 1 and 50 pulses/second. The UV beam is directed via a quartz window onto the ceramic sample placed in a deposition chamber. When the pulses of an energy density between 1 and 2 Joules/cm² and a length of 10-30 nsec hit the sample surface they cause an explosion like evaporation of a thin, e.g. 30 nm surface layer. This process is so fast and high energetic that the composition of the evaporated material is exactly reflecting the target composition and is not influenced by the strongly different vapor pressures

of the elements and their oxides. This is the important difference to the usual continuous evaporation with e-beam guns or by resistive heating from boats. The evaporation of a pellet of $Y_1Ba_2Cu_3O_7$, e.g. in an e-beam gun system results in a film containing almost no Y due to the much lower vapor pressure of Y and its oxides in an $Y_1Ba_2Cu_3O_x$ melt.

Most experimenters using the laser ablation method found that the proper positioning of the substrate with respect to the target is crucial for the film quality. The optimum position seems to be on the vertical of the target surface. The ablation of the target is accompanied by the formation of a brilliant elongated plume of plasma extending outward up to about 2 cm from the target surface. Concerning the optimum distance of the substrate from the target many groups report that this is in the plasma plume but very near to its end. Due to the dependence of the extension of the plasma plume on the pulse energy this implies for fixed geometry a strong dependence of film quality on the pulse energy which is indeed also reported by many groups. Thus a very reliable operation of the eximer laser is of importance for a successful preparation of films by ablation .

Recently an alternative approach to the laser ablation has been presented by Geerk et al. [16] . That is the ablation by a pulsed beam of electrons. Fig. 2.6 shows a sketch of the experimental setup. The electron pulses are generated by a pseudo spark source with a pulse energy of 20 kV, a peak current of 10 kA, and a pulse length of 30 nsec. The beam diameter is 2 mm. In the target chamber an oxygen partial pressure of 2×10^{-2} Torr can be maintained, higher oxygen partial pressures are possible by appropriate differential pumping. The results for films of the 1-2-3 material obtained so far are resistance zero points in the superconducting transitions near 86 K and critical current densities of 1×10^5 A/cm² at 77 K. These results together with the extreme simplicity of the apparatus compared to an eximer laser are encouraging enough to develop the ablation method with charged particle beams with more expenditure.

2.3 The preparation of HTSC thin films by inverted cylindrical magnetron sputtering

The inverted cylindrical sputtering device is shown schematically in Fig. 2.7. The sputtering target is a cylinder of $Y_1Ba_2Cu_3O_7$ sintered material prepared either by hot and high temperature pressing (made by HITEC Materials, Karlsruhe) or by drilling a suitable opening into a sintered disc. The sputter gun is mounted onto a turbomolecular pumped vacuum system. The gun is usually operated in the dc mode with a current of 0.5 A and a voltage of 110 V. For most depositions a mixture of Ar and O₂ was used with partial pressures of 4×10^{-1}

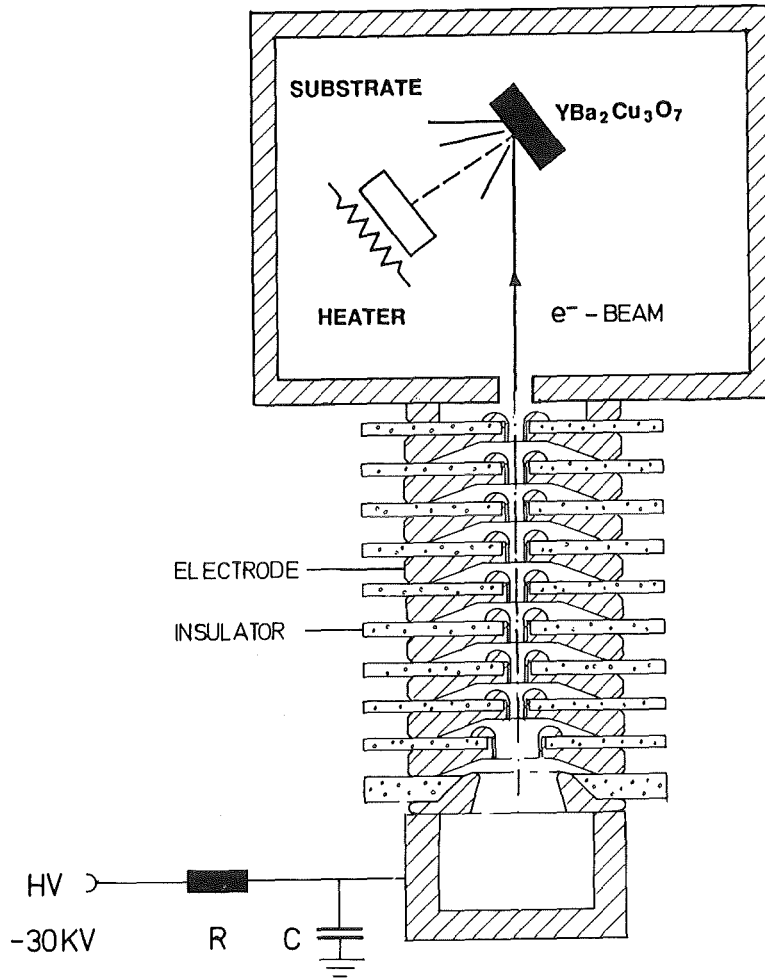


Fig. 2.6 Experimental set-up for the electron-beam ablation experiment.

Torr and 2×10^{-1} Torr, respectively. At this O_2 partial pressure the existence of the perovskite like structure extends up to temperatures of about 750°C following the data on the stability limit of the $YBaCuO$ 1-2-3 phase published by Bormann and Nölting [4]. The second preparation step was found not to be critical concerning the parameters temperature and pressure. The usual procedure is a treatment for 5-10 min in an oxygen atmosphere at pressures in the range of 0.1 to 1 atmosphere. In Fig. 2.8 we demonstrate the importance of the second step. The figure shows the resistance vs. temperature data of a film prepared on (100) $SrTiO_3$ at optimum sputtering conditions which are described in more detail below. After deposition this film was cooled down in the sputtering gas to room temperature (RT) as fast as possible (within 2 min) to prevent any significant oxygen incorporation even at the low oxygen partial pressure of 2×10^{-1} Torr. We see in Fig. 2.8 that the as-deposited film becomes superconducting near 50 K.

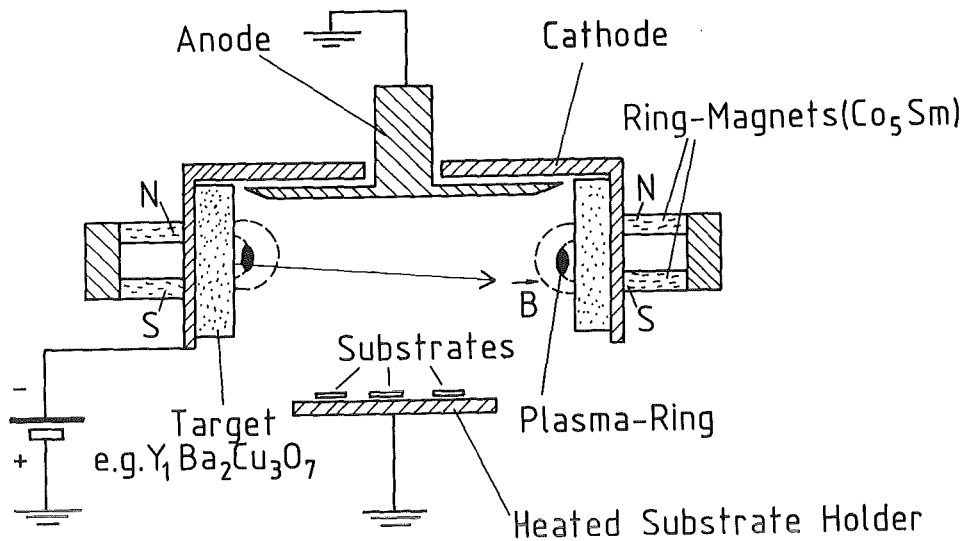


Fig. 2.7 Schematic cross sectional view of the cathode, magnets and substrates arrangement in the inverted cylindrical magnetron sputtering apparatus.

The insert of Fig. 2.8 shows transition curves measured by an inductive method. In this case the film is placed between two coils, a generator and a sensor coil, which act as a transformer. The film is intended to function as a shield between the coils, and in the superconducting state, the shielding currents prevent the transfer of signals from the generator to the sensor coil. The strength of the shielding currents of a film present a better measure of the average superconducting transition of the film material than the resistive transition which often detects only the properties of the best grains in a film. The inductive transition in Fig. 2.8 suggests that a significant part of the as-deposited film is superconducting with a transition near 40 K. After the second preparation step the film resistivity drops by a factor of 10 and the superconducting transition becomes sharp with a zero resistance value at 90 K. The inductive transition now occurs also at 90 K. It is interesting to note that the temperature-dependent resistance behavior is more metallic-like for the oxygen deficient as-deposited film. So far in the literature a semimetallic resistance behavior often is correlated with poor superconducting properties. From our results one can conclude that the resistance versus temperature behavior in terms of a more or less metallic one is not necessarily related to high or low T_c values. To finish the data on the second preparation step we illustrate in Fig. 2.9 how fast a film takes up the oxygen at 450°C. In this experiment we monitor the resistance of a YBaCuO film of about 500 nm thickness versus time. The film is oxygen deficient

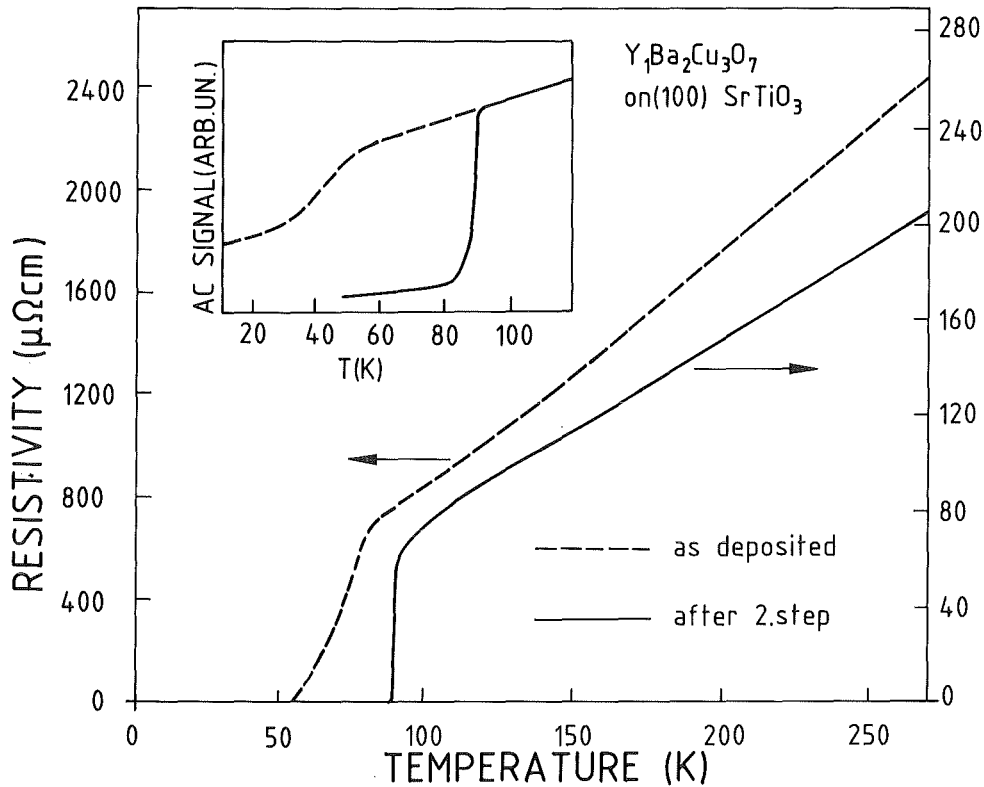


Fig. 2.8 Resistivity vs. temperature curves of an YBaCuO film on (100) SrTiO₃ after deposition (broken line) and after additional treatment in oxygen atmosphere (solid line). The corresponding ac signal vs. temperature curves are shown in the inset of the figure.

and it is first hold at 10^{-3} Torr at 450°C . Then at $t=0$ the vacuum vessel is vented with oxygen up to a pressure of 1 atmosphere within 15 sec. We observe that the resistance of the film quickly decreases indicating oxygen take up reaching the equilibrium state after about 2 min. Therefore typical treatment times for the intercalation step should be in the region of a few minutes.

All the films whose properties are described below were treated in the second preparation step. It was found that the most important parameter for the deposition experiment was the substrate temperature, T_s , during deposition. The heating of the substrates was accomplished by a stainless steel band wrapped around the substrates such, that it also covered partly the substrate surface. This band was heated by passing a current through it. A thermocouple was placed on the backside of the substrates between the substrate and the heating band. Thus the thermocouple measures a temperature somewhere between that of the substrate surface and the stainless steel heater. This simple type of heating and temperature detection has been used earlier at Bell Laboratories [17] for thin film deposition of conventional superconductors and it turned out to be very reliable.

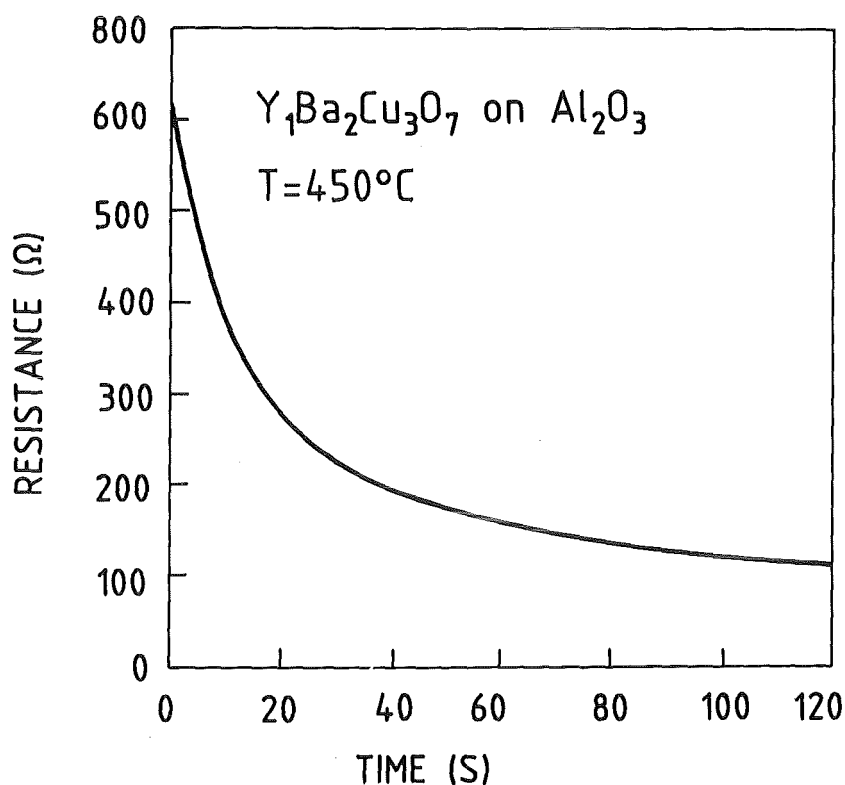


Fig. 2.9 Resistance change vs. time of an oxygen deficient YBaCuO film exposed to an oxygen atmosphere of 400 Torr at a temperature of 450°C starting at time 0.

When the substrate temperature was additionally controlled, e.g. by pyrometric methods the result was that near 800°C the thermocouple reading was about 50°C too high. The substrate temperatures given in the following are corrected according to this calibration.

In Fig. 2.10 we present the influence of the substrate temperature on the superconducting transition for films deposited on randomly oriented sapphire substrates. We observe (upper diagram) that the temperature range between 800°C and 850°C provides an optimum superconducting transition for an oxygen partial pressure of 2×10^{-1} Torr, i.e., the highest pressure we could maintain in our deposition system. Fig. 2.10 further demonstrates the changes in the optimum deposition temperature if the oxygen partial pressure (adjusted by a needle valve before the discharge is switched on) is lowered. The data of the lower diagram were obtained with the oxygen valve closed relying only on the oxygen partial pressure supplied by sputtering from the oxide target. From pumping speeds and the erosion rates we estimate this pressure to be near 10^{-3} Torr. Comparing the three diagrams we see that with decreasing oxygen partial

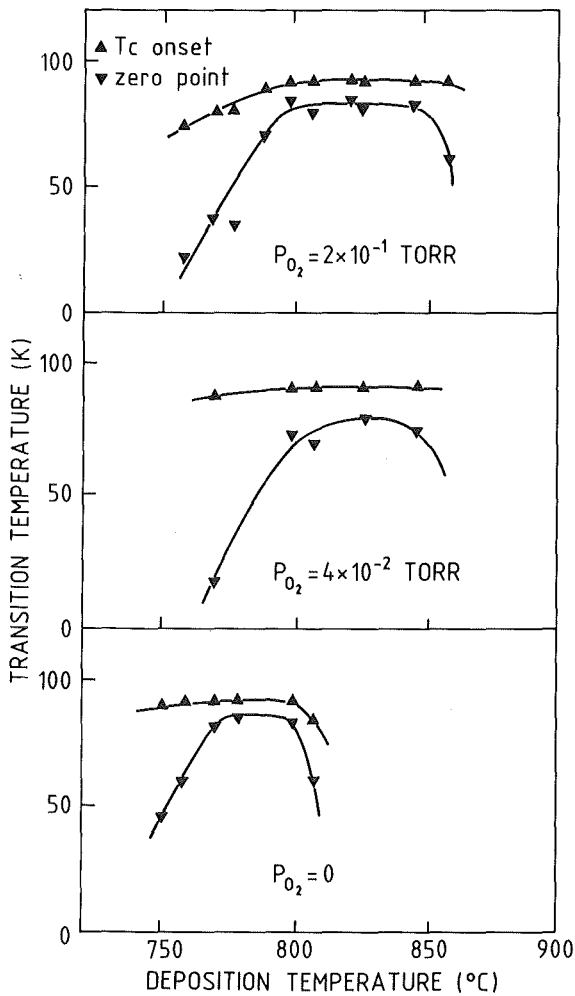


Fig. 2.10
The influence of the deposition temperature, T_s , and the oxygen partial pressure, p_{O_2} , in the first deposition step on the superconducting transitions of YBaCuO films deposited on sapphire substrates. Shown are the T_c onsets and zero resistance values.

pressure the temperature region for optimum film preparation narrows considerably and shifts to lower temperatures. A similar tendency was found in our group already for planar magnetron sputtering of YBaCuO-films. [18]. The T_c decrease at temperatures above the optimum substrate temperature and the shift of this decrease to lower temperatures with decreasing oxygen partial pressure can be simply explained by the influence of oxygen partial pressure and temperature on the existence of the perovskite like structure [4].

In Fig. 2.11 we show the dependence of the superconducting transition on T_s for films of the 1-2-3 material on yttrium stabilized zirconia, $Zr(Y)O_2$, of random orientation. The data are similar to those of Fig. 2.10 up to about 810°C . Then at higher substrate temperatures the films strongly degrade and show insulating behavior. From Rutherford backscattering spectroscopy (RBS) and X-ray measurements we found that this degradation is caused by a reaction of the film with the substrate resulting in a mixed oxide of Y, Ba, Cu and Zr. This type of

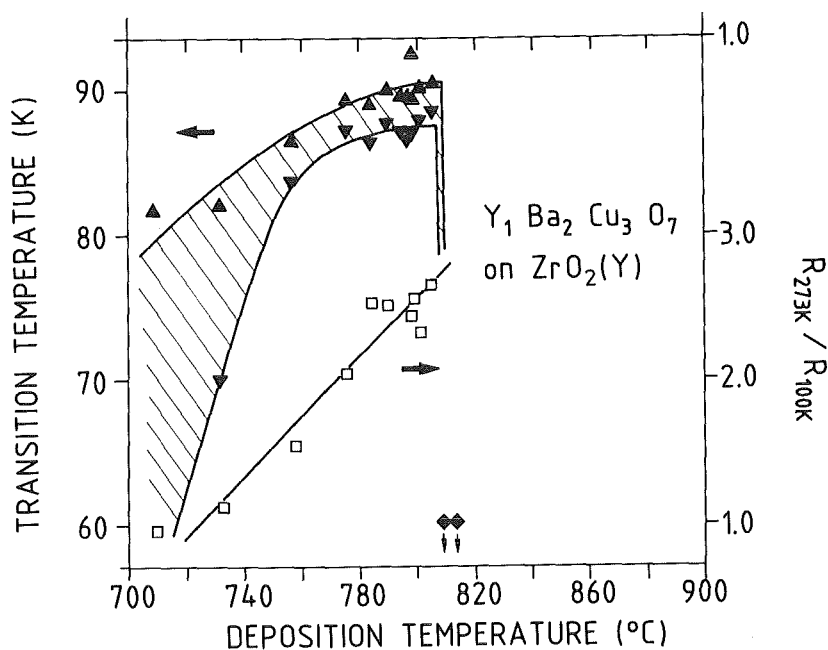


Fig. 2.11 T_c onsets and zero resistance points and the residual resistivity ratios of YBaCuO films vs. deposition temperature for (100) SrTiO₃ (upper part) and Zr(Y)O₂ (lower part) substrates.

reaction which takes place at temperatures above 800°C has been reported already by Cima et al [19]. Therefore we consider the data of Fig. 2.11 as a strong confirmation of the validity of our measured substrate temperatures.

Concluding this section we note, that sputtering from an oxide composite target allows the 2-step preparation of thin films of the 1-2-3 type high temperature superconductors if the negative ion bombardment problem is properly excluded. The measures taken are a sputtering gas pressure exceeding 10^{-1} Torr and an optimum sputtering geometry which is the inverted cylindrical magnetron (ICM). Under these conditions the ICM is a tool of high reliability. In this respect the small scattering of the data of Fig. 2.10 and 2.11 is self explaining. It should be remarked, that in general the reliability of thin film HTSC preparation seems to be a key problem which is presumably the reason why plots of this kind are very rare in literature.

In the following chapters the analysis concerning structure, composition and superconducting properties of films prepared by 2-step ICM sputtering is described in detail. At the end we will demonstrate that this preparation method also allows a first demonstration of possible applications, e.g. the preparation of superconducting tunnel junctions showing a gaplike structure in the I-V characteristic.

3. X-RAY DIFFRACTION ANALYSIS

X-ray diffraction is a standard method for the determination of the microscopic and morphological (e.g. grain shape or grain orientation) structure of materials including thin films. In many cases, however, depending on the problems under investigation specialized equipment must be employed to yield complete and satisfactory results. Thin film analysis generally suffers from low scattering intensities since the amount of material contributing to diffraction is small. Here, line focus diffraction geometries and small angles of incidence are preferable since in this way a larger area of a film will be exposed to the incident X-ray beam. Complete studies of the epitaxial growth of films require equipment depending on the degree of preferred orientation ranging from goniometers suitable for the detection of pole figures for textured growth (like, e.g. four axes diffractometers equipped with tailored software) to high resolution double or even four monochromator systems for the determination of minute lattice mismatches in perfect single crystalline epitaxial growth. Since the 1-2-3 structure compounds on substrates like Al_2O_3 , MgO , SrTiO_3 or Zr(Y)O_2 usually grow with a high degree of texture with the *c*-axis perpendicular to the substrate surface and because the constituents like in YBaCuO are of high atomic number, the diffraction intensity in most cases is sufficiently high such that standard diffractometers may be used.

We have employed a two axes goniometer at a rotating anode X-ray source (40 kV, 200 mA) allowing independent movements of both axes, Θ and ω with an accuracy of 0.001° and a rough adjustment of the azimuthal angle ϕ in steps of 1° . With this diffractometer Θ - 2Θ diffraction spectra were taken in the Bragg-Brentano focusing geometry. In this geometry (for $\psi=0$) only lattice planes parallel to the substrate surface will be detected; this means for single crystalline films that strong lines will only be detected if a major crystallographic direction is aligned with the substrate surface. Similar measurements, however, are possible with a ψ offset, such that planes tangential to the focusing circle but inclined to the substrate surface by an angle of ψ can be detected. Rocking curves (ω -scans) were measured with a stationary detector positioned at an appropriate diffraction angle 2Θ by tilting the sample on the ω -circle through a suitable angular range $\Delta\psi$. Such curves deliver the distribution of particles with a definite orientation (mosaicity) and their alignment with respect to the substrate surface normal. The incident beam diameter for scan-measurements was narrowed to about 1 mm^2 yielding a resolution somewhat below 0.1° . Since the ion beam in channeling experiments has a similar size the mosaic spread obtained with the different methods could be compared from similar areas on a film (see chapter 4).

In addition, measurements have been performed with a thin film diffractometer based on the Seemann-Bohlin focusing geometry at a 1.5 kW X-ray generator. In this geometry the X-ray beam impinges on the stationary sample under a small angle of incidence γ ($0^\circ < \gamma < 10^\circ$). Due to the grazing incidence the area of a thin film hit by the X-ray beam is enlarged by a factor $1/\sin\gamma$ as compared to perpendicular incidence, and as the sample is fixed, always the same volume of material contributes to diffraction independent of the diffraction angle. This allows a direct comparison of line intensities which is important for texture analysis. The stationary sample has another consequence, namely that scattering occurs from lattice planes of different orientation with respect to the substrate surface in contrast to the Bragg-Brentano focusing geometry. For low diffraction angles these are planes slightly inclined to the substrate surface while for higher diffraction angles the inclination increases. A diffraction diagram in the Seemann-Bohlin focusing geometry consequently will be only observed if a sample contains grains of different orientation, i.e. is polycrystalline, and in general no lines will be detected from a truly single crystalline film. Therefore, a comparison of measurements in the different focusing geometries allows discrimination between highly textured growth, single crystalline films containing polycrystalline admixtures and fully single crystalline films.

The growth of the YBaCuO thin films has been studied as a function of various deposition parameters mainly with the aim of improving the transport properties, especially the superconducting transition temperature, T_c , and the critical current density, J_c . Besides the substrate material the deposition temperature, T_s , turned out as a decisive parameter determining the growth and the properties of the films. It was of special interest to correlate the transport properties with the structural growth quality (see chapter 5).

We therefore have studied in some detail the structure of the films on different substrates as a function of the substrate temperature during deposition keeping the other deposition parameters constant. Though a number of common features were observed in the growth on different substrates, the simplest way of data organization is to describe first the results on the single substrates separately and then discuss similarities and dissimilarities in a comparative chapter.

3.1 Films on strontiumtitanate, SrTiO₃

We have used single crystalline SrTiO₃ substrates of (100) and (110) orientation and deposited films in the temperature range $600^\circ \leq T_s \leq 850^\circ\text{C}$ and

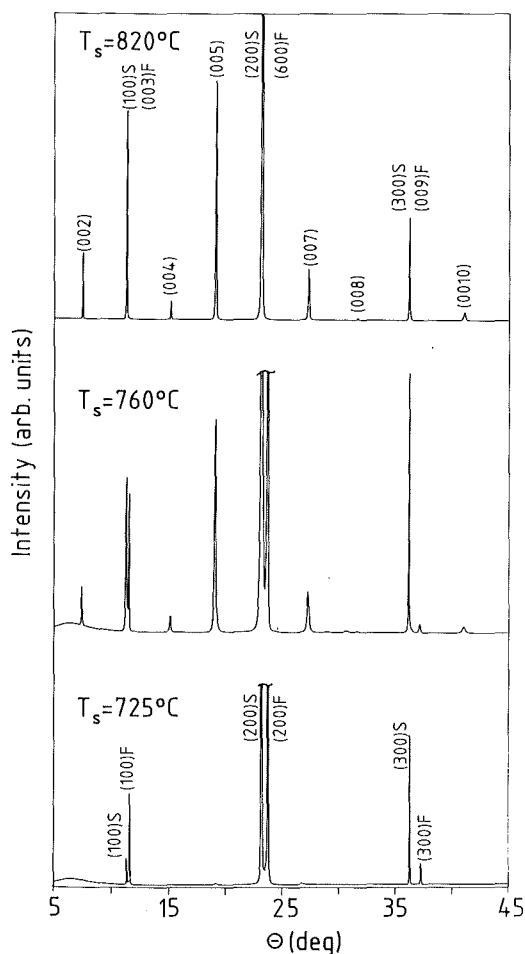


Fig. 3.1
 Selection of X-ray spectra in the Bragg-Brentano focusing geometry of YBaCuO films deposited on (100) SrTiO₃ substrates at different temperatures, T_s , showing "pure" c-axis ($T_s = 820^\circ\text{C}$) and a-axis ($T_s = 725^\circ\text{C}$) orientations and a mixture of both directions ($T_s = 760^\circ\text{C}$).

$700^\circ \leq T_s \leq 800^\circ\text{C}$ for the two orientations, respectively. The thicknesses of the films used in the X-ray measurements typically were about 300 nm. On (100)-oriented substrates the films in the whole temperature range grow highly textured with a general trend that at higher temperatures the c-axis was aligned perpendicular to the substrate surface while at lower temperatures the c-axis was in the film plane and the a-axis perpendicular to the substrate. Between the two extreme cases mixtures of both orientations were observed [20].

As an illustrative demonstration of this growth behaviour we show in Fig. 3.1 three sample spectra representing the different growth regimes. Substrate temperatures around 800°C were best suited to achieve c-axis oriented epitaxial growth. Perfect growth is indicated by the spectrum of a film deposited at T_s of 820°C revealing only lines of the (00ℓ) type. It should be noted, however, that the substrate $(h00)$ lines overlap with the lines of the film for $\ell = 3$ h as indicated in the figure. The main feature of the spectrum of a film deposited at 725°C are well

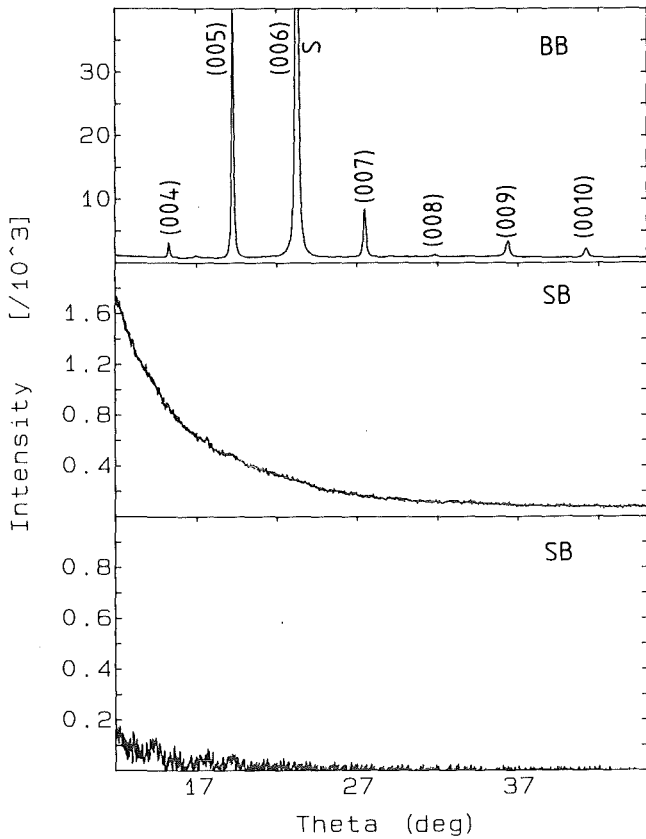


Fig. 3.2
X-ray spectra of an YBaCuO film on (100) SrTiO₃ measured in different diffraction geometries (BB: Bragg-Brentano, SB: Seemann-Bohlin). The lower spectrum was obtained after background subtraction arising mainly by scattering from air. The structureless spectrum in the SB geometry indicates single crystalline growth of the film.

resolved (h00) lines from the SrTiO₃ substrate and from the film demonstrating a highly preferred a-axis orientation. In addition, some faint lines of other orientations and such which could not be assigned to the 1-2-3 phase have been observed in the spectrum. This may explain the enhanced dechanneling yield ($X_{\min} = 25\%$) observed for such films [21] in comparison to c-axis oriented films. Further improvement of a-axis oriented growth appears possible since as yet most efforts have concentrated on the optimization of the deposition parameters of c-axis oriented films due to their superior transport properties. We should mention that, in principle, b-axis oriented growth cannot be excluded from the lower spectrum of Fig. 3.1 because (0k0) lines of the film would overlap with (h00) lines of the substrate. Such growth, however, appears improbable since $b \approx \frac{1}{3} c$. The middle spectrum in Fig. 3.1 of a film deposited at $T_s = 760^\circ\text{C}$ consists of (h00) and (00 ℓ) lines, i.e. the sum of the lines observed for the "pure" c-axis and a-axis oriented cases. This means that c-axis growth changes gradually to a-axis growth by accomodating mixtures of both directions with decreasing deposition temperature.

In Fig. 3.2 we show X-ray spectra of a c-axis oriented film in different diffraction geometries. In the Bragg-Brentano (BB) focusing geometry again merely (00 ℓ) lines are observed. We will demonstrate in further examples that such an appearance alone does not proof single crystallinity. Therefore, in addition spectra are shown in the Seemann-Bohlin (SB) focusing geometry before and after background subtraction. The high background at low diffraction angles arises mainly due to scattering by air. These spectra reveal almost no structure as it is usually observed for single crystals thus strongly indicating epitaxial growth of the film. Such a growth will be later proved by channeling experiments (see chapter 4).

At substrate temperatures above and below those quoted in Fig. 3.1 the oriented growth of the 1-2-3 phase in the film starts to deteriorate. At T_s of 855°C, e.g. c-axis textured growth is still the dominant feature, but in addition to the (00 ℓ) lines many other non identified peaks indicate foreign phase formation probably due to film-substrate reaction. At lower deposition temperature such as 650°C still a-axis oriented growth is observed, but considerable line broadening shows that the growth conditions are worse as compared to those at higher T_s . At 600°C the conditions for epitaxial growth are destroyed, the presence of some lines of the 1-2-3 phase in the X-ray spectra, however, indicates at least polycrystalline phase formation.

The strongly oriented growth of the YBaCuO films in the optimized temperature range allowed an easy determination of the c- and a-axes lattice parameters. The c-axis lattice parameter is constant with a value around 1.168 nm at $780 \leq T_s \leq 855^\circ\text{C}$, i.e. in the temperature range where only c-axis oriented growth was observed. This value is close to that reported for bulk material indicating a stoichiometric oxygen content also in the films in accordance with sharp transitions to superconductivity and low zero resistance values. An abrupt increase of the c-axis lattice parameter is observed at lower deposition temperatures with values of e.g., 1.169 nm and 1.171 nm at T_s of 760°C and 750°C, respectively. This increase coincides with the appearance of a-axis oriented grains in the films. The a-axis lattice constant is around 0.381 nm in the mixture of a and c-axes oriented grains and in the pure optimized [100]-orientation. This value may be compared to 0.382 nm of bulk material [22]. Similar to c, also a increases at low T_s . A value of 0.384 nm at T_s of 650°C indicates deviations from stoichiometry in accordance with the observed disruptions of the superconducting properties. The behaviour of the lattice constants versus T_s will be helpful in the discussion of the appearance of different growth

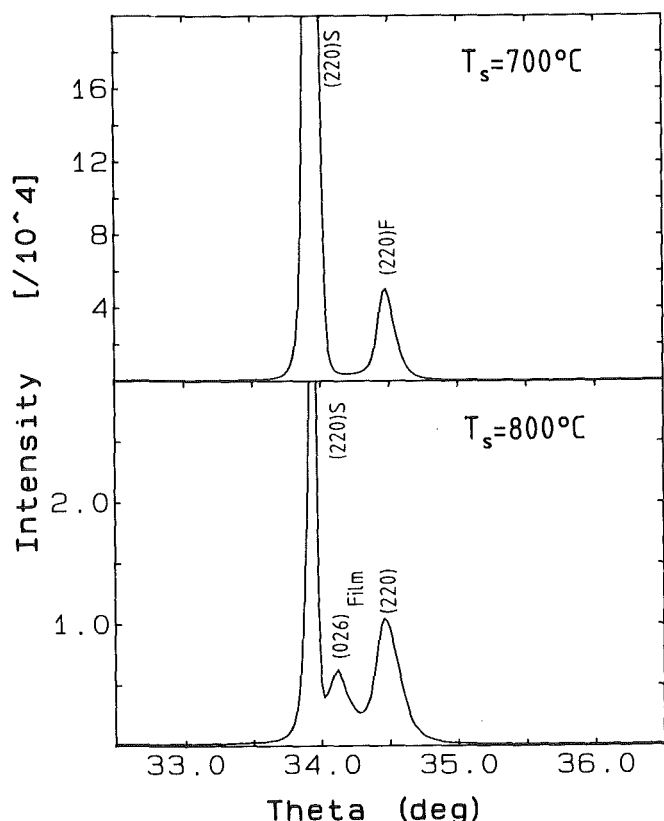


Fig. 3.3
Sections of X-ray spectra of YBaCuO films deposited on (110) SrTiO₃ substrates. Besides the (220) substrate line the diagrams show the (220) line of the film at the lower deposition temperature ($T_s=700^\circ\text{C}$) and in addition a (026) line at $T_s=800^\circ\text{C}$ revealing a pure (110) orientation and a mixed (110)/(013) orientation at different T_s .

directions, though the values were obtained from room temperature measurements after completion of the second preparation step where full oxygen stoichiometry is achieved. We have, however, some indications that the films grow oxygen deficient but already in the orthorhombic phase in the first deposition step, because films quenched to RT after this step revealed broadened transitions to superconductivity [23] (see also chapter 2).

On (110)-SrTiO₃ the growth of YBaCuO films is also temperature dependent, but the dominant characteristic is that the substrate orientation is imposed on the film growth, i.e. the films grow in the (110) orientation. Illustratively, this means that the c-axis is aligned within the film plane parallel to the substrate surface, while a and b form an angle of about 45° with the surface normal. In more detail, we have found a "pure" (110) orientation at the lower deposition temperature of 700°C. At T_s of 800°C in addition to the (hh0) lines also reflections of the (013) type appeared in the X-ray spectra. As an illustration, we show in Fig. 3.3 diffractograms in the 2 θ -angle range of the (220) substrate line. In the spectrum of the film deposited at 700°C besides the substrate peak only the (220) line of the film is seen while at 800°C also a (026) line is observed. We cannot

completely exclude (103) admixtures in our films as reported by Bando et al. [24] due to difficulties in separating (110) from (103) lines since $b \approx \frac{1}{3}c$. Though the lines of the films are broader than those of the substrate their absolute breadth of 0.1° - 0.2° in theta still indicates large grain growth.

Different growth directions besides the c-axis oriented growth of YBaCuO thin films on (100) and (110) SrTiO₃ single crystalline substrates have been quite frequently reported in the past. The substrate temperature was an important parameter in most of such work. A detailed comparison, however, appears difficult because the special deposition parameters reported depend strongly on the deposition method and equipment applied. We therefore just give some reference to related work. a-axis or mixtures of a with c-axis growth e.g., was reported by Kapitulnik [25], Kajikawa et al. [26], Fujita et al. [27] or Edwards et al. [28]. (110) oriented films on (110) SrTiO₃ substrates have been investigated, e.g. by Tonouchi et al. [29] and Bando et al. [24].

3.2 Films on (100)-magnesiumoxide, MgO

The temperature dependence of the growth of YBaCuO films deposited on polished (100) oriented MgO substrates so far has been studied less intensively as compared to the (100) SrTiO₃ substrates. Nevertheless, from the available data we are able to conclude that the growth behaviour qualitatively resembles that of SrTiO₃, however, differs in quantity. This means that principally similar effects are observed, but the temperature scale is shifted. We discuss the results with reference to Fig. 3.4 where X-ray spectra are shown of films deposited at different T_s covering the investigated temperature range of 600°C-800°C. The spectra of the films deposited at T_s of 780°C and 700°C reveal clear (00 ℓ) lines showing c-axis textured growth. Only small admixtures of a-axis oriented grains reflected by faint (h00) lines are present in the 780°C film. This film, however, revealed good channeling performance with a χ_{\min} value of 7% for 2 MeV He⁺ ions such that its principal structure is single crystalline. a-axis textured growth on MgO appeared at lower T_s as compared to the growth on SrTiO₃. It is the dominant feature in the film deposited at T_s of 650°C as demonstrated by strong (h00) lines in Figure 3.4. The a-axis texture, however, is not pure, since in addition to the (h00) lines some c-axis oriented grains and such of (013) and (103)/(110) orientations are present in this film. With decreasing substrate temperature (600°C) the (013) and (103)/(110) orientations grow at the expense of c-axis and a-axis directions, but a-axis orientation is still dominant. Some faint lines of other orientations not resolved in the spectra of Fig. 3.4 in films deposited at lower

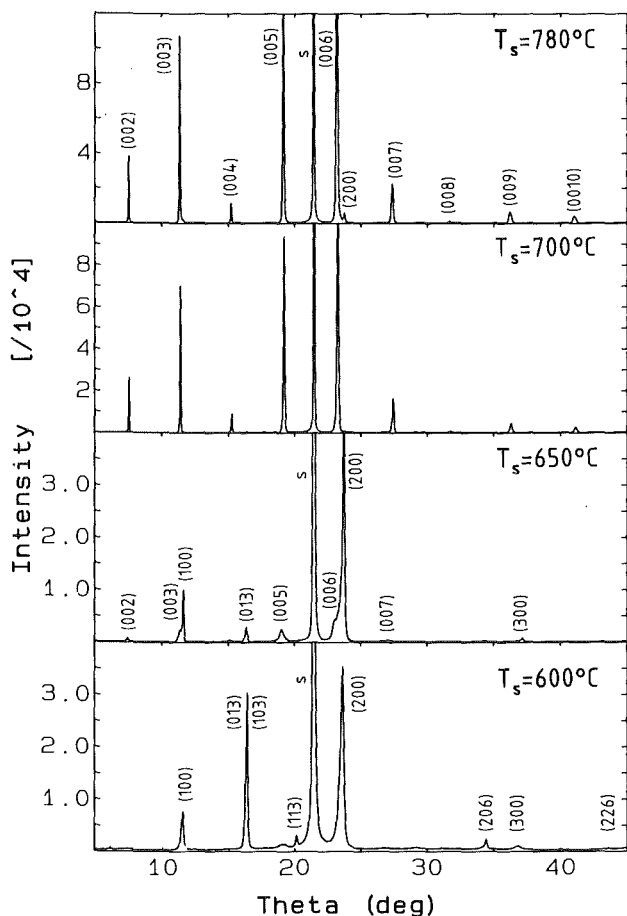


Fig. 3.4
X-ray diffraction diagrams of YBaCuO films deposited at different T_s on (100) MgO substrates. c-axis growth predominates at higher deposition temperatures for $T_s \geq 700^\circ\text{C}$, while at lower T_s a-axis growth with admixtures of (013) and (103) / (110) oriented grains is the dominant feature.

deposition temperatures also indicate the deterioration of the growth conditions for epitaxy in this temperature range.

The behaviour of the c-axis lattice constant in the pure c-axis textured phase, i.e. for T_s down to 700°C , cannot be definitively assessed. This is due to the fact that in different films deposited at T_s around 800°C we observed values ranging from 1.168 nm (corresponding to the bulk value) to 1.172 nm with some indication that the higher values occurred in films having a better growth. The sample films displayed in Fig. 3.4 have values of 1.172 nm and 1.170 nm for T_s of 780°C and 700°C , respectively. A definitive enhancement of the c-axis lattice constant, however, is observed at lower T_s where it coincides with the appearance of a-axis growth similar to the observations on SrTiO_3 . But on MgO the effect is much more pronounced with $c \approx 1.183$ nm at $T_s = 650^\circ\text{C}$. As the matching between film and substrate is an important parameter for epitaxial growth this behaviour appears plausible because the lattice constant of MgO (0.421 nm) is considerably larger than that of SrTiO_3 . The a-axis lattice constant of 0.382 nm for the 780°C

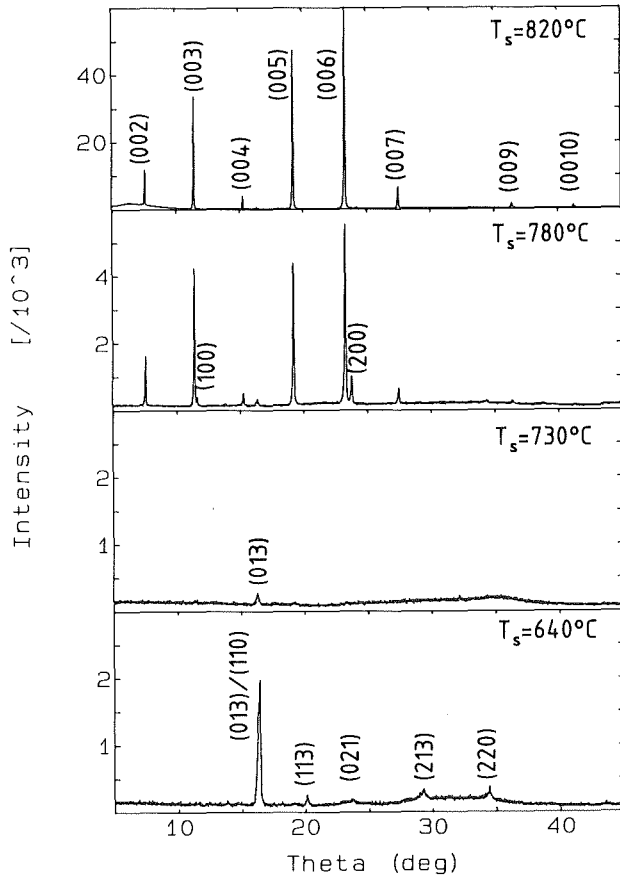


Fig. 3.5 X-ray spectra in the Bragg-Brentano focusing geometry of YBaCuO films deposited on randomly oriented Zr(Y)O₂ substrates at various T_s . While at higher T_s c-axis texture prevails the spectrum at $T_s = 730^\circ\text{C}$ is structureless. This growth behaviour is described in Figs. 3.6 and 3.7.

film corresponds to the bulk value. Enhanced values of 0.383 nm and 0.385 nm were observed at T_s of 650°C and 600°C , respectively.

3.3 Films on yttrium stabilized zirconia, Zr(Y)O₂

Zirconium oxide so far is the only material where we have deposited films on randomly and (100) oriented substrates. The temperature dependence of the growth, however, has been studied on randomly oriented substrates only. Again, we describe our observations by showing sample X-ray spectra in the BB-focusing geometry of films deposited at different substrate temperatures in Fig. 3.5. At the optimized temperature of 820°C with respect to transport properties similar to the observations on (100) SrTiO₃ and MgO c-axis textured growth demonstrated by strong (00 l) lines is the predominant characteristic. Slight indications of other orientations and foreign phase not apparent in the compressed plot of Fig. 3.5 are also present. The amount of foreign phase due to commencing substrate reactions increases at higher T_s (840°C , not shown). Lowering of T_s , like for the example

shown at 780°C leads to a distinct appearance of other orientations, mainly (100) similar to (100) SrTiO₃ and MgO but there at much lower deposition temperatures. The c-axis lattice parameter in this temperature range is around 1.167 nm with a tendency to reduce with increasing T_s.

It is intriguing that at T_s of 730°C almost no structure is visible in the spectrum. This must be due to a highly textured growth, however, with lattice planes not aligned parallel with the substrate surface. We had estimated already from spectra measured in the SB-focussing geometry with an incident X-ray beam inclined by an angle of 10° to the substrate surface that the c-axis of the film must be inclined to this surface by about 10°, because the spectrum revealed rather strong (005) and (006) lines [30]. The misalignment has been proved by an ω-scan with the detector set at the angle 2θ for the detection of the (005) line. The scan is displayed in Fig. 3.6 showing the offset of the c-axis oriented particle distribution by 10.2° and a FWHM of the distribution of 1.5°. Since this substrate was cut such that the surface was inclined by about 10° to the [100] direction in ZrO₂ this growth behaviour again underlines the importance of substrate-film

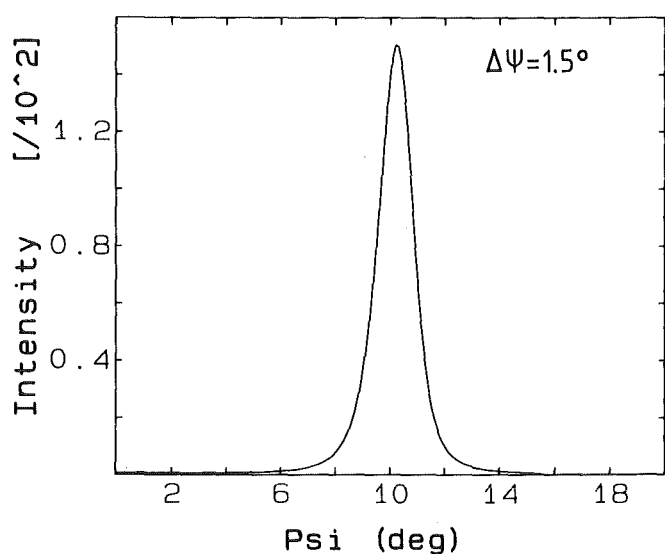


Fig. 3.6
ω-scan of an YBaCuO film deposited at 730°C on randomly oriented Zr(Y)O₂ showing that the maximum of the distribution of c-axis oriented grains is inclined by about 10° to the substrate surface normal.

matching in the epitaxial growth of YBaCuO films. We show the Θ-2Θ spectrum of the 730°C film taken with an ψ offset angle of 10.2° in Fig. 3.7. It reveals, as expected, clear (00ℓ) lines starting at (004) because of shadowing of the lower indexed lines by the ψ offset. The c-axis lattice parameter is 1.169 nm proving the increasing tendency with decreasing T_s. Finally, the film deposited at 640°C

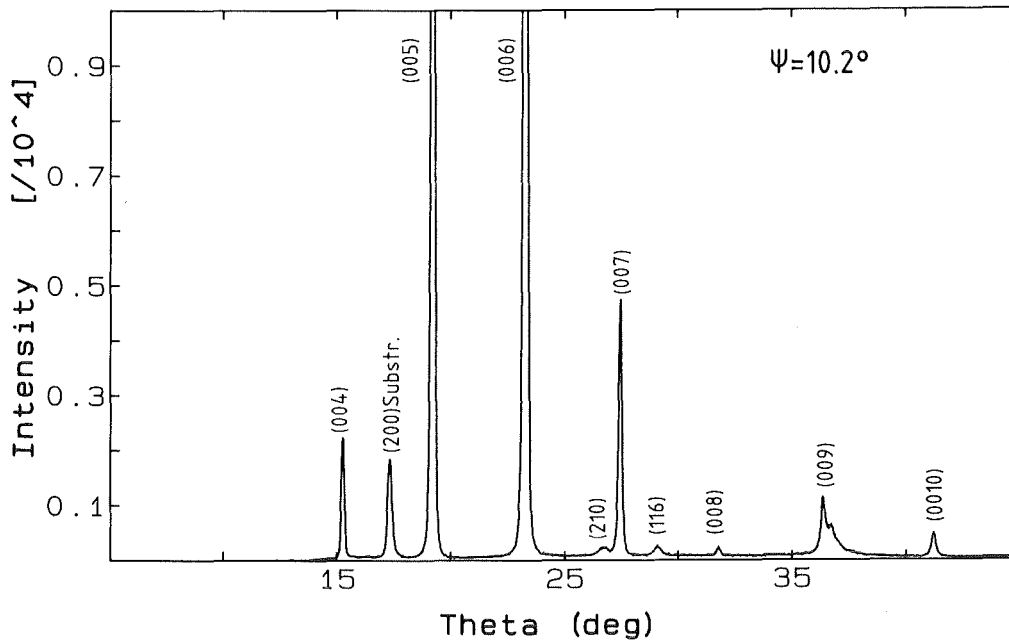


Fig. 3.7 X-ray diagram of an YBaCuO film deposited at 730°C on randomly oriented Zr(Y)O₂ measured with an offset angle of $\psi = 10.2^\circ$. The appearance of the (00 l) lines from the film and the (h00) substrate lines shows that the c-axis oriented grains are aligned with the (100) planes of the substrate inclined to the substrate surface by about 10°.

is polycrystalline showing texture with some preference of the (013) and (103)/(110) orientations.

On (100) oriented Zr(Y)O₂ substrates YBaCuO films have been deposited at T_s of 780°C. They grow in the pure c-axis texture, but again with faint unidentified lines indicating foreign phase formation. The substrates were heat-treated in oxygen atmosphere before deposition. The lattice parameters may depend on this treatment, since values of 1.168 nm and 1.167 nm were determined in films deposited on substrates treated at 950°C and 800°C, respectively. The azimuthal adjustment of the films with respect to the substrate orientation has been determined by channeling measurements and will be dealt with in section 4.6.

3.4 Films on sapphire, Al₂O₃

Sapphire is one of the most commonly used substrates in thin film preparation, but it appears less suited for the deposition of high quality YBaCuO films. One reason is that heavy substrate reactions occur already at rather low deposition temperatures. This can be deduced from Fig. 3.8 where X-ray spectra are shown of films deposited at different T_s . The spectrum of the 820°C film is

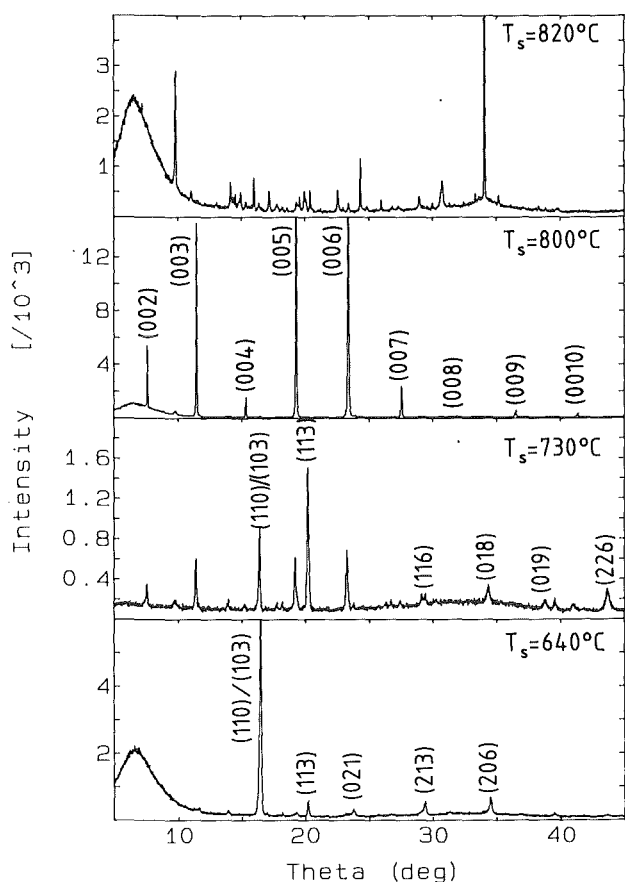


Fig. 3.8
X-ray diffraction spectra in the Bragg-Brentano geometry of YBaCuO films deposited on Al₂O₃ substrates at various T_s. c-axis textured growth is observed at T_s=800°C while the growth at T_s=640°C is very similar to that observed at the same temperature on random Zr(Y)O₂.

clearly dominated by foreign phase formation. At 800°C c-axis orientation predominates, but this only proves textured growth but not epitaxial single crystallinity. The reason is illustrated in Fig. 3.9 where spectra of the 800°C film are compared in the different diffraction geometries. The presence of lines of different type in the SB-geometry reveals that grains of various orientations having lattice planes which are not parallel to the substrate surface exist in the film, i.e., the film though textured, principally is polycrystalline. Such films obstruct channeling and reveal degraded transport properties as will be shown later (see chapter 5).

The polycrystalline nature of the films becomes more pronounced also in the spectra of the BB-focusing geometry at lower deposition temperatures. The c-axis lattice parameter again increases with decreasing T_s. The absolute values at optimized T_s (780-800°C), however, are in the range of 1.165-1.166 nm, i.e. lower than in the bulk material. It is not yet clear whether this is due to oxygen contents above 7. The spectrum of the film deposited at 640°C has almost exactly the same appearance as that deposited at the same temperature on Zr(Y)O₂. This

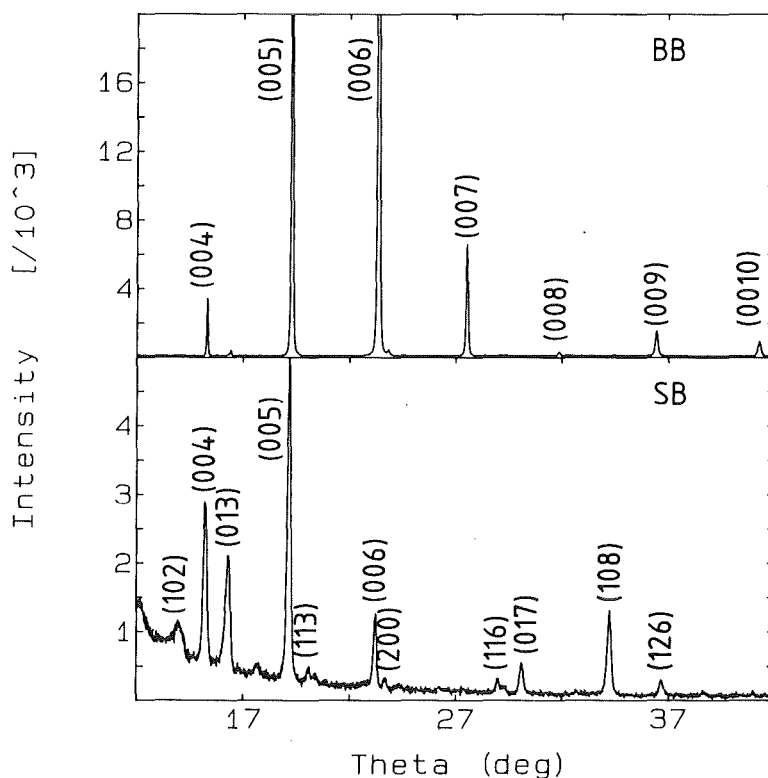


Fig. 3.9 X-ray spectra of an YBaCuO thin film deposited on sapphire in the Bragg-Brentano (BB) and Seemann-Bohlin (SB) focusing geometries. Though the upper spectrum indicates highly c-axis oriented textured growth, the lower one reveals the truly polycrystalline nature of the film.

behaviour suggests that on randomly oriented Al_2O_3 and $\text{Zr}(\text{Y})\text{O}_2$ nucleation at the low temperature is the decisive parameter for textured growth. It should be noted that the enhanced background at low diffraction angles in some of the spectra of Figs. 3.7 and 3.9 is due to scattering from a plastic sample holder hit by the incident X-ray beam.

3.5 Comparison of film growth on different substrates

The results presented have shown that the growth of YBaCuO thin films is strongly influenced by the deposition temperature, the substrate material and the substrate orientation. The matching between the lattice spacings of substrate and film appeared as one of the important intrinsic factors governing the growth direction, but some competing mechanisms determined by the various deposition

parameters may exist and the special conditions in each case finally will decide about the growth characteristics. One general observation was that at deposition temperatures optimized with respect to good transport properties achievement, i.e. temperatures around 800°C, the films grow textured with the c-axis perpendicular to the substrate surface on almost all substrates. This appearance suggests that growth dynamics favour a layer by layer growth of the 1-2-3 layered structure resulting in c-axis texture. An exception was observed on (110) SrTiO₃ substrates where despite a T_s of 800°C, the (110) substrate orientation was imposed on the film structure.

We have demonstrated by measurements in different diffraction geometries that, though c-axis texture prevails on most substrates, the growth quality varies from single crystalline on (100) oriented SrTiO₃ and MgO to principally polycrystalline on randomly oriented Zr(Y)O₂ and Al₂O₃. More quantitatively the growth quality is characterized by ω -scans reflecting the mosaic distribution of grains. Such scans have been measured for c-axis oriented grains in films on various substrates. An example for typical films is displayed in Fig. 3.10 showing narrow distributions for the (100) oriented SrTiO₃, MgO and Zr(Y)O₂ substrates, while broad distributions of several degrees are observed for randomly oriented Zr(Y)O₂ and Al₂O₃. This different growth quality is reflected in the transport properties especially in the critical current densities of the films as will be shown in the last chapter.

The comparison of scans from films on (100) Zr(Y)O₂ and randomly oriented Zr(Y)O₂ directly shows the influence of lattice matching on the epitaxial growth. We have deposited our best films so far on (100) SrTiO₃ and (100) MgO having FWHM values of the mosaic distributions around 0.2°. The variation of the breadths of such distributions on the same substrate material probably is due to differences in the substrate surface finish. The influence of this effect on the growth properties has not been investigated systematically by X-ray diffraction but will be dealt with in detail in the discussion of channeling results in the next chapter.

At lower deposition temperatures we have observed a-axis orientation on (100) SrTiO₃ and MgO. We believe that this growth is governed by the improved lattice matching at lower T_s, since a lattice parameter increase occurred with decreasing T_s. One third of the c-axis lattice parameter at T_s = 750°C on SrTiO₃ (0.3903 nm) is very close to the lattice constant of SrTiO₃ (0.3905 nm). It thus appears plausible that at a slightly lower T_s it is energetically more favorable to accommodate the b and c axes in the film plane with the a-axis perpendicular to the

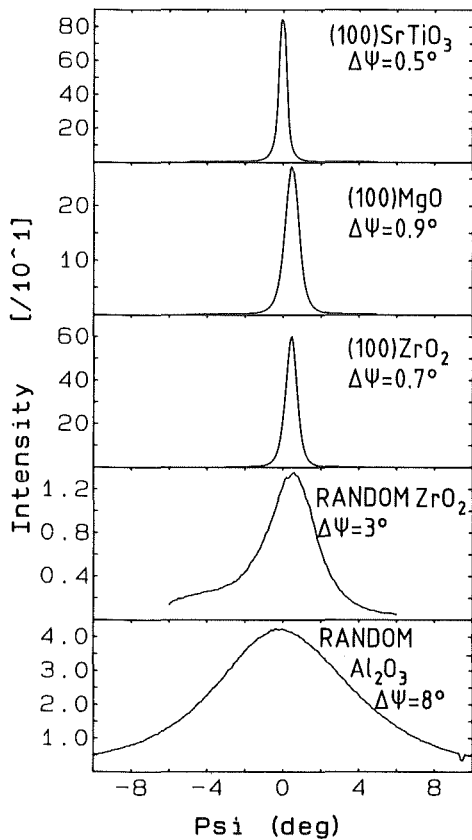


Fig. 3.10
 ω -scans of typical YBaCuO thin films deposited on different substrates with the detector set for the detection of the (005) line. The half-widths of the distributions are a measure of the growth quality of the films.

substrate surface. A better matching of b and c as compared to a and b in the film plane of course would be achieved already at $T_s = 800^\circ\text{C}$, but in this case growth dynamics appear to overcompensate the influence of matching on the growth.

The shift of the a-axis growth to lower T_s on MgO as compared to SrTiO₃ due to the larger lattice parameter of MgO and thus a larger lattice mismatch is a further argument for competing effects influencing the growth behaviour. A detailed quantitative discussion of the special growth conditions must include further parameters like the temperature dependence of lattice spacings of film and substrate or the effects of oxygen incorporation in the different deposition steps on the structure including twinning. This appears difficult at the present state of knowledge. On randomly oriented substrates nucleation and growth of different orientations is favoured by decreasing T_s leading to the formation of polycrystalline structures.

3.6 Ultra-thin films

The X-ray investigations of ultra-thin films with thicknesses below 10 nm[31] so far are in a preliminary state. We show in Fig. 3.11 two representative spectra of 6 nm and 8 nm thick films on (100) SrTiO₃ and (100) MgO, respectively. Besides strong substrate lines the spectra reveal broadened but clear (00 ℓ) lines of the films demonstrating c-axis textured growth also in the initial state of deposition. The film thicknesses estimated from the line broadening were well in agreement with those determined by backscattering measurements. In Fig. 3.12

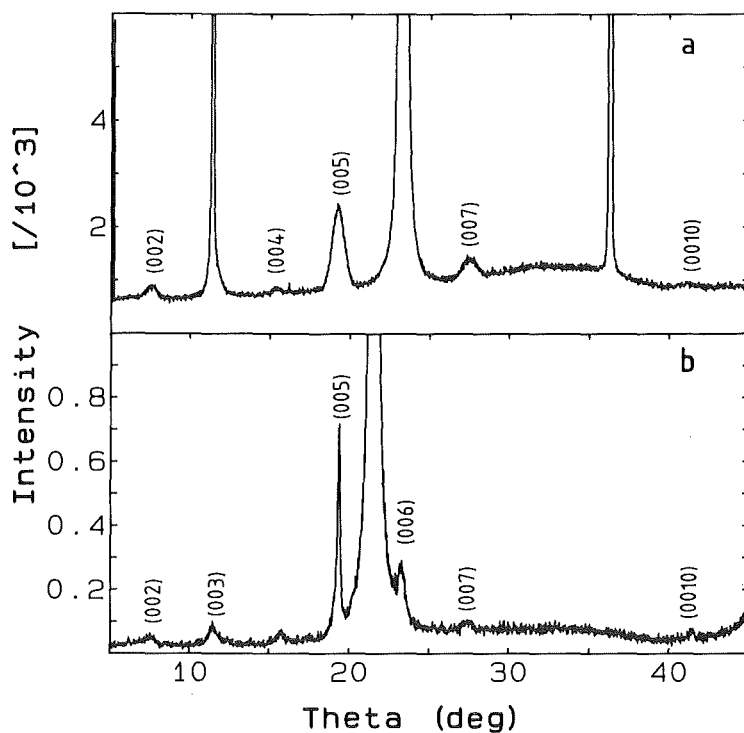


Fig. 3.11 X-ray diffraction diagrams of ultra-thin YBaCuO films with thickness of a) 6 nm on (100) SrTiO₃ and b) 8 nm on (100) MgO, both revealing c-axis textured growth in the initial state of deposition.

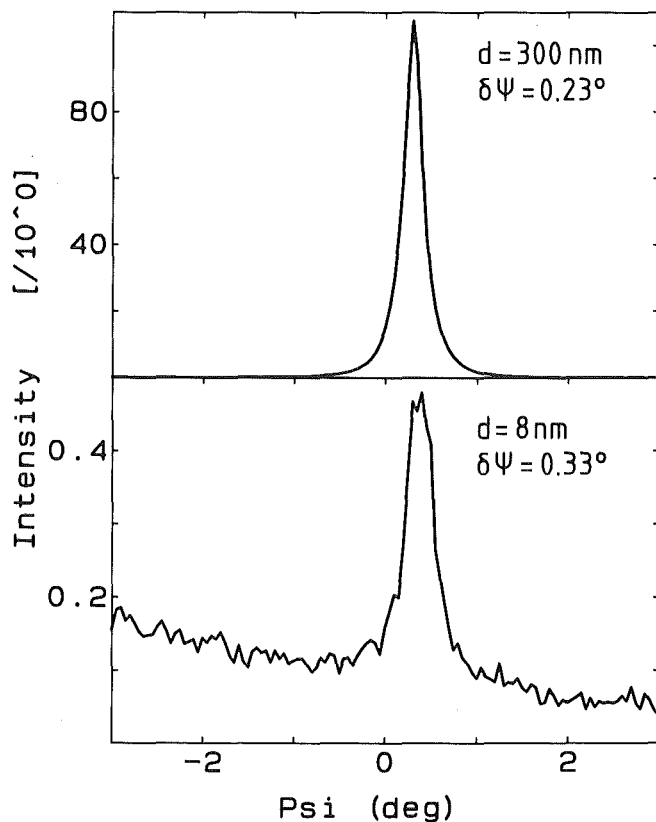


Fig. 3.12
Comparison of rocking
curves of YBaCuO films of
different thickness on (100)
MgO substrates

we compare rocking curves of films on MgO deposited under similar conditions but having different thickness. The increase of the mosaic spread in the ultra-thin film is in accordance with the formation of misfit dislocations as detected in channeling experiments [32] which will be discussed in greater detail in the following chapter.

4. EPITAXIAL GROWTH ANALYSIS BY ION CHANNELING

The motion of energetic charged particles in crystalline targets is strongly influenced by directional effects due to densely packed rows and planes of atoms in the crystal lattice. This phenomenon called channeling was studied by numerous authors and excellent reviews have been published which provide detailed and comprehensive treatments of the subject [33,34,35]. Rutherford backscattering spectroscopy used for thin film analyses [36] combined with channeling has found a widespread application in materials science. Major topics are the determination of lattice locations of dopants, the analysis of intrinsic and radiation induced disorder, surface studies as well as the growth performance of epitaxially layered structures. It is not the purpose of this article to provide a complete list of all known applications. Fortunately, there exists already a comprehensive treatment of the subject [37]. Here only a few applications are mentioned which are important for substrate surface evaluation and epitaxial layer growth.

From the scattering yield of the surface peak the number of contributing surface layers can be readily deduced. Thus the substrate surface and its treatment by various cleaning processes can be controlled and optimized in order to produce nearly defect free surfaces. During heteroepitaxial growth of complex compounds on these surfaces the composition of the compounds can be monitored and variations of the composition due to diffusion or reactions at the interface can be analyzed nondestructively. Further the crystalline quality of the deposited film can be determined as a function of depth. For the case of commensurate growth of systems having slightly different lattice parameters the deposited film will be strained and the amount of this strain can be detected with ion channeling. The application of ion backscattering and channeling spectroscopy to strained layer analysis has been treated in a recent review [38]. The strain associated with the lattice mismatch may be relieved by forming misfit dislocations at the interface. The defect density at the interface, within the film and the surface can be evaluated. From the energy dependence of the dechanneling yield the nature of the disorder may be determined [37,39]. The analysis of angular yield curves provides information on the distribution of film crystallites about the growth direction (mosaic spread) [37]. In the following these analyses concepts are used to analyze and optimize the growth of single crystalline YBaCuO thin films on various single crystalline substrates.

4.1 Analysis concepts

In a typical backscattering experiment a well collimated beam of monoenergetic particles with a beam diameter of about 1 mm is directed onto a single crystalline target mounted on a goniometer. The backscattered particles are detected with an energy sensitive nuclear particle detector. If the crystal directions of the target are well aligned with the incident beam direction the backscattered spectra will be quite different from those of a non-aligned target. Some ions will undergo head-on or close-encounter collisions with the surface atoms and will provide a surface peak in the aligned spectrum. This surface peak provides information on the quality of the crystalline structure near the surface. Ions which enter the crystal close to the atomic rows will experience a high potential energy and will be deflected by angles following the laws of central force scattering. With increasing impact parameters (decreasing scattering angle) these particles are steered away from the rows, cross the center of the channel and may be deflected back by other rows bordering the channel. These particles give rise to flux oscillations which damp out due to multiple scattering. The majority of the incident particles have large impact parameters and thus scatter at small angles in forward directions. The well channelled particles experience many glancing collisions with atoms in successive lattice positions leading to a strong reduction of the backscattered yield in the order of 98%. A simple description of the channeling effect can be derived by the concept that the potential in binary collisions between the ion and the target atoms is replaced by a continuum potential between the ion and a string of atoms [40].

For a compound where a string of atoms may be composed of different elements the string potential can be characterized by the mean distance d between neighbored atoms in the row and by the mean atomic number [34]. Using Molière's screening function [41] the continuum potential distribution for 2 MeV He-ions along the c -direction of $\text{YBa}_2\text{Cu}_3\text{O}_7$ has been calculated and is shown in Fig. 4.1. As a variable in the screening function the ratio u_{\perp}/a is used where u_{\perp} is the one-dimensional rms thermal vibrational amplitude and a is the Thomas-Fermi screening parameter [34]. The vibration amplitudes are averaged for contributions of the atoms in the string using values of 0.083 Å for Ba, 0.076 Å for Y, an averaged value of 0.067 Å for Cu(1) and Cu(2) and an averaged value of 0.088 Å for the oxygen atoms on various positions. These values are taken from high resolution neutron diffraction measurements [22].

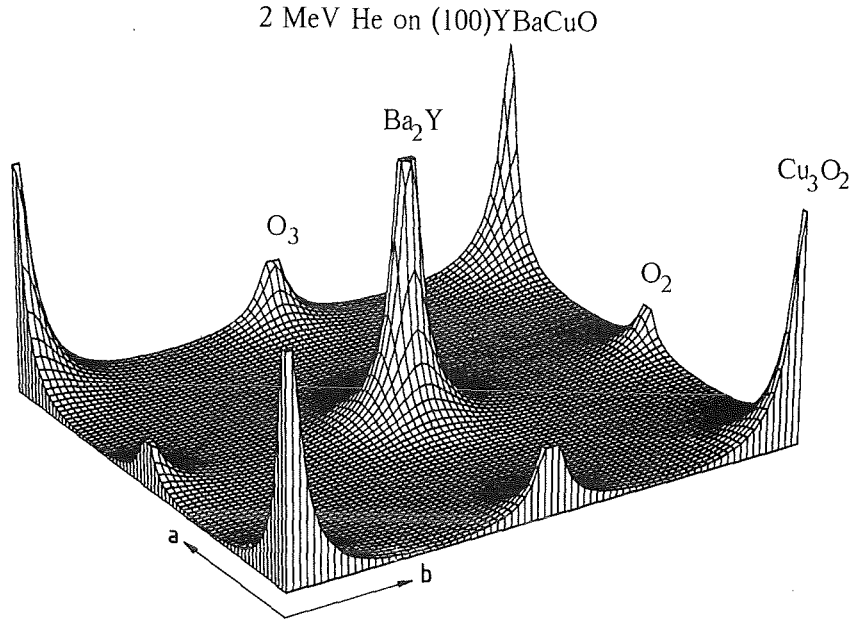


Fig. 4.1 Continuum potential energy distribution for 2 MeV He ions channeled along the c-direction of $\text{YBa}_2\text{Cu}_3\text{O}_7$.

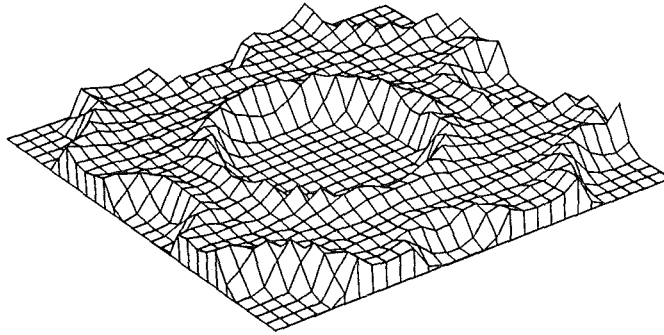
From Fig. 4.1 it is obvious that the Ba_2Y row exhibits the strongest steering force while for the O_2 rows the steering force is weak. The consequences of the potential distribution on the flux distribution will be discussed below. The important feature of Lindhard's continuum theory [40] is the fact that the transverse energy E_{\perp} of the charged particles is conserved during glancing collisions and can be expressed by the sum of the transverse potential energy, $U(r)$, and the transverse kinetic energy, $E \cdot \psi^2(r)$, (E is the energy of the incident particle and ψ , the angle between the particle track and the atomic rows). This leads to a simple relationship between the angle of incidence and the distance of closest approach to the row, r_{\min} (r_{\min} is in the order of u_{\perp}). Thus a critical angle $\psi_{1/2}$ for channeling is obtained for $r_{\min} \sim u_{\perp}$, separating well channeled particles from those with $\psi > \psi_{1/2}$ which will not feel the steering force of densely packed rows or planes. The dependence of the backscattered yield on the angle of incidence can easily be measured. Such angular yield curves are characterized by the minimum yield, X_{\min} , which is the ratio of the yield for perfect alignment to that of random incidence, and $\psi_{1/2}$, which is the half angle at half height $(1 - X_{\min})/2$. The measured $\psi_{1/2}$ and the X_{\min} -values may be compared to calculated values using the formulas from Barrett [42]: $\psi_{1/2} = 0.8 \text{ FRS } (1.2 u_{\perp}/a)\psi_1$ where

ψ_1 is the so-called Lindhard's characteristic angle: $\psi_1 = [2Z_1Z_2e^2/(dE)]^{1/2}$ and $\chi_{\min} = 18.8 N \cdot d \cdot U_{\perp}^2$ (N is the atomic density of the target).

The relationship of χ_{\min} and $\psi_{1/2}$ with u_{\perp} is widely used to determine changes of the lattice vibrations and small static displacements of atoms from their equilibrium lattice sites. The technique is employed to analyze the structure of impurity defect complexes formed in irradiated [43] and implanted systems [44] as well as to determine atomic relaxations in non-stoichiometric refractory compounds [45] and irradiated superconductors with A15 crystal structure [46]. A steplike change of $\psi_{1/2}$ was observed for YBaCuO-single crystals at temperatures below (77 K) and above (100 K) the superconducting transition temperature, T_c [47]. The latter change may be related to an abnormal structural deformation near T_c .

For complex crystalline structures where the steering of particles from different rows leads to a complicated interaction as well as for the analysis of the surface peak where the contribution from successive atoms in the row due to thermal vibrations has to be considered, analytical models are difficult to apply. Therefore the experimental results were analyzed with Monte Carlo computer simulations [42,48]. In these calculations the trajectories of a fixed number of charged particles on their way through the YBa₂Cu₃O₇ lattice are calculated applying a binary-collision model. For the interaction of the ions with the target atoms a Thomas-Fermi potential in the Molière approximation [41] was used. The calculation of the scattering angles was performed using the momentum approximation [49]. The simulation of the thermal vibrations has been performed by choosing the positions of the target atoms according to an isotropic Gaussian distribution with mean values for the vibration amplitudes as given above. The simulation of the angular spread of the channeled particles due to collision with electrons and plasmon excitations was approximated by slight variations of the particle momentum assuming a Gaussian distribution for these changes. The flux distribution along the c -direction of the YBa₂Cu₃O₇ single crystal reveals strong variations. At a depth of 10 nm from the surface the flux profile is not yet fully developed, some flux accumulation is seen around the atomic rows (see Fig. 4.2). At larger depth the flux has accumulated in the potential minima, is well established and has nearly reached equilibrium conditions. While for the simulation of the flux distribution 10^5 particles were used this number was reduced to 3024 for the simulation of angular yield curves. In these calculations the angle of incidence was changed in steps of 0.2 deg. The encounter probabilities between the incident ions and the lattice atoms at depths between 30 and 100 nm

He-Ion Flux at 10 nm in YBaCuO (c-direction)



He-Ion Flux at 100 nm in YBaCuO (c-direction)

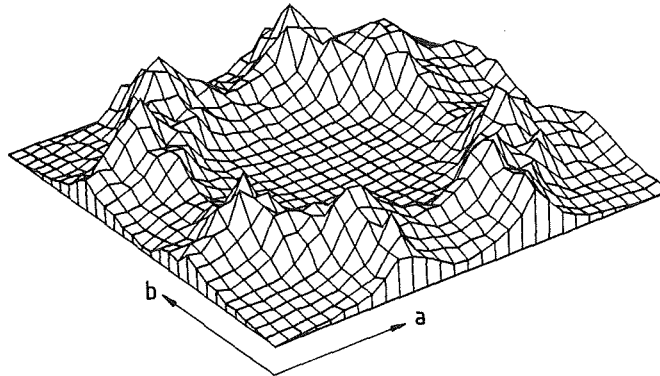


Fig. 4.2 Flux distribution at depths of 10 nm and 100 nm for 2 MeV He ions channeled along the c-axis direction of $\text{YBa}_2\text{Cu}_3\text{O}_7$

were summed up and then normalized to the value calculated for non-oriented incidence. Due to the approximations applied in the calculations of the electron energy loss the simulation will not be able to describe quantitatively the shoulder region of the angular yield curves. However, neither the $\psi_{1/2}$ - nor the χ_{\min} -values are affected by this procedure and should provide more reliable values for $\text{YBa}_2\text{Cu}_3\text{O}_7$ than those obtained from Barrett's formulas.

In Fig. 4.3 calculated angular yield curves through the c-direction are shown for the Ba- and O-sublattices choosing tilt planes 15 and 30 degrees off the (100) plane. It is noted that the critical angles of both sublattices strongly depend on the tilt plane. This fact has to be considered in comparing with experimental results. The large difference of the angular yield curves for O at tilt angles near

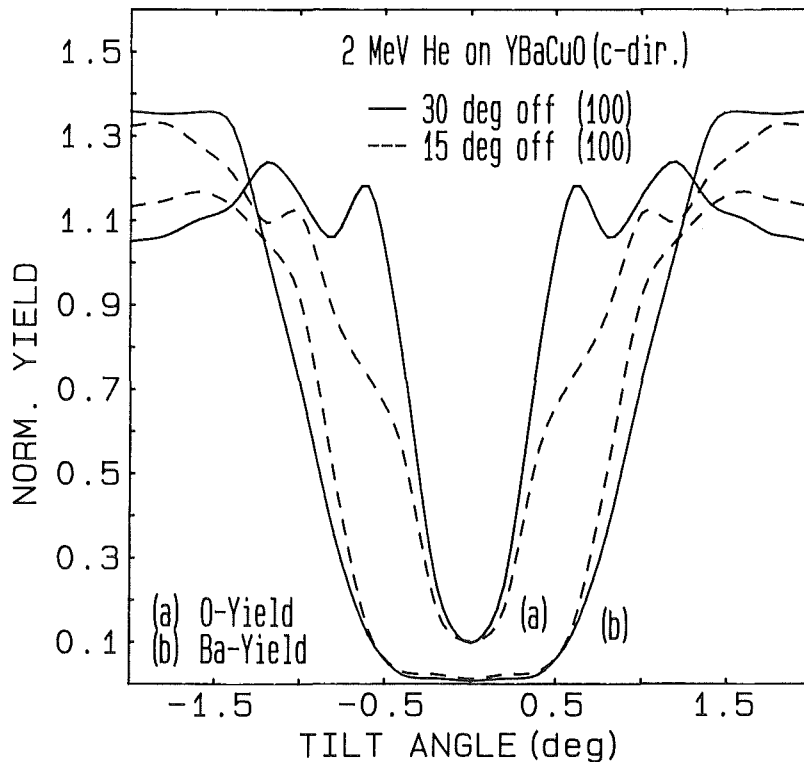


Fig. 4.3 Calculated angular yield curves for 2 MeV He ions scattered from Ba and O. The tilt planes chosen were 15° and 30° off the (100) plane.

0.5 deg is due to the large scattering probability of He-ions close to the (110) plane, which penetrate planes of oxygen atoms with low steering power [50]. The critical angles for the Y-sublattice are slightly larger than those for Ba due to the smaller average vibration amplitude while those for the Cu-sublattice are smaller.

4.1.1 Surface peak analysis

The analysis of the surface peak area is important for the substrates as well as for the films. A perfect substrate surface is the precondition for good epitaxial growth while a perfect film surface is important for applications, for example for the preparation of tunnel junctions and perfect superconductor semiconductor interfaces. From the surface peak area one can immediately calculate the number of surface layers contributing. The measured value usually will be larger than the calculated one due to oxide layers or other modifications such as relaxations and reconstructions. The normalized close-encounter probability of the first layer atom in the row is unity by definition, the contribution of the following atoms will

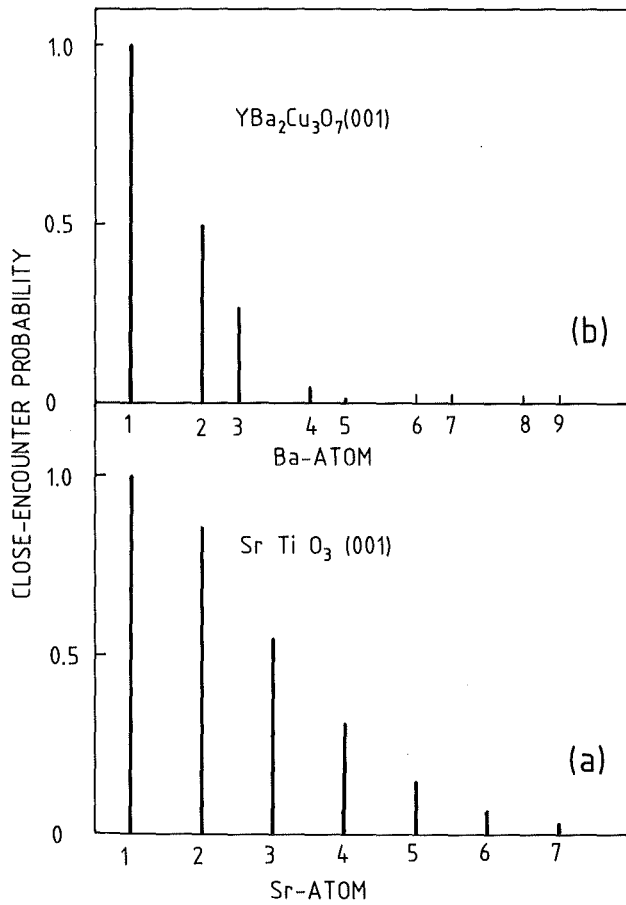


Fig. 4.4
Close-encounter probabilities from successive Ba-atoms in the Ba₂Y row along the c-axis direction of YBa₂Cu₃O₇ (a). Close-encounter probabilities of successive Sr-atoms along the <100> crystal direction of SrTiO₃ (b).

be less than unity because of the shadowing effect of the first atom. The first atom in the row will produce a shadow cone with a cone radius, R_c at the second atom in the row equal to $R_c = 2\sqrt{Z_1 Z_2 e^2 d/E}$ [37]. Due to thermal vibrations there will be a certain probability that the second and the following atoms in the row contribute to the surface peak. These contributions are calculated using the Monte-Carlo simulation described above. For SrTiO₃ the following values for the one-dimensional rms vibration amplitudes have been used [51] at 300 K: 0.081 Å for Sr, 0.062 Å for Ti and an average value of 0.076 Å for O. Using these values rather good agreement between the measured and the calculated $\psi_{1/2}$ - and X_{\min} -values for Sr and O were observed at 3.05 MeV He ion energy [50]. The calculated contributions for each successive Ba-atom in the Ba₂Y-row and for each Sr-atom in the Sr-row along the [100] direction of SrTiO₃ are shown in Fig. 4.4. In order to get the total close-encounter probability contributing to the surface peak the individual contributions from each atom have to be added. The sum of the individual probabilities for 2 MeV He ions incident along the c-direction of

YBa₂Cu₃O₇ and along the [100] direction of SrTiO₃ are 1.8 and 3.0, respectively. Due to the larger shadow cone radius the contribution of the second and successive Ba-atoms is smaller than that of the corresponding Sr-atoms. As will be discussed below the measured surface peak areas will depend on surface cleaning processes and on the parameters which determine the film growth.

4.1.2 Disorder analysis

During the growth of single crystalline films various intrinsic defects will be incorporated such as misfit dislocations at the interface, polycrystalline fractions, foreign phase fractions, dislocations, precipitations, stacking faults, twins etc. The advantage of the channeling technique for disorder analysis is that it provides a fast and simple tool to determine the total defect density, e.g. the crystalline quality and to provide depth profiling which separates defects at the interface, within the layer, and at the surface. Thus the growth process parameters can be optimized in order to reduce the total defect density. Each type of defect has a particular influence on the trajectory of the analyzing particle which is determined by the dechanneling factor σ_D [37]. The probability of dechanneling per unit length dP_D/dz is the product of σ_D and the defect density n_D . The dechanneling factor can be considered as the cross section for a special type of defect which depends in a characteristic way on the analyzing beam energy. Thus from energy dependent measurements information on the special type of defect can be obtained. The disadvantage of the channeling technique is that the method is not very sensitive, the lower limit of detection is about 1 at% of displaced atoms using single alignment. Further, the analysis is ambiguous if different defect structures contribute to σ_D . For defect analysis the incident beam is divided into two fractions, the channeled fraction, $1-\chi_R$, and the random fraction, χ_R . The presence of disorder causes a decrease of the channeled fraction and a corresponding increase of χ_R which depends on the penetration depth, z . The measured aligned yield, $\chi_D(z)$ for a crystal containing defects is given by

$$\chi_D(z) = \chi_R(z) + [1 - \chi_R(z)] \cdot (f \cdot n_D(z)/n)$$

The defect scattering factor f is unity for single displaced atoms and zero if the atoms are only slightly distorted as in strain fields around dislocations. It will be shown that the surface peak which is produced by direct backscattering is small and does not contribute to the dechanneling in the layer. Assuming the presence of mainly extended defects in the layer, f will be near zero.

The random fraction, $\chi_R(z)$ which is the sum of the random fraction for a defect-free crystal and the dechanneled fraction due to extended defects, cannot be measured directly. For small defect concentrations it is given by [37] :

$$\chi_R(z) = \chi_v(z) + [1 - \chi_v(z)] \int_0^z \sigma_D n_D(z') dz'$$

where $\chi_v(z)$ is the minimum yield of a defect-free crystal which is measurable or can be calculated. Neglecting the depth distribution, than in zero order approximation the minimum yield, χ_D , behind the surface peak is equal to the product $\sigma_D * n_D$. The energy dependence of χ_D provides some information on the type of the defects [39]. Polycrystalline fractions and stacking faults are independent on the energy while for dislocation lines (strain regions) χ_D decreases and for interstitial atoms and small amorphous clusters χ_D increases with decreasing analyzing beam energy.

4.2 Substrate surface preparation and analysis

A defect-free substrate surface is a necessary precondition for epitaxial layer growth. Therefore, prior to deposition the substrates were analyzed by ion backscattering and channeling spectroscopy and the influence of various surface cleaning techniques such as polishing, etching, sputtering and annealing in oxygen atmosphere on the surface peak was studied. Highly polished substrates have been received from different manufacturers which very often revealed quite different surface peak areas even for samples from the same charge. In order to get reproducible growth results the substrates were routinely analyzed and were posttreated if necessary. Some SrTiO₃ single crystals were of excellent quality as is demonstrated in Fig. 4.5, where the random and [100] aligned spectra are shown. The low minimum yield value (1.7%) behind the surface peak and the rather small dechanneling factor indicate that the single crystal is nearly free of dislocations. These single crystals were of high quality even for the oxygen sublattice. The oxygen sublattice was studied using the resonant scattering of 3.04 MeV He-ions on ¹⁶O [50]. The $\psi_{1/2}$ - and χ_{\min} -values for Sr and O were in good agreement with those obtained from Monte-Carlo simulation calculations. This is also true for the Sr-sublattice analyzed with 2 MeV He-ions as is demonstrated in Table 1.

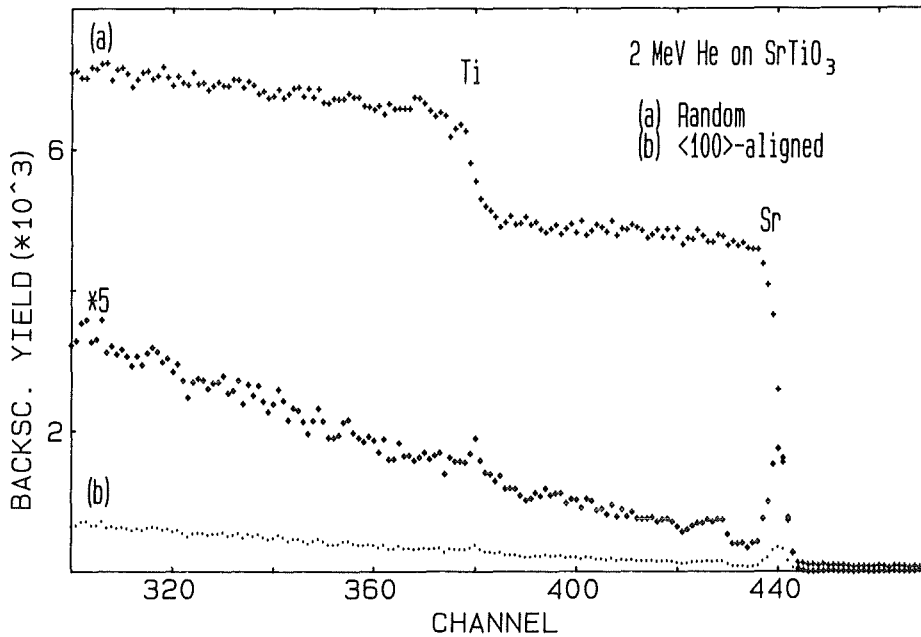


Fig. 4.5 Random and [100]-aligned backscattering spectra from a SrTiO_3 single crystalline substrate.

From the surface peak area (SPA) the number of Sr-atoms/cm², N_t , can be evaluated [36] by $N_t = \text{SPA} \cdot c \cdot \delta E / (H \cdot \epsilon)$ where c is the relative concentration of Sr-atoms, δE the energy / channel, H the height of the Sr-yield in the random spectrum at the surface, and ϵ the backscattering energy loss factor of He ions scattered from the Sr-atoms in SrTiO_3 . The result is that 2.1×10^{15} Sr-atoms/cm² contribute to the surface peak shown in Fig. 4.5. For the (100) surface this number is equal to 3.2 Sr-atoms / row. From Monte-Carlo calculations (see section 4.1.1) a contribution of 3.0 Sr-atoms/row to the SPA is obtained. This result is close to the experimental value indicating that a defect-free (100) SrTiO_3 surface can be obtained by careful polishing. For substrates where the measured SPA was larger than 3.2 Sr-atoms/row, annealing at 950°C for 1 h in 1 atm O₂ usually leads to a decrease of the peak area. The peak structure behind the SP is due to flux oscillation with depth, mentioned in section 4.1. A further test of the surface quality is the determination of the energy dependence of the SPA. Due to the shadow cone the SPA should decrease with decreasing analyzing beam energy. This behaviour is indeed observed as is demonstrated in Fig. 4.6 where it is seen that the experimental results are in good agreement with the calculated data.

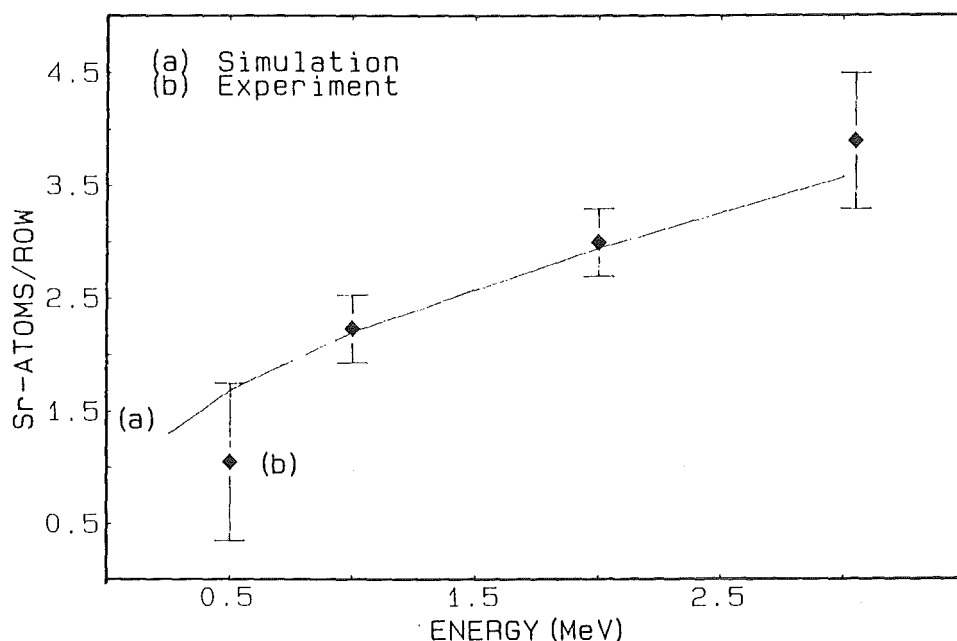


Fig. 4.6 Sr surface peak area in Sr-atoms/row as a function of the analyzing He-beam energy. The solid line is from Monte Carlo simulation calculations.

The properties of (100) MgO surfaces prior to film deposition were also characterized by the channeling spectroscopy. Cleaved as well as polished substrate surfaces have been studied. For both, cleaved and properly polished surfaces χ_{\min} values of 2% and nearly equal values for the SPA's were obtained. This is demonstrated in Fig. 4.7 where the [100]-aligned spectra are shown for a cleaved and a polished MgO surface. Further, the angular yield curves have been measured and the results for the critical angle and for χ_{\min} are given in Table 1. The measured values are in good agreement with those determined by Monte Carlo simulation calculations. In these calculations the mean one-dimensional vibration amplitude for Mg and O used was 0.063 Å. This value was obtained from temperature dependent Debye-Waller factor measurements by X-ray diffraction[52]. The measured SPA is also in good agreement with the calculated one (Table 1) which indicates that cleaved as well as properly polished surfaces are nearly free of defects or structural distortions. It should be noted however that for many MgO-substrates enhanced SPA's are observed. Even for cleaved surfaces sometimes 1 extra Mg-atom/row was detected. Chemical etching of MgO samples leads to an enhanced SP with a composition of about MgO_{2.5} indicating that probably Mg-Peroxide is formed at the surface in the etching process. Annealing at 1300°C in 1 atm O₂ leads usually to a decrease of the SPA.

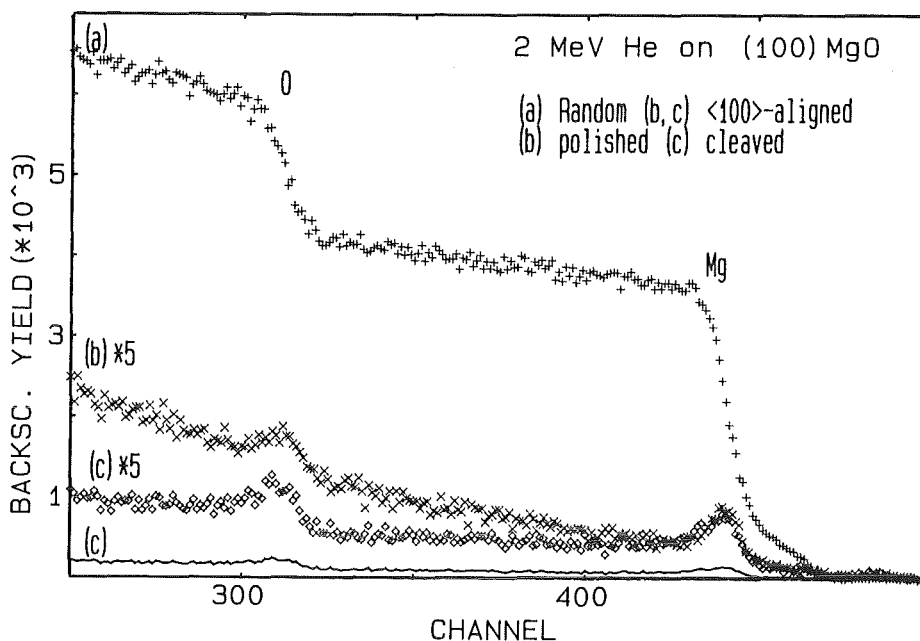


Fig. 4.7 Random and $\langle 100 \rangle$ -aligned backscattering spectra from MgO single crystalline substrates. The enlarged aligned spectra are shown for a cleaved and a polished MgO-substrate.

The situation concerning the Y-stabilized cubic $Zr(Y)O_2$ substrates is not clarified yet. Up to now we did not receive substrates with properly polished surfaces. This is demonstrated in Fig. 4.8 where the random and two $[100]$ aligned backscattering spectra are shown. The aligned spectra are from two different substrates of the same charge. The large difference of the SPA's indicates quite different polishing quality. Both substrates were annealed at $950^\circ C$ in 1 atm O_2 . A large decrease was observed for substrate (c) but not for substrate (b) as is demonstrated by spectrum (d). Annealing at $1300^\circ C$ did not lead to a further reduction of the SPA. Analyzing this SPA leads to 5.1×10^{15} Zr-atoms/cm² which corresponds to 3.4 Zr-atoms/row. Monte-Carlo calculations, however, resulted in a far smaller value of 1.4 Zr-atoms/row, due to a rather small one-dimensional rms vibration amplitude of 0.042 \AA . This value was used in a previous channeling study of $Zr(Y)O_2$ single crystals [53]. From the difference of the measured and calculated SPA it can be concluded that the surface disorder corresponds to 3 Zr atoms/row. This is a factor of 2 larger than observed previously for the (111) surface of $Zr(Y)O_2$ [53]. Large discrepancies are also observed for the angular yield curves of 2 MeV He ions scattered from Zr shown in Fig. 4.9. The measured χ_{\min} - and $\psi_{1/2}$ -values are far smaller than the calculated

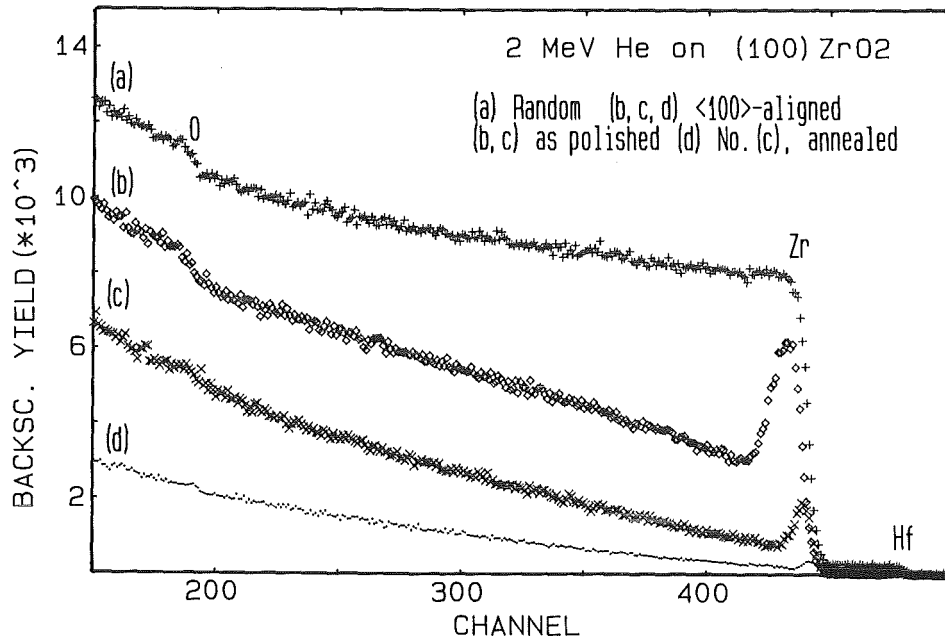


Fig. 4.8 Random and <100>-aligned backscattering spectra from Zr(Y)O₂ single crystalline substrates. The aligned spectra are shown for 2 substrates (b) and (c) with different surface quality and for sample (c) after annealing, (d).

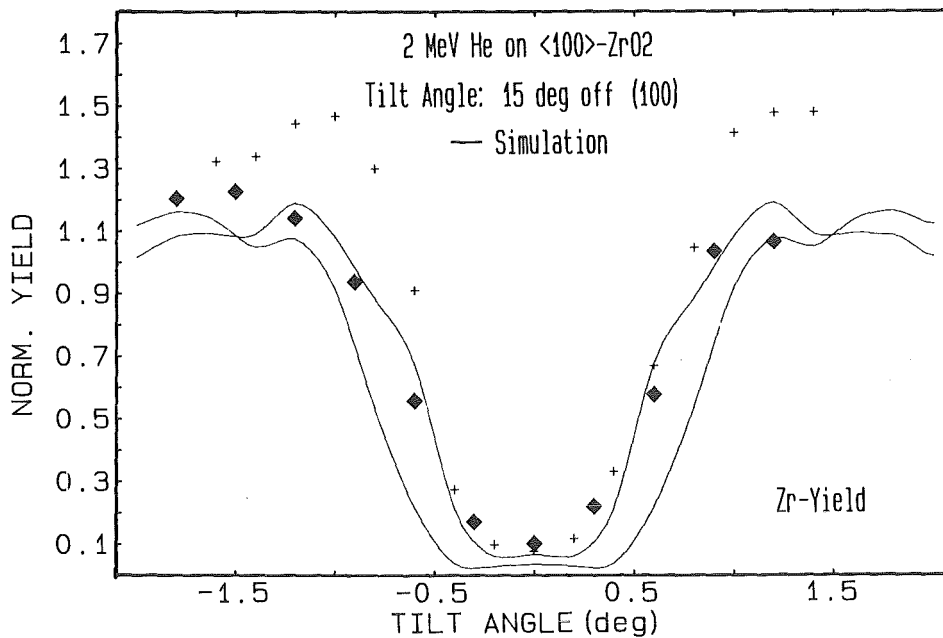


Fig. 4.9 Measured and calculated angular scan curves through the <100> crystal direction of Zr(Y)O₂ in a tilt plane 15 deg. off a (100) plane.

data (see also Table 1). Only if the mean vibration amplitude is deliberately raised from 0.042 Å to 0.1 Å a rather good agreement between measured and calculated data can be obtained (solid curve through the data points in Fig. 4.9). This large amplitude however is in good agreement with the large temperature factors for the cations of $B=1.2 \text{ \AA}^2$ ($\bar{u}_\perp=0.12 \text{ \AA}$), determined by neutron diffraction measurements on Zr(Y)O_2 [54]. These large B-values are attributed to cation relaxations towards O-vacancies which in turn are incorporated to maintain local charge neutrality. Using a value of 0.1 Å for the mean vibrational amplitude the number of Zr atoms/row contributing to the surface peak would rise to 3.0 in reasonable agreement with the measured value. This result leads to the conclusion that the large surface peak may be due to relaxations of Zr atoms near the surface towards O vacancies and a further improvement of the surface peak by cleaning processes could therefore not be obtained.

Substrate	$\psi_{1/2}$ (deg)		Min. Yield (%)		SP (atoms / row)	
	exp	cal	exp	cal	exp	cal
(100) SrTiO ₃	0.74	0.73	1.7	1.4	3.3	3.0
(100) MgO	0.69	0.67	2.2	2.1	3.1	3.35
(100) ZrO ₂	0.55	0.78	7.5	2.1	3.4	1.35

Table 1. Comparison of the experimental and calculated values for $\psi_{1/2}$, χ_{\min} and SP obtained for 2 MeV He ions on (100) SrTiO₃, (100) MgO, and (100) ZrO₂

4.3 YBaCuO thin films: growth performance and disorder

A good quality of the substrate surface is just one necessary precondition for the successful growth of epitaxial layers. Other preconditions are the substrate temperature during deposition and the orientation of the substrate surface. In chapter 2 it was shown that at high substrate temperatures, depending on the substrate material, interface reactions will occur and will prohibit epitaxial growth. At low substrate temperatures the growth orientation will change. The film orientation as a function of substrate temperature and orientation can easily be determined by X-ray diffraction analysis. The growth dependence on these parameters has been discussed in detail in chapter 3. Backscattering and channeling spectroscopy turns out to provide interesting complementary

information concerning the determination of the total disorder density such as the polycrystalline fraction, foreign phase fractions and other defect structures such as stacking faults within the layer and disorder structures at the surface and at the interface. Information can be obtained on possible coherency strain in the film and its relieve by the formation of misfit dislocations with increasing film thickness. In the following these features will be discussed in some detail.

4.4 Growth on strontiumtitanate, SrTiO₃

Numerous groups have observed c-axis oriented growth of YBaCuO thin films on (100)SrTiO₃ using different deposition techniques. Highly textured films of the pure 1-2-3 phase are usually obtained. The main disorder component is a polycrystalline material fraction.

The amount of polycrystalline material in highly textured films depends on the substrate surface quality and on the substrate temperature and orientation. The influence of the substrate surface quality on the film growth performance is demonstrated in Fig. 4.10 [21]. In Fig. 4.10 (A) random and [100] aligned spectra of (100) SrTiO₃ substrates are shown. The sample providing the aligned spectrum (a) with $\chi_{\min} = 22\%$ was cut into three pieces which were annealed at 950°C in 1 atm O₂ for 1 h, leading to an improvement of the crystalline quality shown as spectrum (b) with $\chi_{\min} = 9\%$, and at 1300°C shown as spectrum (c) with $\chi_{\min} = 2\%$. The Sr surface peak areas decreased correspondingly. YBaCuO films were then deposited under optimized conditions resulting in c-axis oriented growth. In Fig. 4.10 (B) the backscattering spectra of these films which are labelled according to their corresponding substrates are displayed. The random spectrum is taken from film (c); it is similar for all the films except of small differences in the film thickness. The χ_{\min} values vary from 43% to 33% and further to 15% for the films on the substrates of increasing quality. Since similar χ_{\min} values were reproducibly obtained for the films on the substrates with similar quality, these results clearly demonstrate a strong dependence of the film growth on the substrate quality. X-ray diffraction measurements in the Seemann-Bohlin geometry reveal polycrystalline phase contributions for the films (a) and (b) while for the film (c) no lines could be detected indicating epitaxial growth (see chapter 3). A variety of other defect structures will contribute to χ_{\min} . This disorder will be discussed in more detail in section 4.8. Here we have to conclude that the polycrystalline fractions in samples (a) and (b) are smaller than 43% and 33%, respectively. The polycrystalline fraction extends throughout the total film thickness.

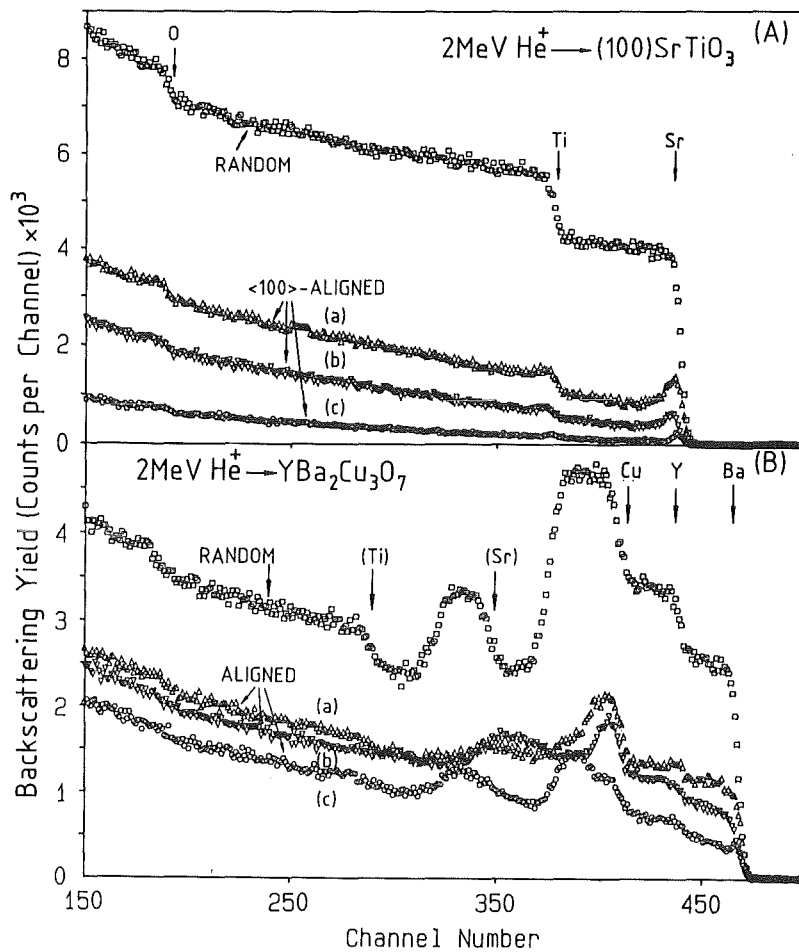


Fig. 4.10 (A) Random and $\langle 100 \rangle$ -aligned backscattering spectra from (100) SrTiO_3 substrates of different quality (χ_{\min} equals (a) 22%, (b) 9% and (c) 2%) and (B) c-axis oriented YBaCuO films deposited on these substrates (χ_{\min} for Ba equals (a) 43%, (b) 33% and (c) 15%).

Large polycrystalline fractions have also been observed in a-axis oriented films which were grown on (100) SrTiO_3 and on (100) MgO at low substrate temperatures. X-ray diffraction shows that the c-axis lattice parameter increases when the substrate temperature is lowered due to deviations from oxygen stoichiometry. The growth conditions for c-axis orientation might thus deteriorate and a-axis direction is preferred reducing the lattice misfit and guaranteeing the epitaxial growth of the film. Pure a-axis growth on (100) SrTiO_3 is obtained at substrate temperatures around 700°C . Fig. 4.11 shows random and aligned spectra for a film with the a-axis perpendicular to the substrate surface. The minimum yield for Ba is 22% indicating that 80% of the material is epitaxial. This is, however, considerably lower than single crystalline fractions of 96%

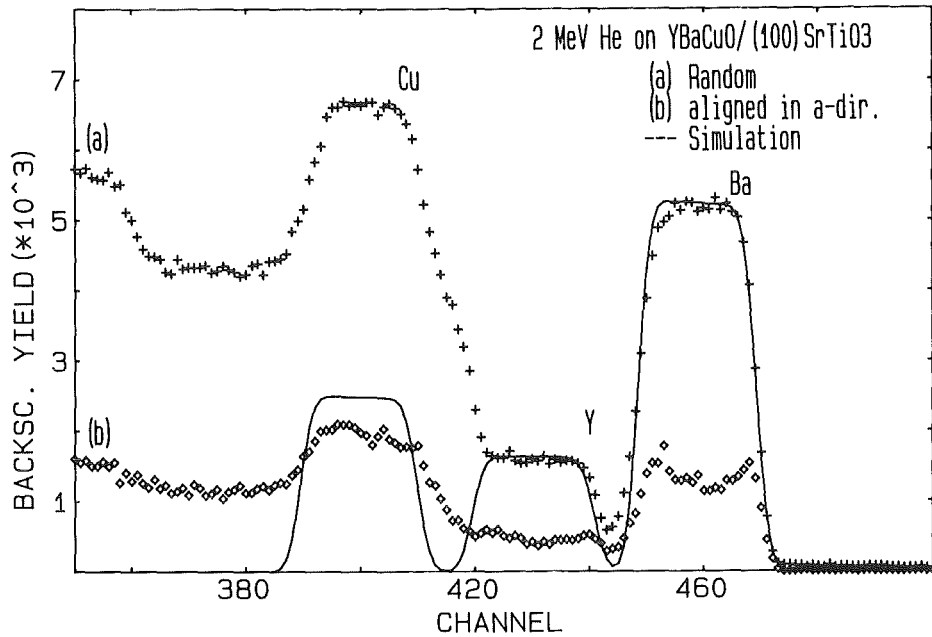


Fig. 4.11 Random and [100]-aligned backscattering spectra from an a-axis oriented YBaCuO film deposited on (100) SrTiO₃. Also shown is the simulation of the film composition (solid line).

observed for our best c-axis oriented films. As high quality substrates are used in both cases there must be other reasons to explain the difference. In principle, less perfect growth may occur at lower substrate temperatures due to the reduced surface mobility of the arriving atoms. It should be noted that the film composition also depends slightly on the substrate temperature. The Ba concentration decreases slightly with decreasing substrate temperature and the composition of the film shown in Fig. 4.11 is 0.95:1.45:3.0 (solid line). The change in composition however does not necessarily affect the growth performance as will be shown below. Energy-dependent minimum yield measurements for Ba using incident ion energies of 1.0, 1.5, 2.0 and 3.04 MeV did not reveal any change of χ_{\min} with energy which is expected for films with large polycrystalline material fractions. Energy dependent χ_{\min} -values have been observed for c-axis oriented films of higher quality as will be discussed below.

The growth of YBaCuO films on (110)-oriented SrTiO₃ substrates has been studied at temperatures of 700°C and 800°C. In these cases, the substrate orientation is imposed on the film growth, i.e., the films grew in the (110)-orientation. More precisely, a "pure" (110)-orientation has been observed at the lower deposition temperature of 700°C. At 800°C in addition to the (hh0)-lines also reflections of the (013) type appeared in the X-ray diffraction pattern.

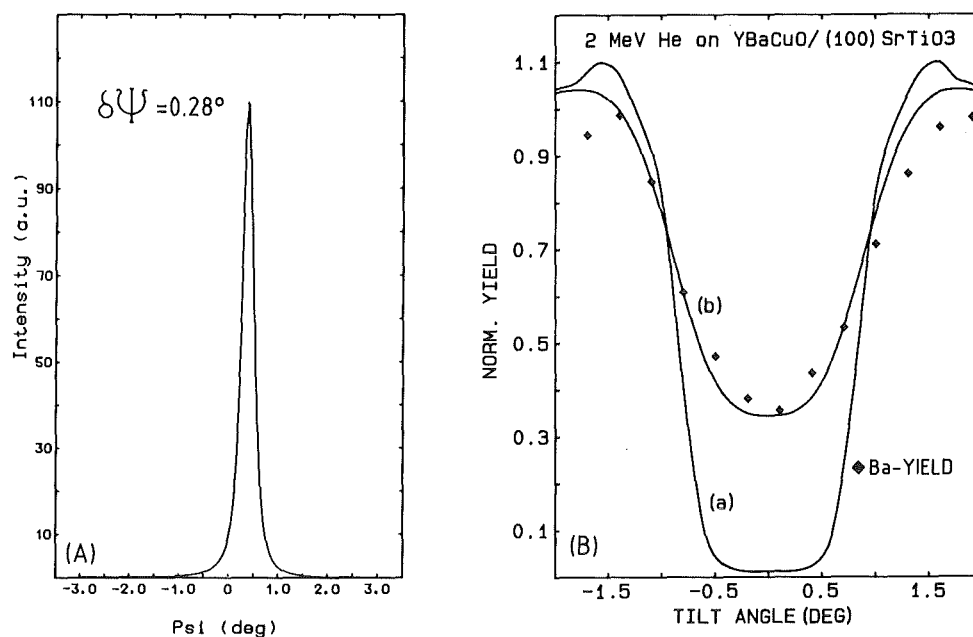


Fig. 4.12 (A) Rocking curve (ω -scan) of an YBaCuO film on (100) SrTiO₃. The scan was taken for the (005) line. The half width value is 0.28°.
 (B) Angular yield curve through the c-direction of an YBaCuO-film on (100) SrTiO₃ containing a large fraction of polycrystalline material. Included is the calculated dip curve of a defect free crystal (a) and after convolution and including defects (b).

Random and [110]aligned spectra for a (110)-oriented film revealed channeling behaviour but with a much poorer χ_{\min} -value of 56%. It should be noted that the composition near the surface of this film was far off stoichiometry (Y_{0.9}Ba_{1.35}Cu₃O_{7-x}) probably due to the high diffusion within the a,b plane. SEM pictures showed the presence of foreign phase material on the film surface in form of clusters. This may be the main reason for the deterioration of the χ_{\min} -value. For the (110)/(013) oriented films comparable spectra with a similar χ_{\min} values were obtained. It is interesting to note, however, that though the axial χ_{\min} values for both (110) and (110)/(013) directions were similar, planar channeling could only be observed in the (110) oriented films. In films with (110) oriented growth, cross-sectional transmission electron microscopy images reveal many linear contrast regions indicating a large amount of lattice defects or distortions [55].

4.5 Mosaic spread in films with polycrystalline fractions

The single crystalline grains in films containing large polycrystalline fractions are rather well aligned with the substrate orientation. The standard deviation from the mean growth direction is determined by X-ray diffraction (see

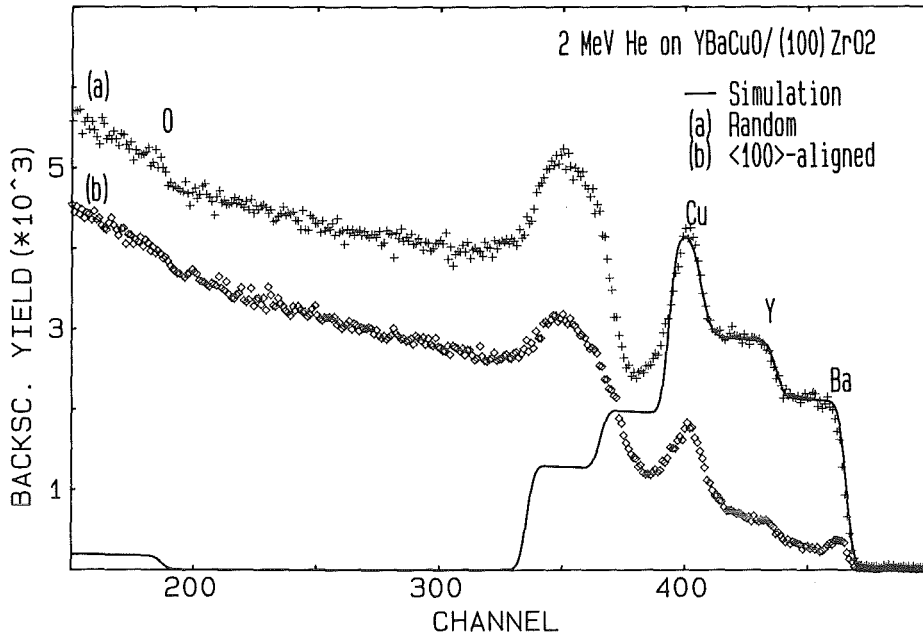


Fig. 4.13 Random and [001] aligned backscattering spectra from a c-axis oriented YBaCuO film deposited on (100) Zr(Y)O₂. The (100) planes of the film are aligned with the (100) planes of the substrate. The solid line presents a simulation of the film composition.

chapter 3) and by angular yield measurements. Both techniques have been applied using the same film and the results are shown in Fig. 4.12. The experimental angular yield data in Fig. 4.12(B) reveal a high minimum yield value of about 35% and the shape of the dip is more flat than that of the curve (a) which is calculated for a defect-free crystal. In order to fit the experimental data, curve (a) is first convoluted with a Gaussian curve, assuming a Gaussian distribution of the grain orientation with a standard deviation of 0.2°. The resulting convoluted dip curve, $\chi(\psi)$ is then used to determine the channeled beam fraction, $1-\chi(\psi)$, which is multiplied with a defect density of $N_D=33\%$ in order to determine the fraction of the beam which is transformed into a random component. This random component is finely added to the convoluted dip curve to obtain the solid curve (b) through the experimental data points. The mosaic spread obtained by ion channeling is in good agreement with that extracted from the rocking curve shown in Fig. 4.12(A). From the small value observed for the mosaic spread it may be concluded that there is no mutual interference during the growth of crystallites with different orientations.

4.6 Growth on (100) yttrium stabilized zirconia, $Zr(Y)O_2$

Although distortions have been observed at the (100) $Zr(Y)O_2$ surface (see section 4.2), the YBaCuO-films deposited onto these surfaces reveal a good single crystalline c-axis oriented growth. This is demonstrated by the random and [100] aligned spectra shown in Fig. 4.13. The minimum yield for Ba behind the surface peak is 12%. The best X_{min} value obtained up to now for films on $Zr(Y)O_2$ is 10%. The simulation of the composition (solid line): 0.95:1.5:3.0, indicates that a rather large Ba-deficiency does not necessarily affect the crystalline growth. The Ba-surface peak corresponds to 6.4 Ba atoms/row. This value indicates a rather large distorted surface layer (see section 4.10). The good crystalline growth is amazing as a large lattice parameter mismatch exists. The lattice parameter of $Zr(Y)O_2$ lies between 5.12 Å and 5.14 Å, depending on the Y-concentration. The lattice misfit can be reduced if the c-axis oriented growth is azimuthally adjusted in such a way that by a 45° rotation about the c-axis the (100) planes of the film are aligned with the (110) planes of the substrate. The distance of the lattice

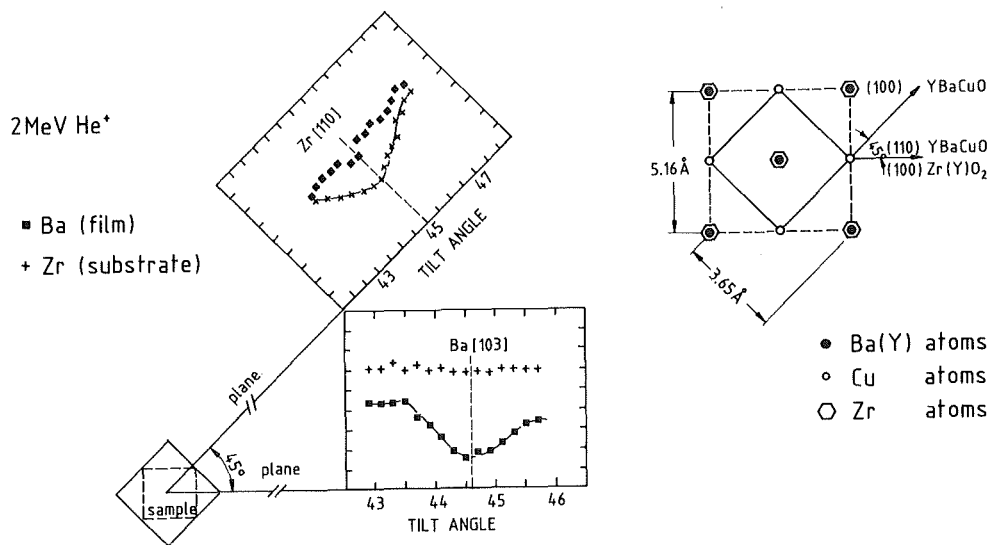


Fig. 4.14 Schematic representation of the azimuthal growth of epitaxial YBaCuO films on (100) oriented $Zr(Y)O_2$ substrates. A tilt from the axial channel ([100] substrate and [001] film) by 45° leads to a minimum in the scattering from the substrate ([110] channel) while a tilt by 44.6° in the same direction after rotation of the sample by 45° in the film plane leads to a minimum in the scattering from the film ([103] channel) (left part of the figure). This shows that the film growth with the [110] direction aligned with the [100] direction of the substrate leading to an improved lattice matching (right part of the figure).

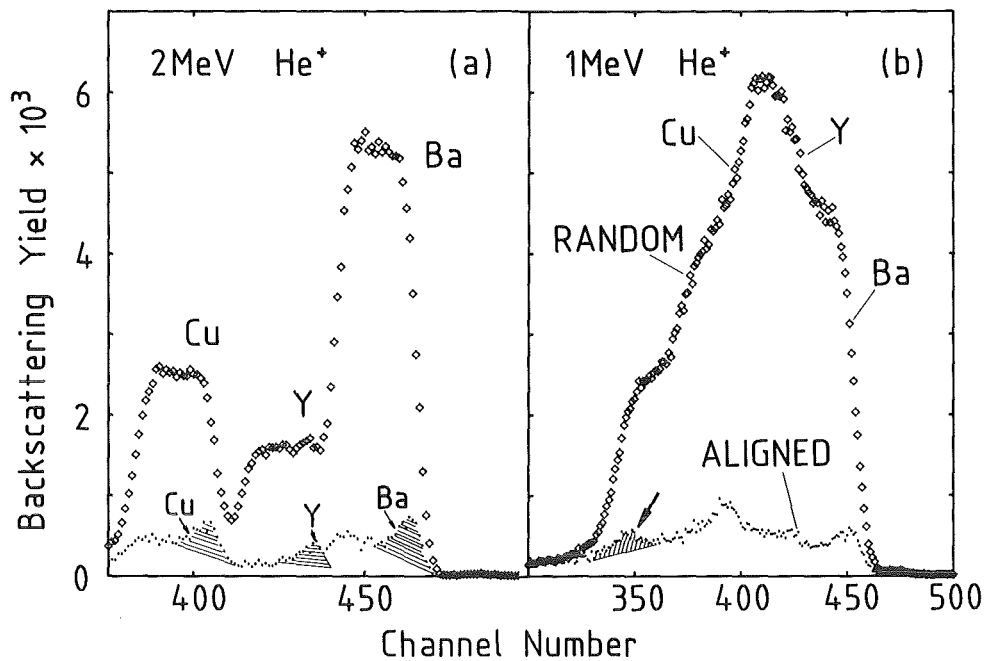


Fig. 4.15 Sections of random and aligned backscattering spectra of a 100 nm thick YBaCuO film on MgO measured with 2 MeV (a) and 1 MeV (b) He ions. The hatched areas in the aligned spectrum of (a) indicate the surface peak yields for different masses while that marked by an arrow in (b) arises due to enhanced dechanneling at the film-substrate interface.

planes along the [110]-direction is 3.62 Å resulting in a lattice misfit of about 7%. Inclined channeling proved this growth behavior as shown in Fig. 4.14. Following the (100) plane of the film with the analysing beam a dip in the backscattered yield is observed near 45° due to the [103] axis of the film however no dip occurs for the substrate (110) plane at 45° as expected. Following the (110) plane of the film this behavior is just opposite: no dip in the film but for the substrate due to the presence of the [110] axis.

4.7 Growth on (100) magnesiumoxide, MgO

Low mass substrates such as MgO are especially well suited for the analyses of deposited films as the He ions backscattered from the substrate and the film are well separated in energy. Further, the single masses can be resolved if the films are sufficiently thin and the disorder can then be studied separately for each metal sublattice in YBaCuO. In Fig. 4.15 random and [100] aligned backscattering spectra of a 100 nm thick film taken with 2 MeV and 1 MeV He⁺ ions are displayed for illustration. The mass separation in the spectrum taken with 1 MeV He⁺ ions is poorer instead a better depth resolution is achieved (Fig.

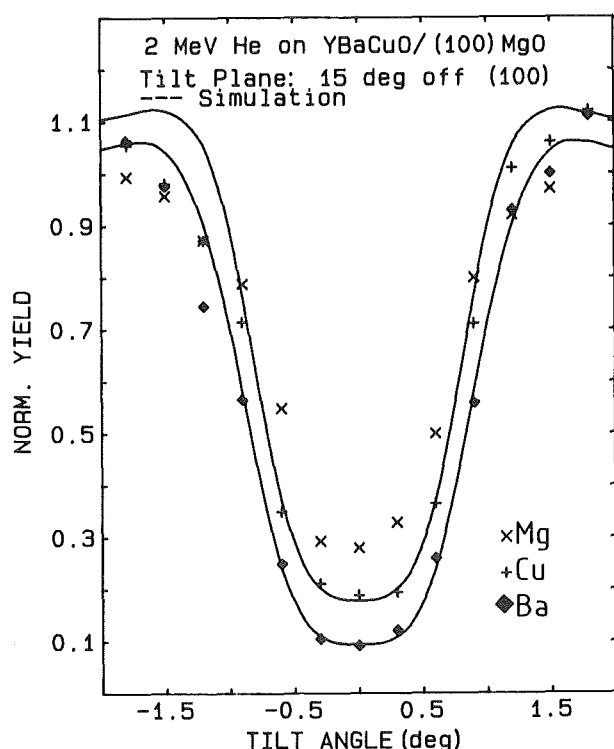


Fig. 4.16
Angular yield curves of Ba and Cu-atoms through the [001] direction of an YBaCuO film and of Mg atoms through the <100> direction of the MgO substrate. The solid curves were obtained by Monte Carlo simulation.

4.15b). The composition of the film was close to the 1-2-3 stoichiometry with maximum deviations of 10%. The aligned spectra show a large reduction of the backscattering yield throughout the film thickness. Quantitative values may be deduced from Fig. 4.16 where angular scans taken with 2 MeV He⁺ ions through the [001] direction are shown for scattering by Ba and Cu from the film and by Mg from the substrate. The χ_{\min} value of 7% determined for Ba (3.5% have been reported for bulk single crystals in ref. 56, and we have found 4% for YBaCuO films on (100) SrTiO₃) reveals the rather good crystalline order achieved on (100) MgO substrates. While the χ_{\min} value of 8% for Y is close to that of Ba, a relatively high value of 16% was determined for Cu, reflecting some extra dechanneling in the Cu sublattice.

The solid lines drawn through the data points of Fig. 4.16 are the result of Monte Carlo simulation calculations. The angular half width values, $\psi_{1/2}$ obtained in the simulation (0.89°) agree with the measured values within experimental error. A Gaussian distribution of the misorientation of the crystallites with a standard deviation σ was assumed in the calculations. σ values of 0.1° and 0.2° for Ba and Cu, respectively, gave best fits to the experimental data. The small σ values reveal a mosaic structure with a narrow directional

distribution of the crystallites, again showing the good epitaxial growth quality of the films on MgO. Since the minimum yield values for the film and the substrate appear at the same angular position, the c-axis of the film is perpendicular to the substrate surface to within the error of the determination of the minima in the scans (0.05°). Rocking curves (ω -scans) support the findings in channeling simulation analysis. The mosaic spread of 0.22° (half width) in the thick film corresponds almost exactly to the channeling data for Ba if the standard deviation σ is converted to the half width of the distribution. The increase of the spread in the thin film is in accordance with the formation of dislocations as detected in the channeling experiments discussed below.

4.8 Intrinsic defect structures

It is a general observation that films with χ_{\min} -values of about 15% and below do not reveal polycrystalline material fractions visible with X-ray diffraction. Therefore χ_{\min} -values above about 1%, which is the calculated value for a perfect crystal have to be attributed to the presence of other defect structures. Such defects have been detected by transmission electron microscopy in $\text{YBa}_2\text{Cu}_3\text{O}_7$ and are summarized below in order to provide a basis for the interpretation of the channeling results. The planar stacking fault which is often observed is caused by the incorporation of extra $(\text{CuO})_2$ -double layers leading to a lattice shift either by $a/2$ or by $b/2$ which occurs with about equal probability [57]. Such stacking faults would contribute to the dechanneling yield in equal amounts to all metal sublattices. Cationic disorder in localized regions of 1 to 2 nm have been observed and explained by edge-sharing CuO_4 groups [58]. Cross section HTEM studies on our films revealed a similar kind of defect structure [59], which provides extra scattering from Cu atoms displaced from the rows in strain regions at the edge of this defect. Besides planar defects, small disordered regions bordered by edge dislocations have also been observed [60]. Assuming that these disordered regions would contain some extra CuO_x -precipitates, such defects could explain the enlarged χ_{\min} -values for the Cu-sublattice discussed above. Dislocations would result in energy dependent minimum yield values as observed for some of our films [50] which will be discussed in more detail below. Ordered planar defect structures, similar to stacking faults may occur in epitaxially grown YBaCuO-films and may even give rise to a new structure, called the 2-4-8 structure [61]. From X-ray analyses of our films we can exclude the existence of the 2-4-8 phase in our films. Other defect structures which have been observed by TEM studies in thin films are out-of-phase boundaries and twin boundaries [62]. In this work the out-of-phase boundaries were mainly observed for a-axis oriented films. About

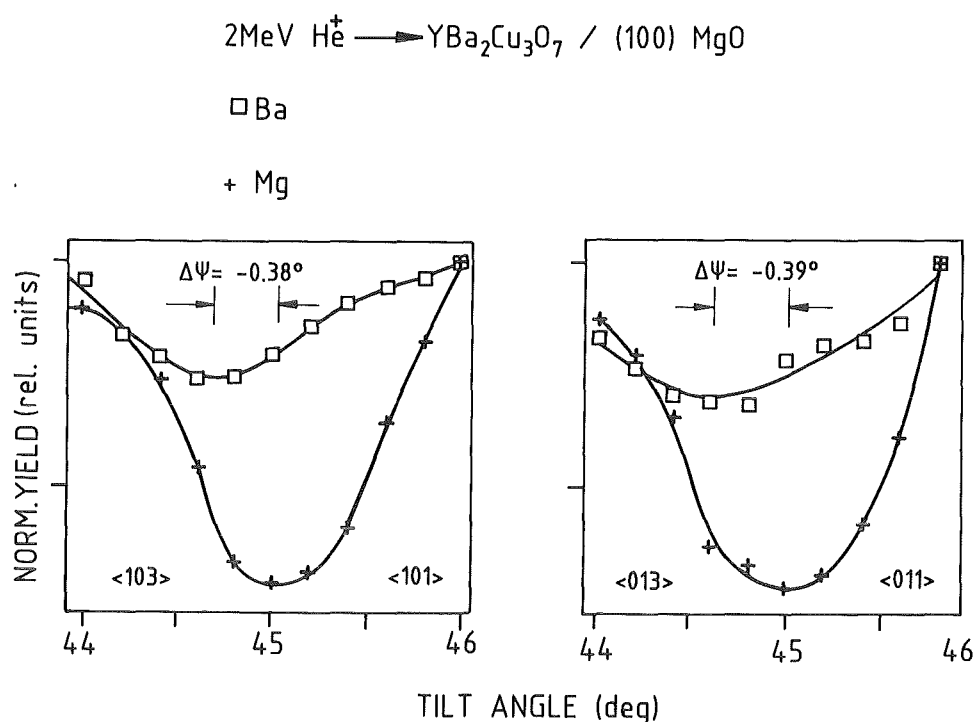


Fig. 4.17 Angular yield curves through the [103] and [013] directions of an c-axis oriented YBaCuO film and through the corresponding <101> and <011> directions of the MgO substrate.

80% of the sample area was a-axis oriented in good agreement with the χ_{\min} -value of 22% observed for our a-oriented films. The phase transition from tetragonal to orthorhombic structures always leads to the formation of (110) mirror twins which may occur either along the [100] or the [110] direction. The a- and b-axes are interchanged across the twin boundary. The existence of twins in our c-axes oriented films can directly be determined using inclined channeling at 45° along perpendicular (100) planes and by measuring the difference of the minima of the angular yield curves through the [110] substrate direction (45°) and the [013] or [103] film directions ($\arctg(a/c/3)=44.48^\circ$, $\arctg(b/c/3)=44.95^\circ$). The results of such measurements are presented in Fig. 4.17. The angular yield curves through the [013] as well as through the [103] direction reveal a similar shift from the [110] direction of the substrates which clearly indicates that a mixture of a and b directions exists in our films. It cannot be decided, however, if mirror twins occur within one grain or if grains with different a and b directions are present.

As discussed in section 4.1 the energy dependence of the minimum yield should provide some information on the most prominent defect component in the films. Fig. 4.18 shows a collection of data from various films on different substrate

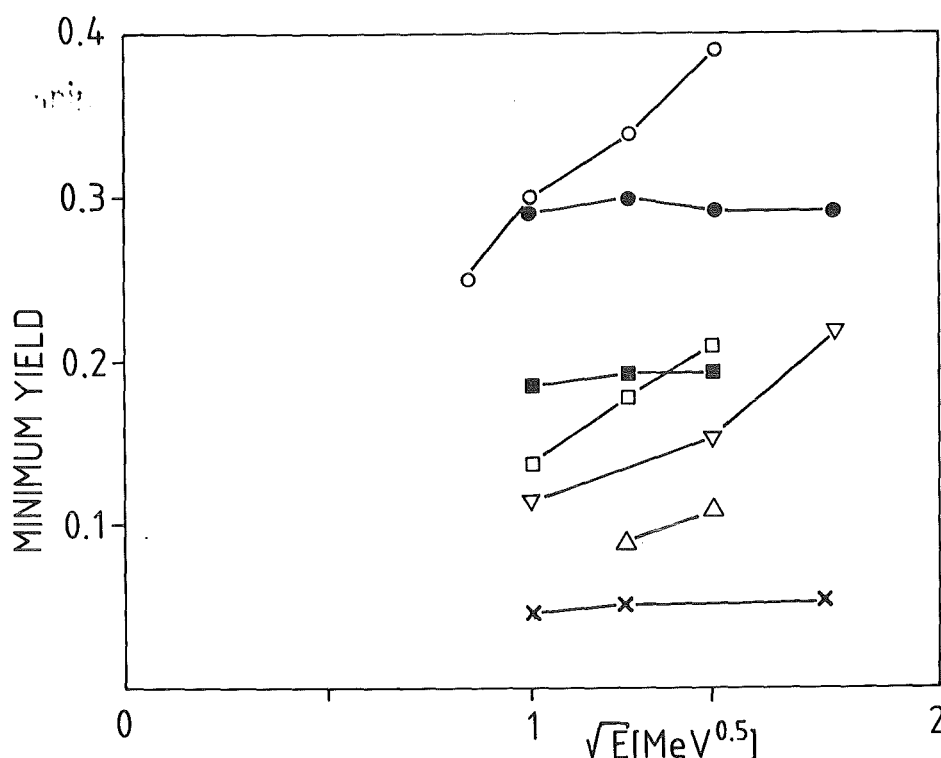


Fig. 4.18 Minimum yield values behind the Ba-surface peak as a function of the square root of the incident He ion energy.

material. The minimum yield values for Ba are displayed as a function of the square root of the analyzing beam energy. A linear dependence and a decrease of χ_{\min} with \sqrt{E} would indicate the existence of dislocations while an energy independent behaviour would indicate the existence of stacking faults and polycrystalline material fractions especially for large χ_{\min} -values. For these cases the polycrystalline fraction could be detected by X-ray diffraction (see chapter 3). For some films which show a linear decrease, the extrapolation to zero energy hits the zero point indicating that only dislocations are present, while other films point to a mixture of defects. For the best film the energy dependence is weak and does not extrapolate to zero. For such a case the existence of stacking faults is most probable.

In general, it can be noted from the literature that the occurrence of a special defect structure depends to a large extent on the thin film preparation methods. Therefore it seems difficult to draw general conclusions by comparing defect structures of films produced by different deposition processes. In our films small defects (3-5 nm in diameter) with double Cu-O planes and distorted edge regions

prevail. This distorted region would provide extra scattering from Cu atoms and would reveal a decrease of χ_{\min} with decreasing analyzing beam energy in agreement with the channeling results.

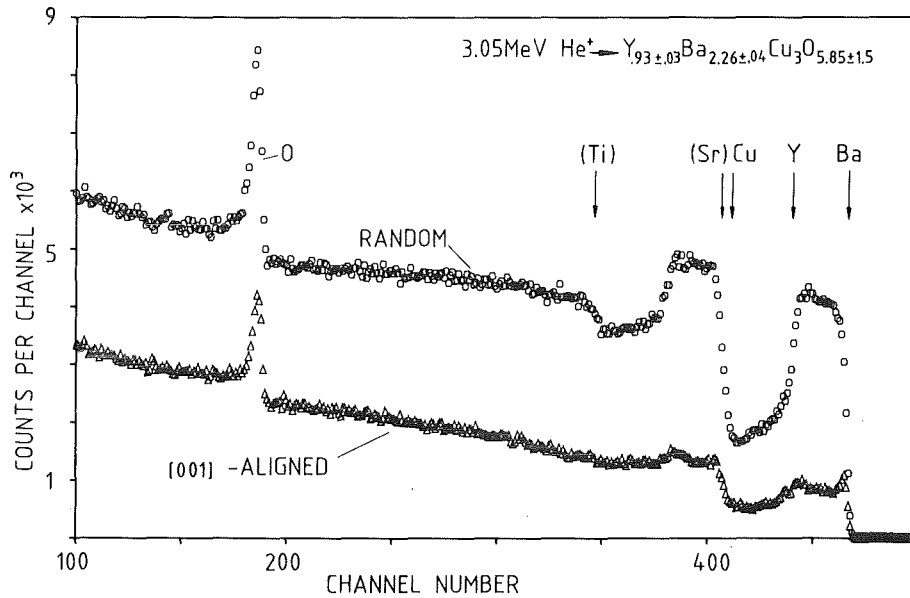


Fig. 4.19 Random and [001] aligned backscattering spectra from an YBaCuO film on (100) SrTiO₃ in the tetragonal phase using an incident He ion energy of 3.05 MeV [79].

4.9 Disorder in the tetragonal phase

The question arises if the defect structures discussed above were already present in the tetragonal phase or had been produced during the transformation from the tetragonal to the orthorhombic phase which is accompanied by twin formation. He-ion channeling and backscattering studies have been performed for the tetragonal structure. In Fig.4.19 the random and [100] aligned backscattering and channeling spectra are presented for the tetragonal phase. From the perfect matching of the aligned spectrum from the film and the substrate region a strain-free growth of the tetragonal YBa₂Cu₃O_{7-x} phase on (100)SrTiO₃ can be deduced. From the step heights of the different components and from the peak area of the oxygen resonance peak the composition of the sample can be obtained. The analyzing beam energy can be varied in order to facilitate the determination of the different components. At 3.05 MeV the oxygen component is determined from the enhanced sensitivity due to the oxygen

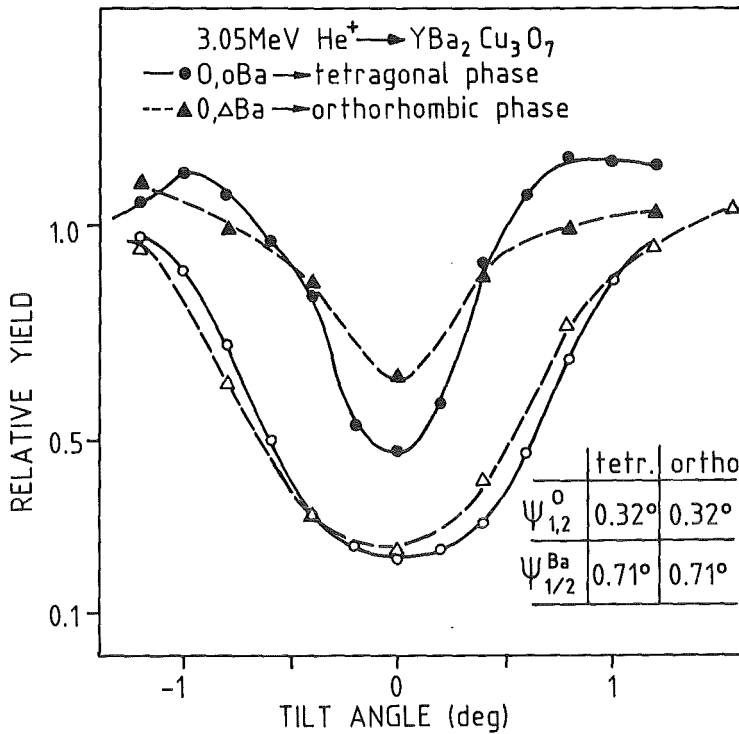


Fig. 4.20 Angular yield curves through the [100] and [001] axial directions of YBaCuO thin films in the tetragonal and orthorhombic phase. The angular yield curves are shown for Ba and for O [79].

resonance peak [50] while the metal content is most easily determined from the step heights measured at 2 MeV incident He-energy. The composition of the film shown is $Y_{0.9}Ba_{2.3}Cu_3O_{5.9}$. The normalized minimum yield values for Ba as determined from the ratio of the yield heights below the surface peak and for oxygen from the ratio of the peak areas of the oxygen resonance peaks are 20% and 48%, respectively. In order to get more detailed information the angular yield curves were determined using a tilt plane 15° off a (100) plane. The results of these analyses for the Ba and the oxygen sublattice are shown in Fig. 4.20 in comparison to those previously obtained for the orthorhombic phase [50]. It can be seen that the critical angle and the minimum yield values for the Ba sublattice are rather similar in both phases while there is a large difference for the minimum yield values of oxygen which are 65% and 48% for the orthorhombic and for the tetragonal phase, respectively. From Monte Carlo simulation calculations it can be inferred that about half of the difference of the X_{min} -values for the oxygen sublattices can be attributed to the enhanced mean vibrational amplitudes of the oxygen atoms in the chain positions in the orthorhombic phase. Since the minimum yields of the metal sublattice are similar in both phases, it

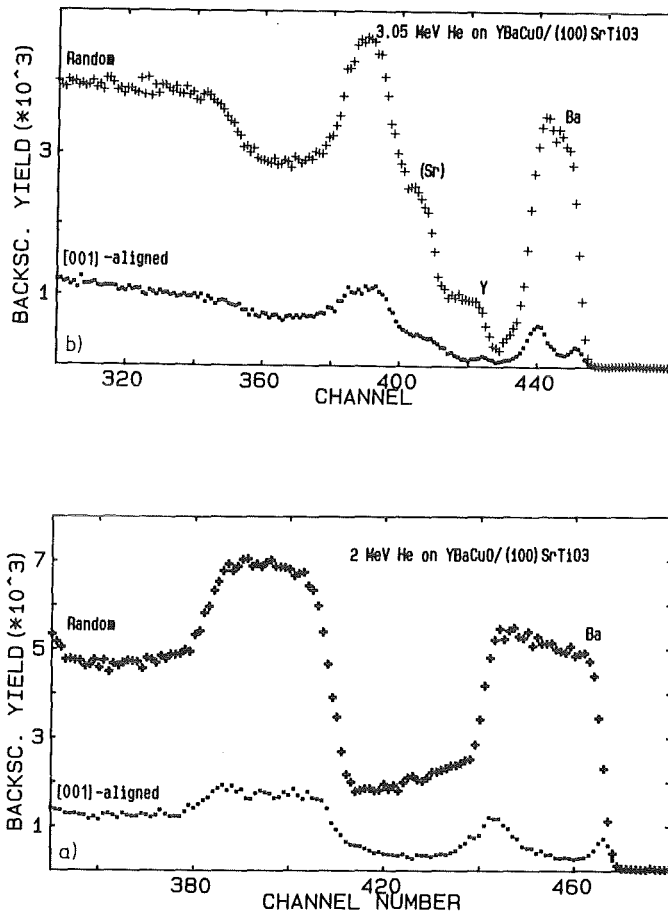


Fig. 4.21 Random and [001] aligned back-scattering spectra from a 100 nm thick YBaCuO film on (100) SrTiO₃, measured with different He ion energies (a: 2 MeV, b: 3.05 MeV).

can be concluded that defects are already produced during the growth of the tetragonal phase.

4.10 Surface peak of YBaCuO

The analysis of the surface peak areas (SPA's) provides interesting results about the disorder at the surface. As an example one of our best results is shown in Fig. 4.21(b) at 3.05 MeV where the surface peak yield provides a measure of the number of atoms exposed to the incident beam on the surface. The Ba surface peak in Fig. 4.21(b) corresponds to 1.8×10^{15} Ba atoms/cm² which is equal to 2.7 Ba atoms/row. Subtracting the contribution of a perfect surface including thermal vibrations of about 2.2 Ba atoms/row (see Fig. 4.4) gives about 0.3 displaced Ba atoms per row. From this a disordered layer thickness of about 0.5 nm can be

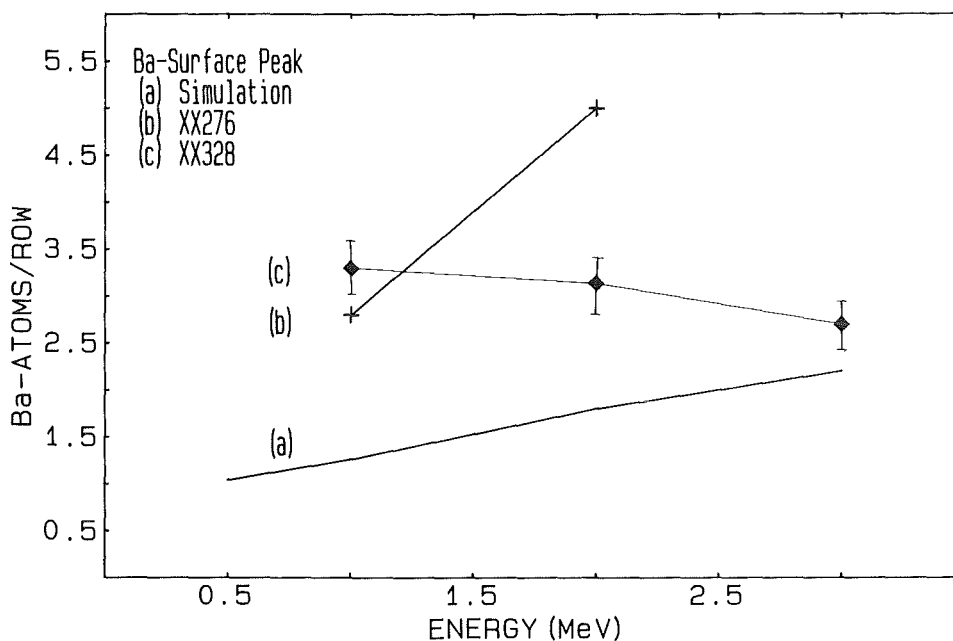


Fig. 4.22 Surface peak area in Ba atoms/row as a function of the analyzing beam energy for two YBaCuO thin films.

estimated, assuming the 1-2-3 composition. The latter assumption is justified by the analyses of the surface peaks for Y, Cu and Ba shown in Fig. 4.15. A ratio 1:1.7:3.1 close to stoichiometry is obtained. This indicates that there is no extra Ba_xO_y at the surface. It should be mentioned however, that the analyses of 15 SPA's provided an average value of about 4 extra Ba atoms/row corresponding to a disordered surface region of about 2 nm. It turned out, however, that this larger SPA's were energy dependent indicating partially ordered growth with respect to the bulk of the film. The nature of this ordering is yet not clear, but it implies that the above estimates of disordered surface layer thickness should be considered as preliminary. In contrast, the smallest SPA did not show a strong dependence on energy as can be seen in Fig. 4.22 where a comparison is given for two films with quite different SPA's at 2 MeV. The results shown in Fig. 4.22 clearly indicate that quite different defect structures exist at the surface. The arrangement of the planes certainly also plays a role in the analysis. For sample XX328 the SPA of Y could be analyzed at 3.05 MeV and a value of about 0.85 Y atoms/row was obtained. From this number being smaller than unity and which would be still reduced considering the contribution of thermal vibrations it is concluded that the uppermost layer does not contain Y. A more detailed analysis may provide additional information in future.

4.11 Misfit strain and misfit dislocations

Since the lattice mismatch between YBaCuO and the MgO substrate is very large ($\sim 9\%$), coherency strain is expected in very thin films. With increasing film thickness such strain may be relieved by the formation of misfit dislocations. Axial channeling is a valuable tool to detect strain as well as misfit dislocations at interfaces [38]. The existence of disorder at the film substrate interface for the YBaCuO/MgO system is indicated already in the [001] aligned backscattering spectra displayed in Fig. 4.15. In the spectrum measured with 1 MeV He⁺ ion energy (Fig. 4.15 (b)) an appreciable increase in the dechanneling yield appears near the back edge of Cu. Since the back edge of Ba overlaps with the front edge of Cu, the corresponding increase of the Ba yield cannot be separated from the Cu surface peak in this spectrum, however, at least is partly resolved in the spectrum of 2 MeV He⁺ ions (Fig. 4.15 (a)) and for 3.05 MeV He⁺ ions (Fig. 4.21 (b)).

For a further study of strain relief and a characterization of the defect structure at the interface, channeling experiments have been performed as a function of the analyzing beam energy and the film thickness. The energy dependence of the dechanneling yield allows at least qualitatively to distinguish between the main defect structures in a material, while from the thickness dependence we intended to determine the critical film thickness for strain relief. In the initial state of growth the lattice parameters of the film a ($a = 3.8231 \text{ \AA}$), and b ($b = 3.8864 \text{ \AA}$) will tend to expand to match the larger lattice constant of the MgO substrate ($a = 4.21$), and the c -axis will be compressed according to the Poisson effect. This compression will change the angle between the [013]/[103] direction in the film (accessible for channeling for c -axis oriented films) and the [110] direction in the substrate. The estimated change is several degrees and should be easily detected by axial channeling. Therefore angular scans through inclined crystal directions were performed on a 17 nm thick film and the results are presented in Fig. 4.23. The angular yield curves for Ba and Mg obtained for normal incidence are shown in Fig. 4.23(a) while Fig. 4.23(b) represents the results for inclined incidence. The observed difference in the minima of the scans of about 0.4 degree for inclined incidence, however, can be attributed to the deviation of the [013]/[103] direction ($\arctan(a/c/3) = 44.5^\circ$) from the [110] substrate direction (45°) calculated for an unstrained film. Thus the expected additional shift well above 1° has not been observed and we conclude that strain has already been relieved for films on MgO. For films on SrTiO₃ with a lattice constant of 3.905 \AA the lattice misfit is much smaller (2% for the a -direction)

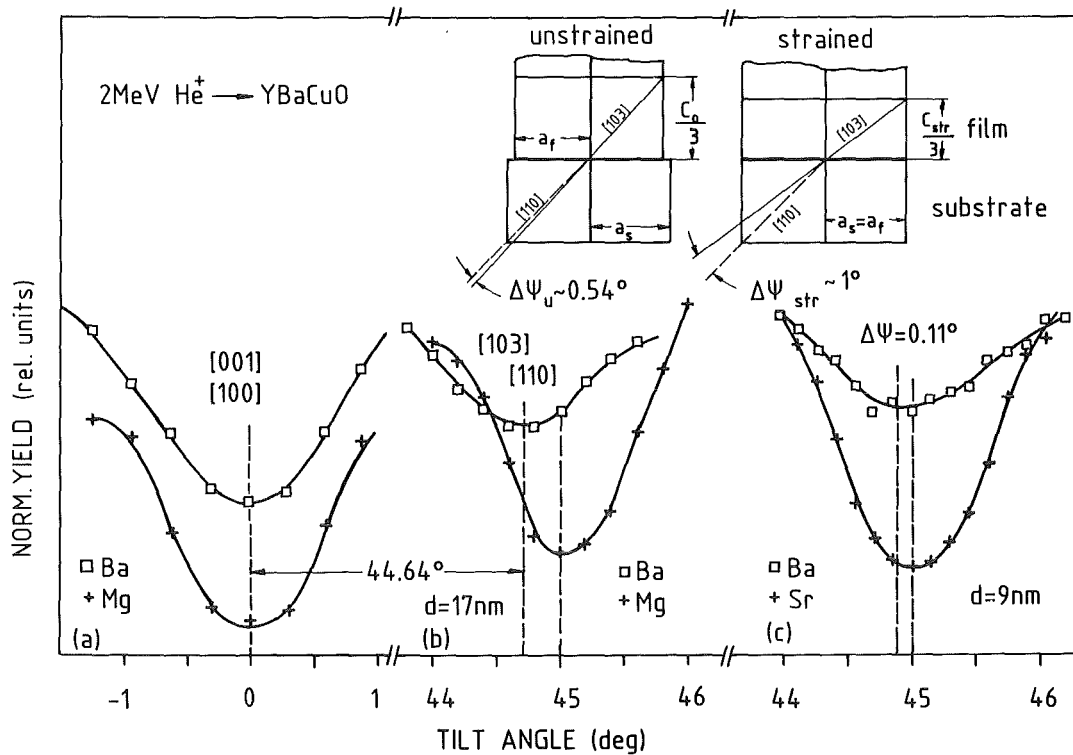


Fig. 4.23 Angular yield curves of an YBaCuO film (Ba signal) through different directions. (a) For perpendicular incidence ([001] and [100] scans for film and substrate (Mg), resp.). (b) For inclined incidence ([103] and [110] scans). (c) For inclined incidence ([103] and [110] scans for film and substrate (Sr), resp.). The expected shifts for unstrained ($\Delta\psi_u$) and strained ($\Delta\psi_{str}$) films are shown in the inset.

resulting in less strain and a corresponding small shift in the angle of about 1° at most. The results for a 9 nm thick film on (100) SrTiO₃ are shown in Fig. 4.23(c). A small shift of about 0.3° is seen, indicating that the layer is partially strained and that a partial commensurate growth occurs.

Our conjecture that strain is relieved by the formation of misfit dislocation is supported by the energy dependent analysis of the dechanneling behaviour. The minimum yield values, χ_{min} , for Ba of films on MgO with different thicknesses have been measured. The χ_{min} -values decrease with decreasing energy as shown in Fig. 4.24. The strongest dependence is observed for the thinnest film and the linear dependence on \sqrt{E} proves the presence of dislocations. With increasing thickness the energy dependence of the dechanneling yield becomes much weaker and is almost constant at a thickness of 100 nm. Here the χ_{min} values can be resolved from the interfacial region in the backscattering spectra, and the independence on energy indicates that the principal defect structure are stacking faults, as has been discussed above for thick films (see Fig. 4.18). The increase of

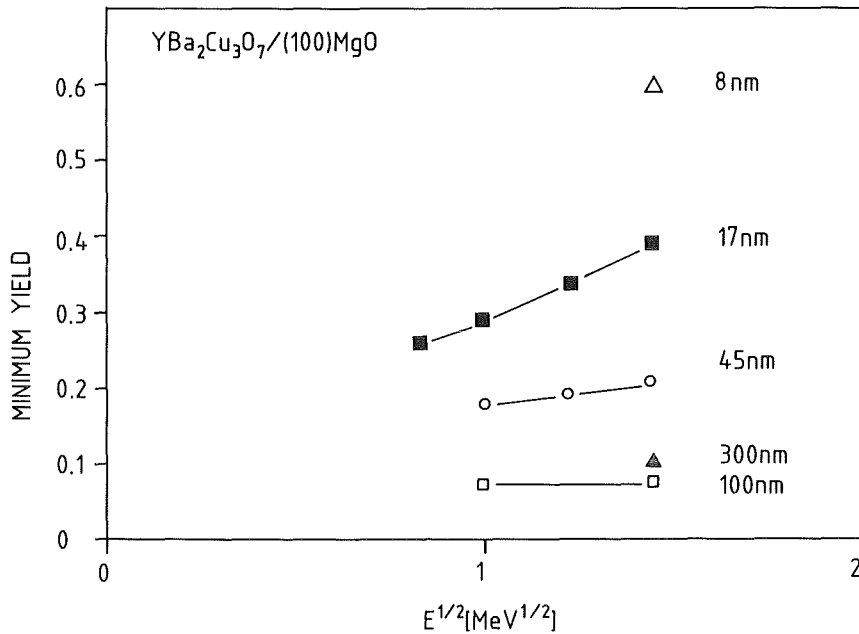


Fig. 4.24 Dechanneling yield values versus the square root of the analyzing beam energy, E , for YBaCuO films of different thickness on (100) MgO substrates.

χ_{\min} with decreasing film thickness is smaller for films on SrTiO₃. In Fig. 4.25 the random and [001]-aligned spectra for two films on (100) SrTiO₃ and (100) MgO are shown for comparison. The minimum yield values, χ_{\min} in both films are considerably larger than our best values of 5% and 7% observed so far in thicker films on SrTiO₃ and MgO, respectively. This is partly due to a contribution of disordered material at the film surface consisting on the average of about 4 and in better cases of about 2 displaced Ba atoms/row at 2 MeV and to interfacial dechanneling. Since the disordered surface is thought to contribute equally to χ_{\min} on both substrates, the different minimum yield values in films on SrTiO₃ and MgO reflect the different effects of dechanneling at the film-substrate interface. The large lattice mismatch between YBa₂Cu₃O_{7-x} and the MgO substrate causes extreme strain in the film at the interface which is immediately relieved by forming misfit dislocations. From the effective extra interfacial dechanneling we have estimated that a dislocation layer of a few nm thickness had formed which may be non-superconducting. In contrast, c-axis oriented YBa₂Cu₃O_{7-x} matches quite well with the (100) surface of SrTiO₃. Therefore commensurate growth is achieved such that good crystalline order is readily built up in the very first layers. The occurrence of strain was directly observed by inclined-direction channeling at 45° from the surface normal in a 9 nm thick film (Fig. 4.23 (c)), but

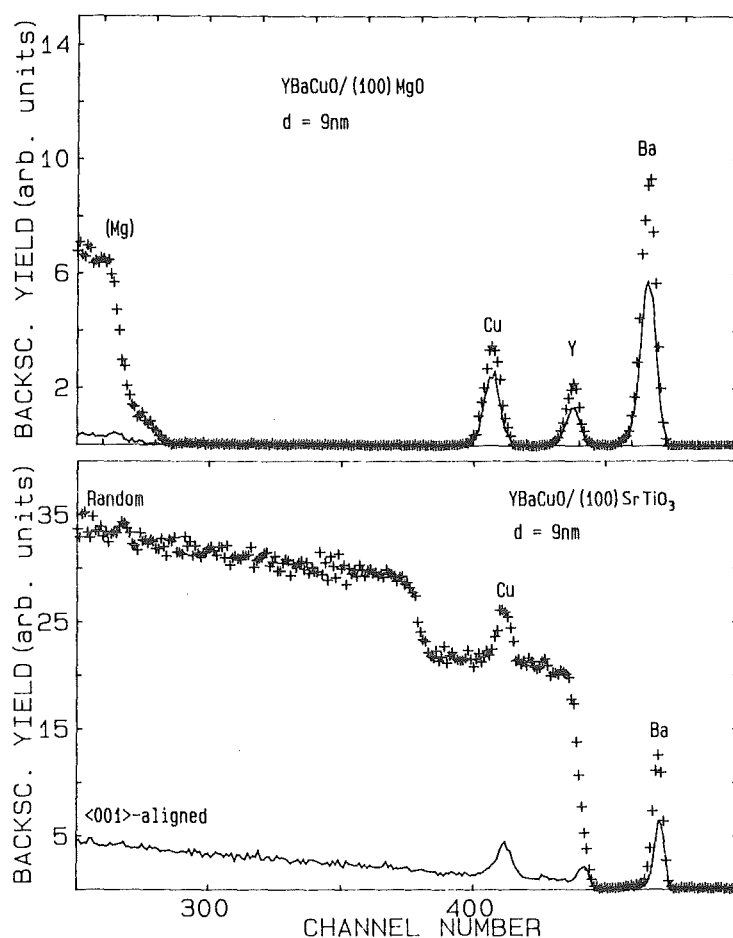


Fig. 4.25 Random and aligned backscattering spectra for 9.0 nm thick YBaCuO films on (100) SrTiO₃ (lower) and (100) MgO (upper) substrates.

not in films with thicknesses above 13 nm. Due to the additional interfacial layer containing dislocations in films on MgO the superconducting path breaks down already in thicker films than on SrTiO₃ when the film thickness is decreased (see chapter 5).

4.12 Concluding remarks

Ion channeling and backscattering spectrometry has provided valuable information on many aspects of the synthesis and analysis of high quality superconducting YBa₂Cu₃O₇ thin films. Sputtering parameters such as cathode voltage, gas pressure in the discharge, sputter gas ratio Ar/O₂ and substrate temperature have been optimized in such a way that films with stoichiometric compositions were grown. Film compositions and interface reactions were monitored in different annealing treatments in order to stimulate the various

phase transitions from the amorphous to the tetragonal and finally to the high T_c orthorhombic phase. The He ions resonance on oxygen at 3.04 MeV is appropriate to monitor the oxygen content on a reasonable level of accuracy.

He ion channeling in combination with Monte Carlo simulation calculations leads to the evaluation of the crystalline properties of the single crystalline SrTiO₃, MgO and ZrO₂ substrates. Nearly defect free substrate surfaces are a necessary precondition for optimized single crystalline film growth. The main disorder structures which have been observed in the as-deposited YBaCuO films and which would be in accord with the dechanneling measurements were polycrystalline material fractions, dislocations, stacking faults, and small planar defects with double Cu-O layers and with strain regions at the edges. The mosaic spread of the oriented single crystalline regions is small ($\sigma \leq 0.2^\circ$) and does not depend on the disorder density in the film. Twinning is observed in c-oriented films by inclined channeling, although it is not possible to decide if these (110) mirror twins are within the crystallites or due to different orientations of crystallites.

Optimal growth was observed for c-oriented films with best minimum yield values of 5% at 2 MeV and 4.5% at 3 MeV He ion energy. This is only slightly worse than minimum yield values of 2% to 3% observed for YBaCuO single crystals. The best values for the surface peak area were obtained at 3 MeV He ion energy and correspond to 0.6 extra Ba atom/row indicating that the disordered layer thickness is about 0.6 nm. It should be noted, however, that an average value of about 2 nm for the disordered surface layer thickness is observed. The interfacial disorder which can be attributed to misfit dislocations depends on the lattice parameter mismatch and is smallest for films on (100) SrTiO₃. Films on (100) SrTiO₃ of 9 nm thickness and below are partially strained indicating commensurate growth.

5. SUPERCONDUCTING PROPERTIES

The superconducting and normal conducting properties of the films, i.e. the superconducting transition temperature, the transition width, the critical current density, the residual resistivity or residual resistivity ratio strongly correlate with the growth quality characterized by channeling and diffraction experiments in the preceding chapters. Besides the substrate material, the substrate temperature, T_s , was under otherwise optimized deposition conditions an important parameter determining the film properties.

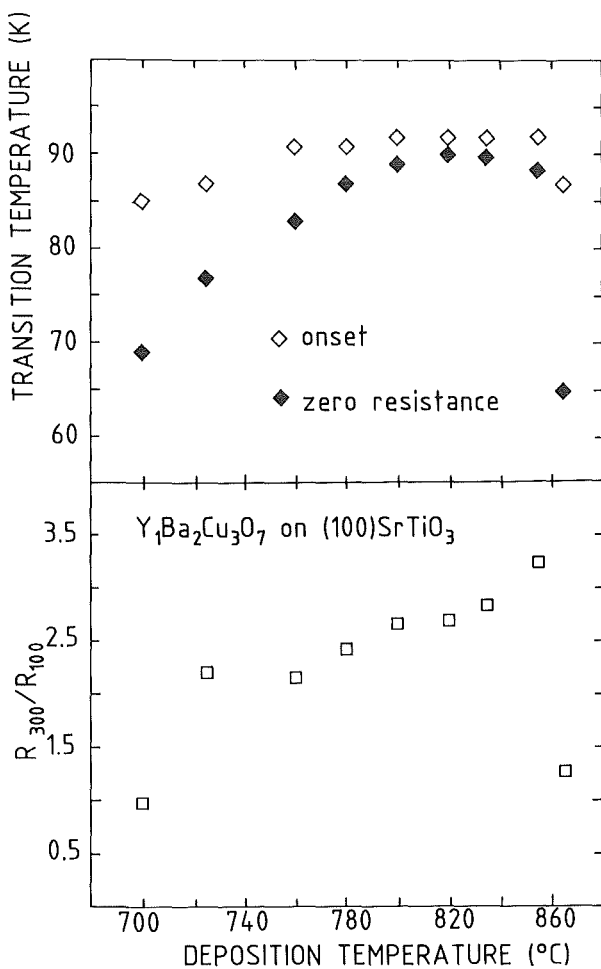


Fig. 5.1
upper: Onset and zero resistance points of transition curves to superconductivity of YBaCuO films deposited on (100) SrTiO₃ substrates versus deposition temperature. lower: Residual resistivity ratio, R_{300}/R_{100} , of the films.

5.1 Transition temperatures and transport properties

We show as a first example the transition temperature (onset and zero resistance values) and the resistance ratio of films deposited on (100) SrTiO₃ substrates as a function of T_s in Fig. 5.1. It can be seen that the optimum temperatures for the preparation of high T_c films with narrow transitions are in the range of 780°C-850°C. The best value achieved for the completion

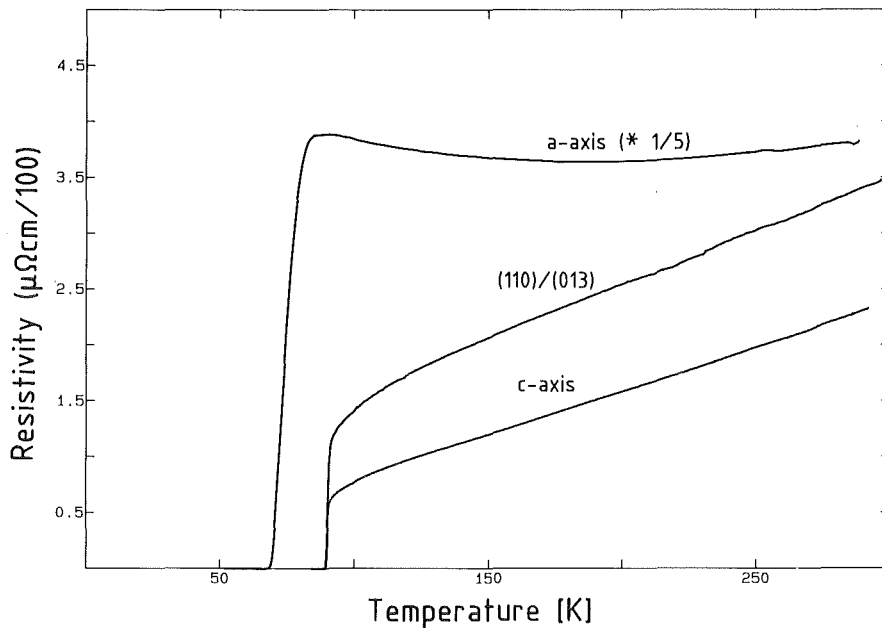


Fig. 5.2 Resistivity versus temperature curves of three YBaCuO films deposited on SrTiO₃ substrates having different growth directions as indicated in the figure.

temperature T_{c0} was 91 K with a transition width, δT_c , of 0.5 K. This temperature range coincides with pure c-axis epitaxial growth. Higher deposition temperatures leading to second phase formation do not considerably influence the onset temperature but strongly depress the completion temperature thus leading to enhanced transition widths. Also the appearance of a-axis oriented grains and the pure a-axis oriented film are characterized by slight depressions of the T_c onset values and enhanced decreases of the completion temperature. We explain this behaviour on the basis of the increased c-axis lattice parameter; the films deposited at lower T_s do not have a stoichiometric oxygen concentration, and probably also an inhomogeneous distribution is present with degraded material surrounding grains of higher T_c . The resistance ratio shows that best electrical transport again occurs in films with pure c-axis orientation. Our best resistivity values ($T = 100$ K) in films on (100) SrTiO₃ were around 60 $\mu\Omega\text{cm}$.

The transport properties in dependence of the film orientation on SrTiO₃ substrates are shown in Fig. 5.2 where the resistivity is displayed as a function of temperature for three films having (001), (110)/(013) and (100) orientations. The (001) and (110)/(013) oriented films reveal metallic behaviour, while the transport in the a-axis film is slightly temperature activated. The enhanced resistivity in this film is in accordance with the strong anisotropy of transport

properties observed in single crystal measurements [63,64]. This anisotropy may be partly reflected also in the (110)/(013) film showing higher resistivity than the c-axis textured film. This, however, does not influence the superconducting transition temperature and the transition width. In contrast, the a-axis film shows a broadened transition and a reduced T_c as already shown in Fig. 5.1. This behavior is related but not due to the growth direction, since as discussed before a-axis oriented growth is connected to deviations from oxygen stoichiometry.

On the other substrates the superconducting transition temperature in principle behaves similarly to the data described for SrTiO_3 . We had shown the results for films on Al_2O_3 already in Fig. 2.10 where also a temperature plateau of T_s for high and sharp transitions achievement was observed. The exact values depend on the actual substrate material. The upper value of T_s is determined by the onset of chemical reactions which start at grain boundaries since the zero resistance point is always affected much stronger than the onset temperature. The degradation at lower T_s is accompanied by growth deteriorations characterized by polycrystalline film formation and deviations from oxygen stoichiometry. Again, due to grain boundary formation, the completion temperature at lower T_s is more effectively depressed than the onset values.

As a last example we show in Fig. 5.3 a plot of T_c vs. T_s for films deposited on randomly oriented $\text{Zr}(\text{Y})\text{O}_2$ substrates. It is interesting to note that a high and sharp T_c here is obtained also at $T_s = 730^\circ\text{C}$, i.e. at conditions where a high degree of texture with the c-axis inclined to the substrate surface following the substrate surface orientation was observed. Degraded properties also with respect to the normal conduction [16] again coincide with polycrystalline phase formation at lower deposition temperatures.

Summarizing the T_c data we can conclude that for each investigated substrate material an optimum deposition temperature range exists where high T_c values and sharp transitions are achieved. In this temperature range c-axis textured growth is obtained and the zero resistance values of T_c are not strongly depending on the substrate material. Our best T_{c0} values determined in resistive measurements so far were 87, 89, 90, and 91 K on Al_2O_3 , MgO , ZrO_2 and SrTiO_3 , respectively.

Inductively determined transition temperatures [23] and other transport properties like the residual resistivity and especially the critical current density, J_c , however, closely are related to the growth quality of the films. Polycrystalline fractions in the films or wide mosaic distributions lead to property degradation.

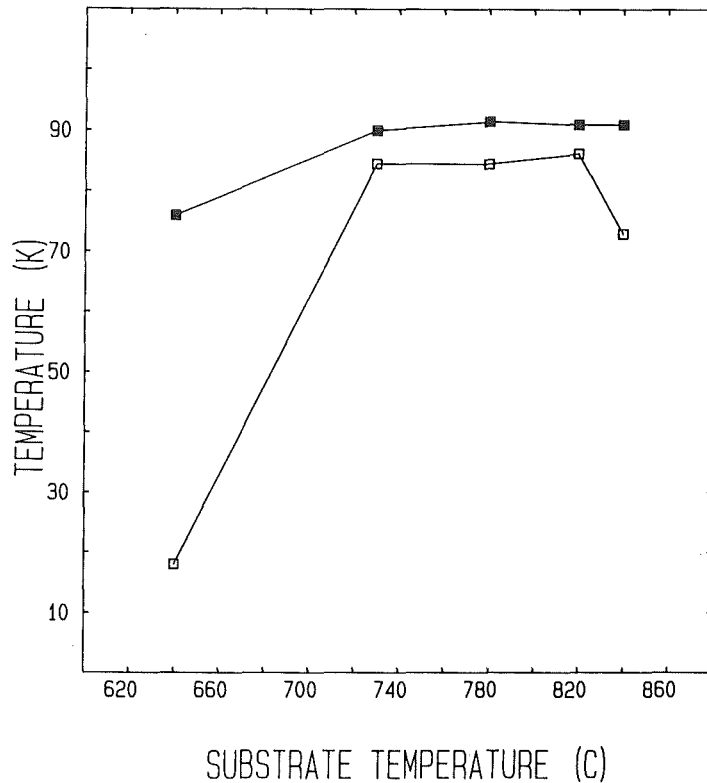


Fig. 5.3 Onset (filled symbols) and zero resistance (open symbols) values of YBaCuO thin films on randomly oriented Zr(Y)O₂ substrates as a function of the substrate temperature in the first deposition step.

The highest J_c values have been determined in epitaxial single crystalline films and qualitatively, the critical current density values in films on different substrates correlate with the widths of the mosaic distributions [65] shown in Fig. 3.10. As a demonstration we show critical current density measurements as a function of temperature in Fig. 5.4. The maximum values obtained at 77 K are $5.5 \cdot 10^6$, $9 \cdot 10^5$, $5 \cdot 10^5$ and $1 \cdot 10^3$ A/cm² for films on (100) oriented SrTiO₃ and MgO and on randomly oriented ZrO₂ and Al₂O₃, respectively. In the meantime a value of 2.0×10^6 A/cm² has been determined in a film on (100) oriented Zr(Y)O₂ substrate. The J_c values are directly related to the residual resistivity of the films as has been demonstrated for films prepared by different cooling procedures on (100) SrTiO₃ substrates [66]. The lower J_c value of $3 \cdot 10^5$ A/cm² for the (110)/(013) oriented film on (110)SrTiO₃ as compared to the $5.5 \cdot 10^6$ A/cm² for the film on (100)SrTiO₃ is in accordance with this observation.

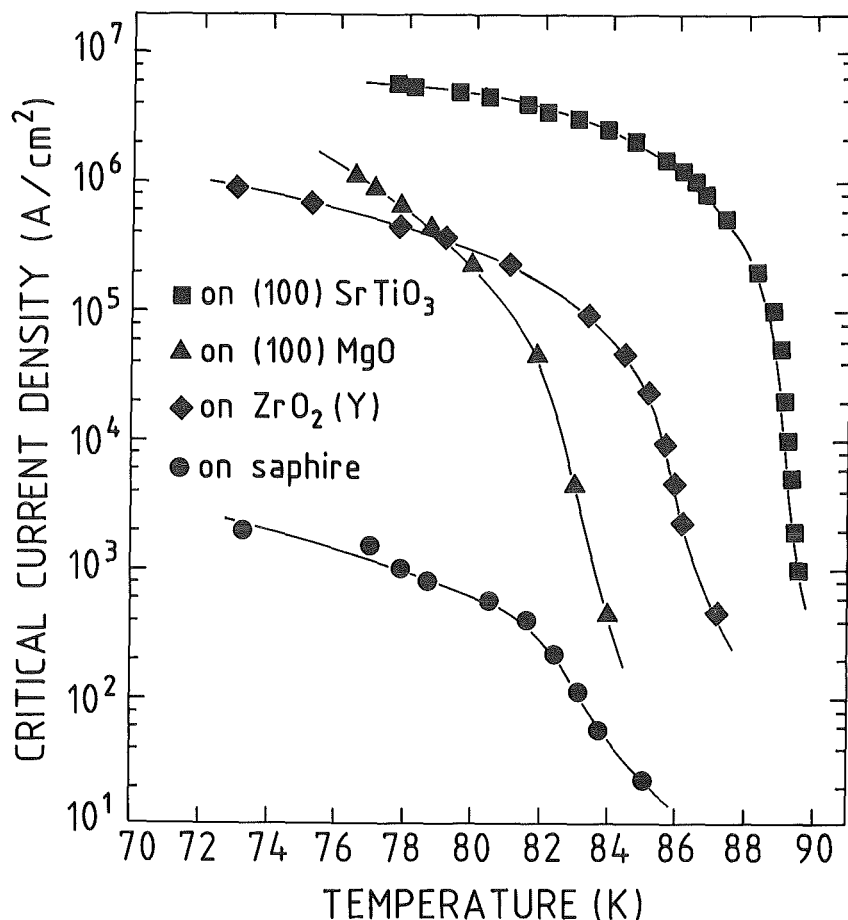


Fig. 5.4 Critical current densities measured in zero magnetic field versus temperature for YBaCuO thin films deposited on different substrates. The curves through the data points are guides to the eye.

5.2 Superconducting properties of ultrathin films

The superconducting properties of crystalline ultrathin films with thicknesses below 10 nm which had been deposited on carefully prepared and characterized (100) SrTiO₃ and MgO surfaces could be studied after an in situ deposition of a 30-50 nm thick amorphous protection layer [31]. As an example normalized resistivities (vs. temperature) are shown in Fig. 5.5 for films deposited on SrTiO₃ having different thicknesses. It can be seen that metallic behaviour and full superconductivity though achieved in broadened transitions occurs down to thicknesses of 3 nm. Thinner films reveal temperature activated conductivity and only partial superconductivity. This does not appear as an intrinsic property of the material but probably is due to inhomogeneities in the films like grain boundaries characterized by a distorted structure and inhibiting a continuous superconducting path through the film in a resistive measurement. In one

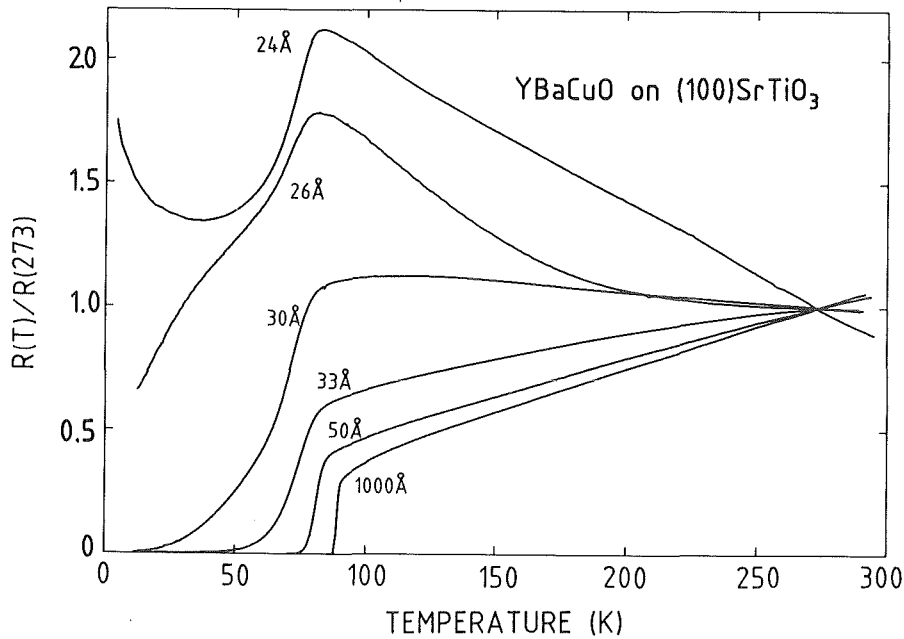


Fig. 5.5 Normalized resistance, $R(T)/R(273)$, versus temperature plots for ultra-thin YBaCuO films on (100) SrTiO₃. Full superconductivity above 4.2 K is observed for films with thicknesses down to 3 nm.

exceptional film of 2 nm thickness, however, metallic behaviour and full superconductivity was observed indicating that under optimum conditions the growth of very thin films still can be improved.

The conductivity at 273 K, the resistance ratio, $R(273)/R(100)$, and the transition temperatures are compared for films on SrTiO₃ and MgO as a function of film thickness in Fig. 5.6. It can be seen that the abrupt decrease of T_{c0} for films on SrTiO₃ coincides with the change of the resistivity ratio from above to below 1. This is in agreement with a model of superconducting grains surrounded by degraded material as discussed above. The deteriorations of the transport properties of films on MgO start at larger thicknesses (about 3 nm shift) as compared to those on (100)SrTiO₃. This differences may be explained by the growth behaviour analyzed by channeling experiments as discussed in chapter 4. The large lattice mismatch between YBaCuO and MgO causes extreme strain at the substrate-film interface which is immediately relieved by the formation of misfit dislocations. Such a layer may have a thickness of a few nm and degraded superconducting properties leading to a breakdown of superconducting paths at larger thicknesses than on SrTiO₃ where strained but commensurate growth is favoured by the superior lattice matching. A study of the fluctuation-enhanced conductivity above T_c in the ultrathin-films [31] in terms of the Aslamazov-

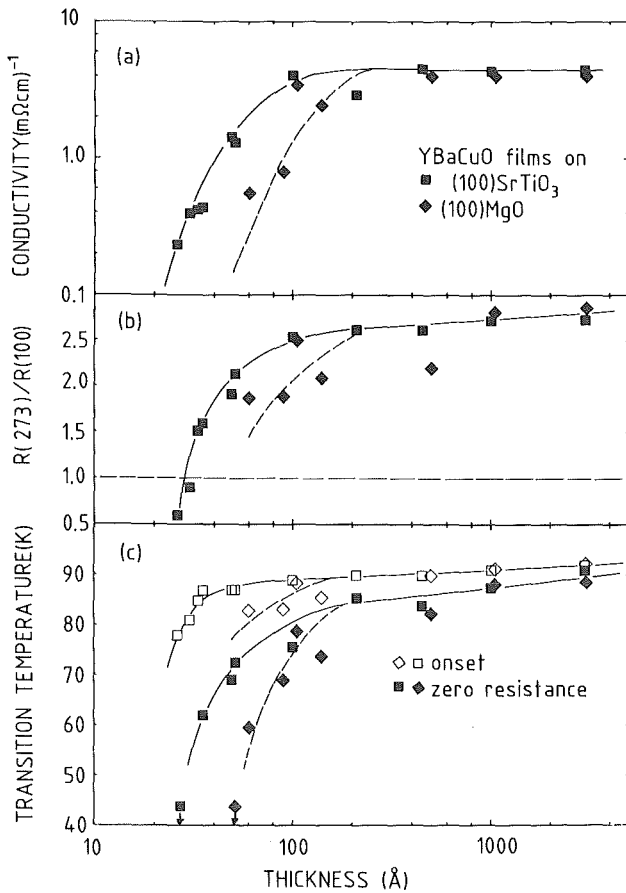


Fig. 5.6 Conductivity (a), resistance ratio, $R(273)/R(100)$ (b), and onset and zero resistance values of superconducting transition curves (c) in thin and ultra-thin YBaCuO films on (100) SrTiO₃ and (100) MgO substrates. The degradation of properties starts on MgO at larger thicknesses as compared to films on SrTiO₃ due to differences in the initial state of growth.

Larkin theory [67] revealed three-dimensional behavior in films with thicknesses of only two or three unit cells. These results prove experimentally the short coherence length in the 1-2-3 compounds along the c-direction.

5.3 Electron tunneling

Over the last 30 years of research in traditional superconductivity electron tunneling has become recognized as an important tool for studying superconducting properties. After Giaver [68] discovered the superconducting tunneling effect as a method for the determination of the superconducting density of states in 1960 McMillan and Rowell [69] established electron tunneling as a spectroscopic method for the determination of the electron coupled phonon spectrum and gave the first detailed proof for the validity of the Eliashberg gap equations [70]. For the traditional superconductors these equations describe the dependence of the superconducting properties on the details of the electron-coupled-phonon-spectrum and on the Coulomb repulsion of the conduction

electrons. With the discovery of the high T_c superconductors the tunneling experimenter is starting again from the beginning as the coupling mechanism is not known till now and hence a microscopic theory is not established for these new materials. Thus it is even not clear at present if the superconducting density of states determined by tunneling in principle can ever provide that detailed information on the microscopic superconducting mechanism as it was the case for the traditional electron-phonon-coupled superconductors. Due to these uncertainties we have avoided in the following presentation and discussion as far as possible the terminology originating from the traditional superconductors and replaced it by more generic expressions. E.g., instead of "energy gap" we use the designation "gaplike structure". This expression remains correct for the case that the HTCS' might exhibit an energy gap in a type of BCS density of states or that in future it will turn out that e.g. the true coupling mechanism is that proposed by Anderson [71]. For the tunneling density of states that would substitute a usual energy gap by a sequence of excitation structures caused by spinons and holons [71]. The latter example characterizes the typical present difficulties in the interpretation of HTSC tunnel data from the theoretical point of view.

The most serious experimental problem involved in the tunneling method is the small sampling depth which is of the order of a coherence length i.e. about 20 Å, for most of the interesting superconductors. Only in the case of the simple s-p metals, the coherence length is large, e.g. 1000 Å. Obviously, a small sampling depth makes high demands on the material quality of the superconductor itself and on the interface region between the superconductor and the tunnel barrier. For the 1-2-3 material group, e.g., $Y_1Ba_2Cu_3O_7$ from critical field measurements a coherence length of about 3 Å is deduced in the direction of the c-axis whereas for directions parallel to the a-b plane about 30 Å are found. Thus the a-b plane coherence length is comparable to that of conventional superconductor compounds and has encouraged us to study the HTSC by tunneling experimental procedures analogous to those which proved successful for the conventional superconductors. In the following we present tunneling results on $Y_1B_2Cu_3O_7$ films prepared on $SrTiO_3$ single crystals with two different orientations, the [001] and the [110]-directions perpendicular to the film plane.

The films of $Y_1Ba_2Cu_3O_7$ were prepared by reactive magnetron sputtering using an inverted cylindrical magnetron sputtering head under the standard sputtering conditions described in chapter 2. As substrate material mostly (110) oriented single crystals of $SrTiO_3$ were used on which the films grew up in the mixed (110)/(013) orientation. After the second preparation step the samples were not passed through a special treatment for the fabrication of the tunnel barrier.

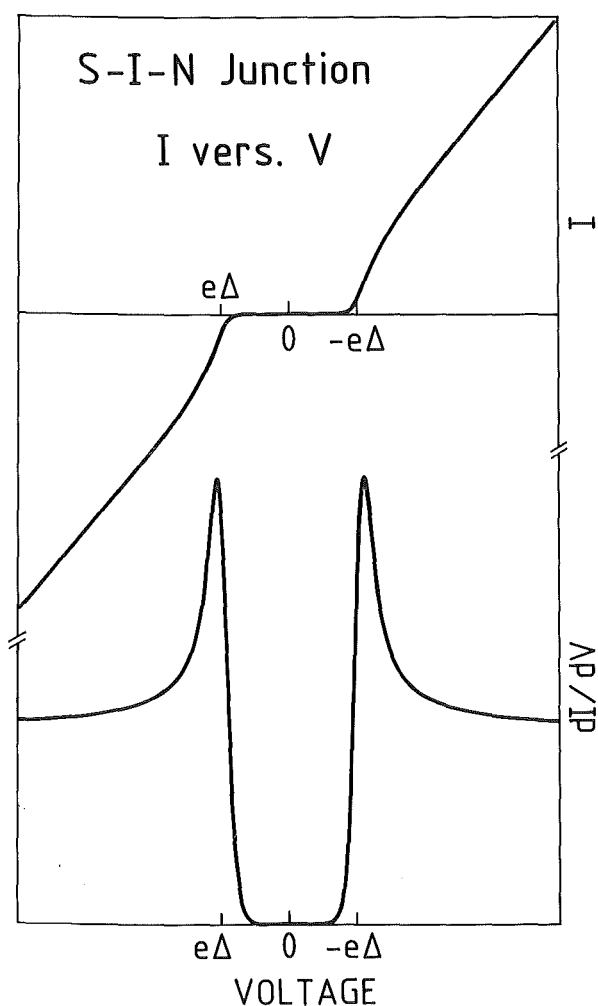


Fig. 5.7
The figure illustrates the electrical measurements taken on a conventional superconductor-isolator-normal conductor tunnel-junction in a tunneling spectroscopy experiment. The upper part shows a typical I-V characteristic and the lower part the dynamic conductivity dI/dV versus voltage reflecting the shape of the superconducting density of states.

Probably a natural oxide builds up on the films during cooling to room temperature at the end of that step. Pb or In were used as counter electrodes. In the case of Pb counter electrodes the samples were taken out of the sputtering system and painted in the usual way with an insulator varnish to define the tunneling area of $1-5 \text{ mm}^2$. Then a separate evaporation chamber was used to deposit the Pb films. In the course of this fabrication procedure the film surface is exposed to ambient air for about 10 min. In the case of the In counter electrodes the junctions were completed in an alternative way: After cooling to room temperature the magnetron system was strongly floated with dry oxygen or nitrogen to prevent ambient air and humidity from contaminating the film surface. Then small cuts from 0.5 mm diameter In wire were pressed onto the film surface to form the counter electrode of a tunnel junction.

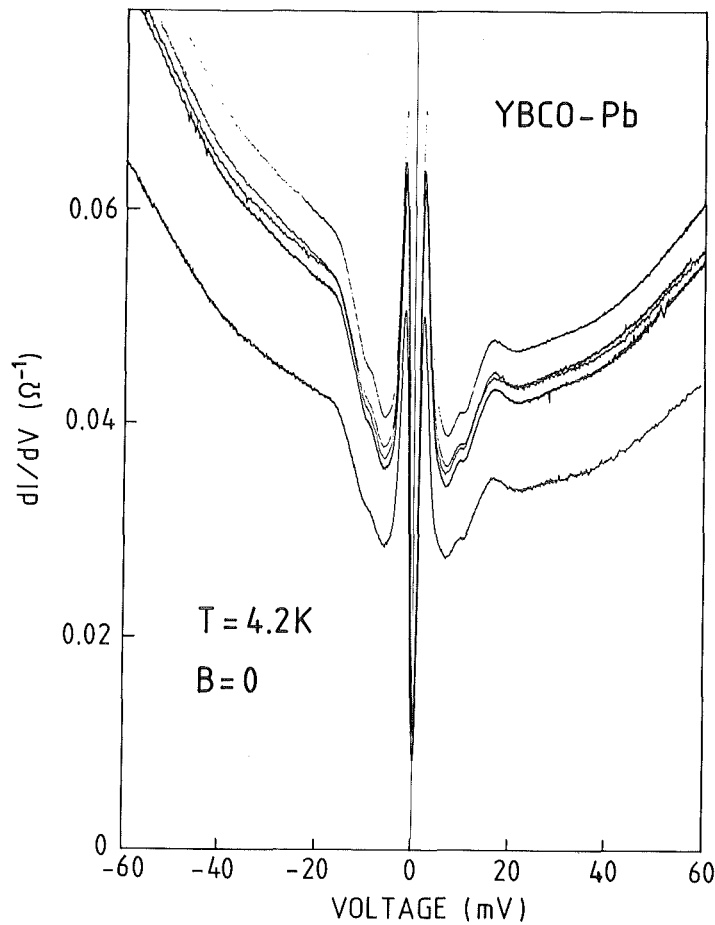


Fig. 5.8 dI/dV vs. V of 5 different junctions of the type YBaCuO-Pb. The YBaCuO-films are grown on (110) oriented SrTiO₃.

We are used to illustrate our results in the derivative kind of presentation because the first derivative dI/dV of the current voltage characteristic of the tunnel diode is directly related to the density of states of the electrodes. In Fig. 5.7 we demonstrate schematically the current-voltage and the dI/dV trace of a tunnel diode with one electrode in the superconducting state with the energy gap Δ . The superconducting density of states $N(E)$ is extracted from tunnel data by normalizing the superconducting to the normal state following the formula $N(E) = (dI/dV|_s)/(dI/dV|_n)$. We further remark, that most of the tunneling results described in the following are published in great detail in ref. 72.

In Fig. 5.8 we show the dI/dV versus V traces of five junctions of the type YBCO-Pb prepared in one run. The Pb films are in the superconducting state, and we observe at ± 11 mV the phonon induced structures of the longitudinal Pb phonons. Between +20 mV and -20 mV we see in all the junctions an interesting

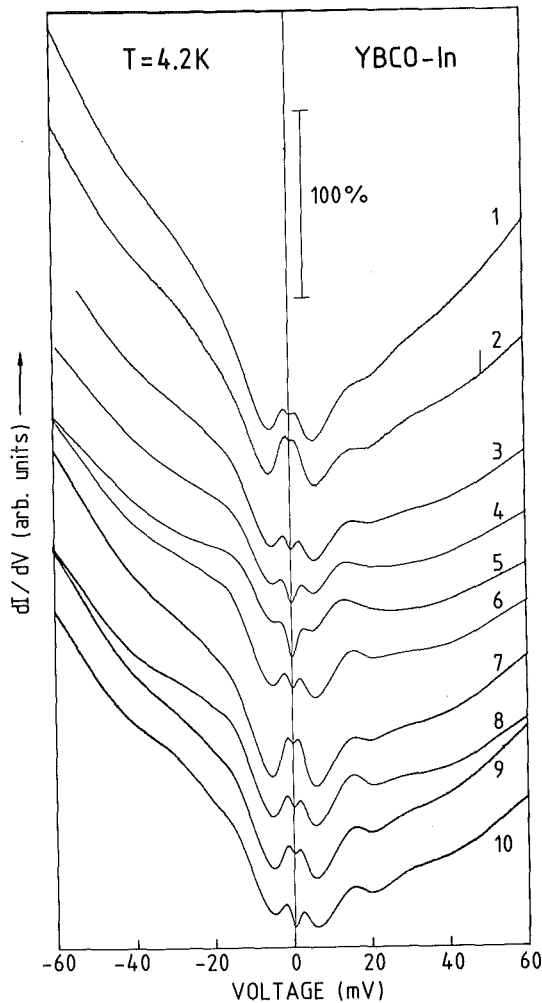


Fig. 5.9
 dI/dV vers. V for 10 different junctions of the type YBaCuO-In (cut). The traces were all normalized to the same vertical scale, which is the relative change in tunneling conductance. The bar marks a change in 100%.

feature which forms a gap like dip and which we attribute to the YBCO material. To this gap-like structure (GLS) we will focus our attention in the following. In Fig. 5.9 we present tunnel data taken on junctions formed by the In cuts. From the 10 junctions shown in Fig. 5.9 the junctions No. 1 and No. 2 were prepared on films grown on (100) SrTiO₃ substrates, all the other traces are from (110)/(013) oriented films. We observe no superconducting features of the In counter electrode as at this temperature In is in the normal state. On all the junctions we see the GLS between +20 mV and -20mV and that it is very similar to that one of Fig. 5.8. In ref. 72 we have presented strong experimental arguments that the GLS is caused by a density-of-states effect of the the Y₁Ba₂Cu₃O₇ electrode and not by other tunneling effects, e.g. inelastic tunneling, which can generate similar structures in the first derivative traces. Furthermore we could demonstrate that the GLS is reflecting a density of states effect of

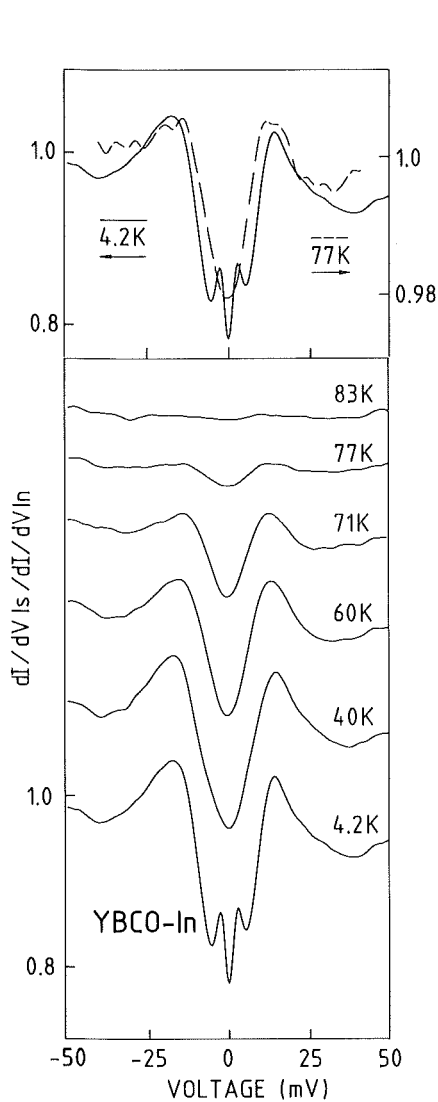


Fig. 5.10

Lower part: Normalized conductance traces (the conductance in the superconducting state of the YBaCuO film is normalized to the conductance measured in the normal state of the film) for different temperatures. The zero resistance of the resistive transition is at 86 K. Upper part: Comparison of the shape of the normalized conductance traces measured at 4.2 K (left scale) and at 77 K (right scale).

superconductive and not of semiconductive nature by following the temperature dependence. This is illustrated in Fig. 5.10 where we show conductance traces of junction No. 4 of Fig. 5.9 taken at different temperatures. To improve the visual clarity of the GLS especially at higher temperatures, the data shown in Fig. 5.10 were refined in two ways: First, all the measured dI/dV traces were normalized to the structureless background taken at 95 K where the $Y_1Ba_2Cu_3O_7$ film is in the normal state. Then these normalized data were unfolded with respect to the usual temperature broadening of the density of states tunneling experiment, which is a bell shaped curve with $3.5 kT$ half width (on a traditional superconductor such a refinement procedure would result in a set of BCS like density-of-states curves with an energy gap corresponding to the respective

temperature). We observe in Fig. 5.10, that the GLS is still clearly present at 77 K and disappeared near 83 K. The resistive T_c of the film was at 86 K.

In Fig. 5.9 we observe that most of the junctions show an additional structure at higher voltage between 30 and 40 mV. For the following comparison of our tunnel data with those of other experimenters we use the normalized data of a junction with no additional high energy structure (No. 5) and data representative for a strong additional structure (No. 10). Most of the tunneling studies on YBaCuO which show interesting gap-like features have used small area point contacts to fabricate the tunnel junction [73,74,75,76]. In all these experiments normal conductor tips were used as counter electrodes. Thus, an unambiguous proof of tunneling could not be made. The experimenters deduced energy gaps from their data ranging from 11.5-50 meV. We found that our GLS compares well to the data of Kirtley et al. [73]. In Fig. 5.11 we show our normalized data from

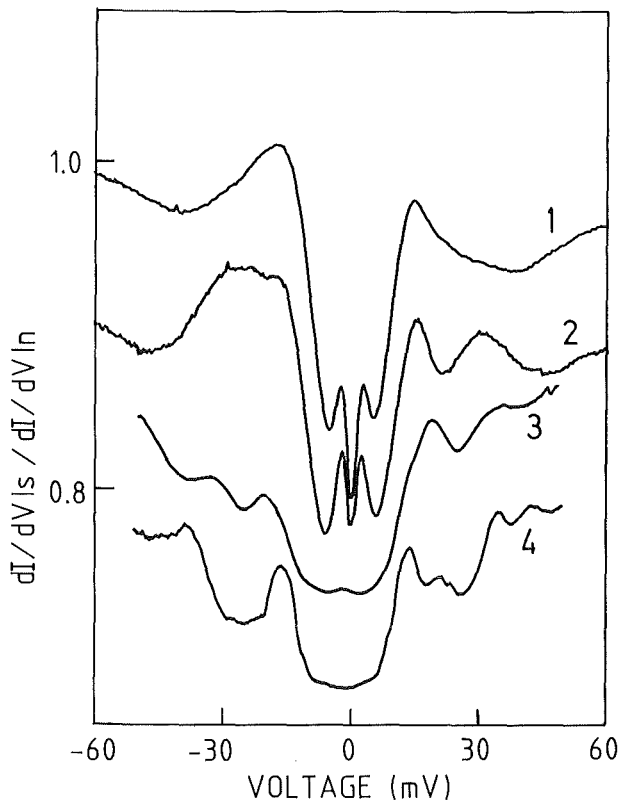


Fig. 5.11
Comparison of the normalized conductance data from junction No. 4 (trace 1) and junction No. 10 (trace 2) of Fig. 5.9 to dI/dV data of Kirtley et al. [73] obtained by point contact tunneling with the tip parallel to the c -axis (trace 3) and parallel to the a - b plane (trace 4).

junction No. 4 and No. 10 together with data which these authors obtained for the tip parallel to the c -axis (trace 3) and parallel to the a - b plane (trace 4). We see that the maxima in our curves at ± 16 meV agree very well with the data of

Kirtley et al. Trace 2 and 3 also show a remarkable similarity in the high energy structures near ± 30 mV.

Fournel et al [77] prepared tunnel junctions of the conventional type on single crystals of YBaCuO. They report that their junction area was oriented parallel to the a-b plane. In Fig. 5.12 we compare their result for the normalized density of states again with our results represented by junction No. 4 and No. 10. First of all we note, that the strength of the structure of Fournel et al. corresponds to a change in conductivity of 20%, similar to our structures. Furthermore, the shape of the structure of Fournel et al. is similar to that of junction No. 4 except that the voltage scales differ strongly. The peaks in their GLS are located near ± 30 mV and we observe that they are coinciding with the high energy structures of our junction No. 10. Two other results of Fournel et al. are similar to our data. Their GLS shown in Fig. 5.12 shows the same type of temperature dependence as our

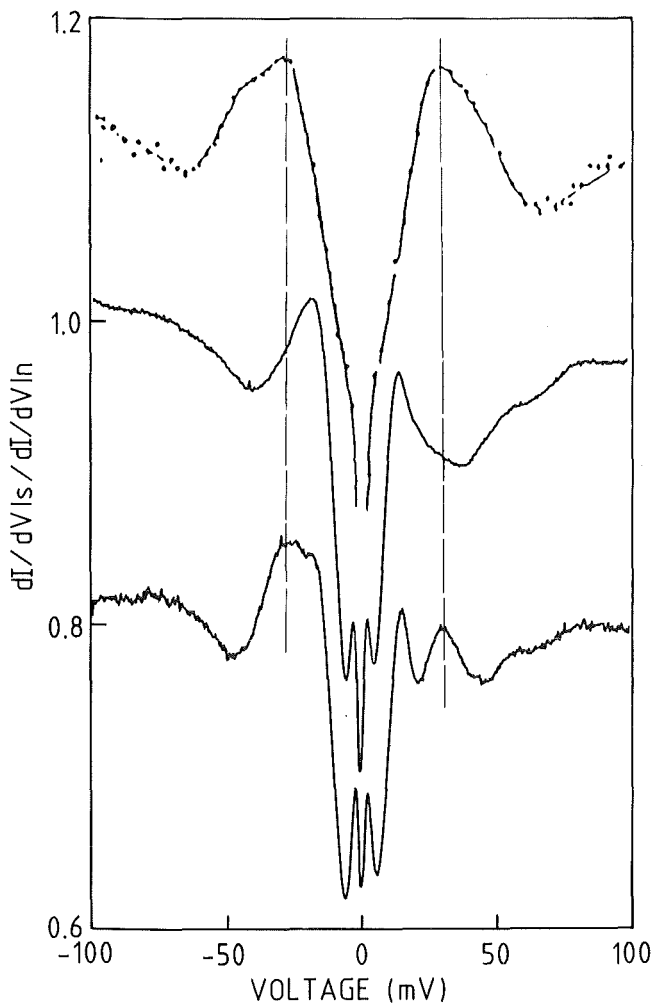


Fig. 5.12
Comparison of the normalized conductance data of Fournel et al. (upper data) to that of junction No. 4 (trace in the middle) and to that of junction No. 10 (lower trace). The vertical scale is valid also for the data of Fournel et al. [77].

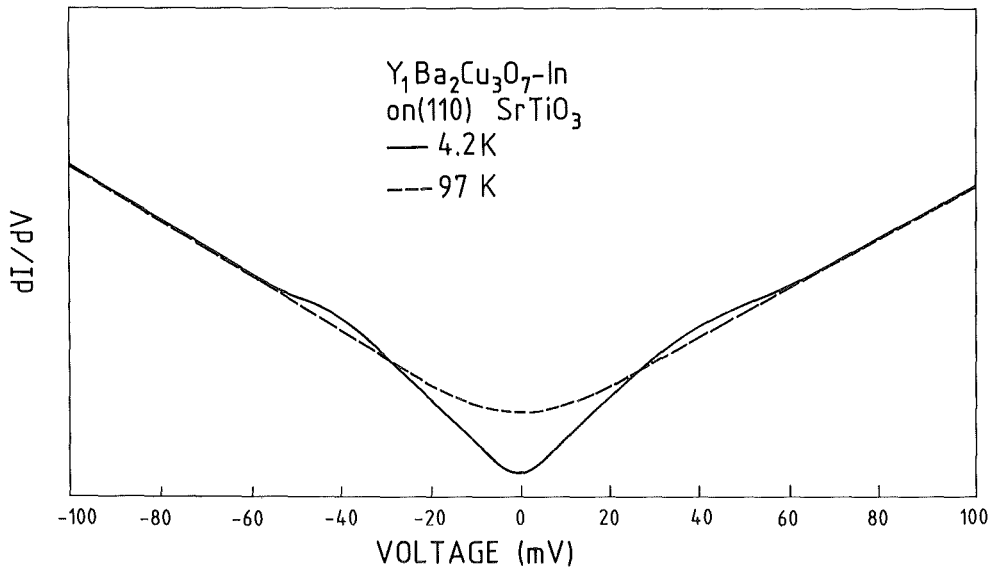


Fig. 5.13 Dynamic conductivity of an YBaCuO-isolator-In tunnel junction taken in the normal (97 K) and in the superconducting state of the YBaCuO film. The isolator is an artificial tunnel barrier of amorphous YBaCuO material.

GLS. The peak distance stays roughly constant till T_c is reached. Furthermore they also found a dip in conductivity at zero bias about 6 meV wide and strongly developing below 30 K.

The data of Fig. 5.12 suggest that in junctions of the type of No. 10 we measure a superposition of two GLS. This interpretation is supported by results we got from $Y_1Ba_2Cu_3O_7$ -In junctions where we used an artificial amorphous oxide of the 1-2-3 material as tunnel barrier. Most of these junctions were similar to those of Fig. 5.9 but two of them showed traces as illustrated in Fig. 5.13. We observe that the superconducting trace deviates from the strongly changing normal background by density of states peaks at about ± 35 mV and a drop in the density of states near zero bias. The normalized conductance data shown in Fig. 5.14 show already some resemblance in shape to those known from traditional superconductors and would propose for that case an energy gap of about 35 meV. We consider the data of Fig. 5.13 and 5.14 as a demonstration that it is possible to prepare junctions on $Y_1Ba_2Cu_3O_7$ films which show mainly the high energy GLS as found by Fournel et al. [77].

Clearly, the most intriguing question on which we have to focus in future is to clarify the origin of the two GLS. The first very often presented explanation is that the low energy (16 mV) GLS is measured on oxygen deficient material of a T_c of say only 40 K or 50 K present in the films. But this is clearly excluded by the

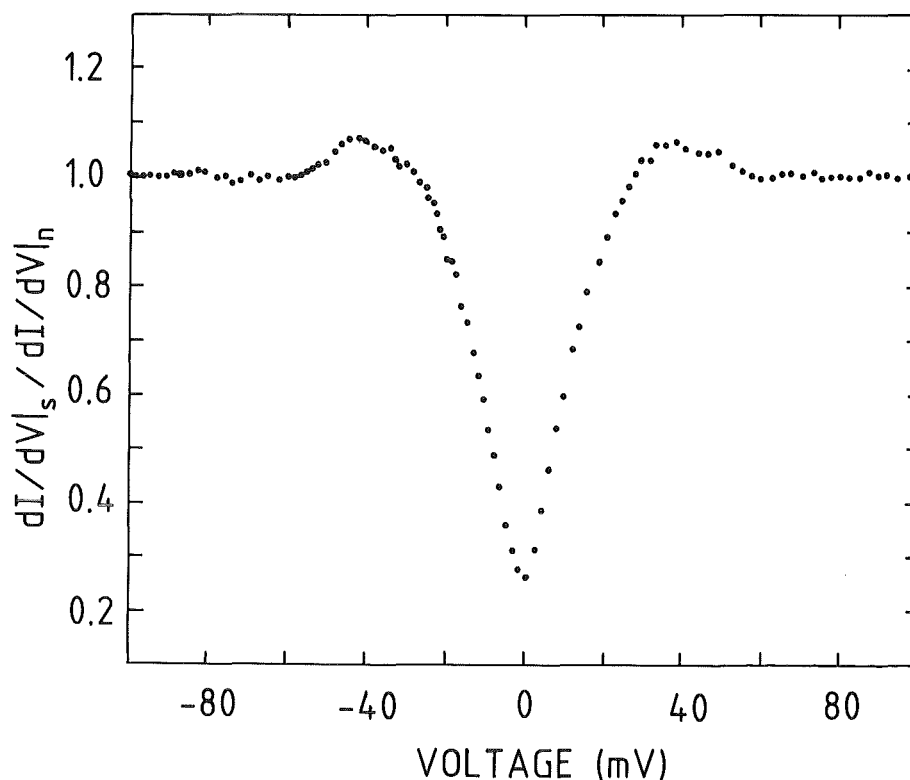


Fig. 5.14 Normalized conductance of the YBaCuO-In tunnel junction of Fig. 5.13.

data of Fig. 5.10 which show that the low energy GLS disappears near 83 K and not between 40 and 50 K. If the 16 meV GLS is due to degraded material at the film surface, then type of a proximity effect is needed to explain the high "gap vanishing" temperature of Fig. 5.10. On the traditional superconductors proximity effects were a quite common problem in tunneling experiments and caused gap structures which mostly appeared to be strongly smeared out to low energies but which did not show a sharp gap of e.g. half the value of that of the bulk of the film. If the comparably sharp GLS of Fig. 5.10 is really caused by a strong proximity effect then that would imply very special and also very reproducible conditions concerning the surface chemistry of the 1-2-3 material. In this case the results of Fig. 5.13 can be explained by an improvement of the quality of the material at the tunnel barrier-superconductor interface due to the artificial barrier.

Another explanation of two or even multiple GLS are anisotropy effects. We know from scanning electron microscopy that the surface roughness of our films exceeds by far the typical thickness of 20-30 Å of a tunnel barrier. In that case one

has to assume that the measured tunnel current represents some type of an average of the tunnel currents into the different crystalline directions [72]. The contribution of the different directions is given by the frequency of the corresponding crystalline planes on the film surface and by the thickness of the tunnel barrier on these planes. It is conceivable that especially in the case of the strongly anisotropic HTSC materials the oxidation chemistry is strongly different for different planes and thus provides a preference of the tunnel current to certain crystalline directions. This preference will certainly change if the tunnel barrier formation method is changed. In this way one can explain easily the different results of Fig. 5.9 and Fig. 5.13.

In conclusion, we have presented tunneling results on $Y_1Ba_2Cu_3O_7$ obtained from thin film junctions. The results show two gaplike structures which both compare well to results found by other groups on single crystals either by sandwich type junctions or by point contact spectroscopy. We have presented two scenarios based on special proximity effects or on directional tunneling to explain these results. A final decision could be made if precise density-of-states measurements by other experimental methods are available. The method of infrared absorption so far provides data which are much less detailed and which mostly lack the important condition of 100 percent reflectivity in the superconducting state at low frequencies. Recently the superconducting density of states of the 80 K superconductor $Bi_2Ca_1Sr_2Cu_2O_x$ has been measured for the first time by photoemission spectroscopy with the result of an energy gap near 30 meV [78]. Perhaps this method can also be applied to $Y_1Ba_2Cu_3O_7$ to clarify the origin of the two GLS.

ACKNOWLEDGEMENTS

The authors would like to thank their colleagues W.Y. Guan, M. Höbel, Q. Li, F. Ratzel, C. Schultheiss, R. Smithey, B. Strehlau, F. Weschenfelder and X.X. Xi who contributed significantly to the results presented in this review for a very pleasant and fruitful cooperation.

REFERENCES

- [1] J.G. Bednorz and K.A. Müller, *Z. Phys. B - Condensed Matter* **64** (1986) 189
- [2] P. Chaudhari, R.H. Koch, R.B. Laibowitz, T.R. McGuire and R.J. Gambino, *Phys. Rev. Lett.* **58** (1987) 2684
- [3] D. Dijkkamp, T. Venkatesan, X.D. Wu, S.A. Shaheen, N. Jisrawi, Y.M. Min-Lee, W.L. McLean and M. Croft, *Appl. Phys. Lett.* **51** (1987) 619
- [4] R. Bormann and J. Nölting, *Appl. Phys. Lett.* (in press)
- [5] K. Kishio, J. Shimoyama, T. Hasegawa, K. Kitazawa and K. Fueki, *J.J. Appl. Phys.* **26** (1987) L1228
- [6] N. Missert, R. Hammond, J.E. Mooig, V. Matijasevic, P. Rosenthal, T.H. Geballe, A. Kapitulnik and M.R. Beasley, *IEEE Trans. Mag.* **25** (1988) 2418
- [7] T. Terashima, K. Iijima, K. Yamamoto, Y. Bando and H. Mazaki, *J.J. Appl. Phys.* **27** (1988) L91
- [8] D.D. Berkley, B.R. Johnson, N. Anand, K.M. Beauchamp, L.E. Conroy, A.M. Goldman, J. Maps, K. Mauersberger, M.L. Mecartney, J. Morton, M. Tuominen and Y.-J. Zhang, *Appl. Phys. Lett.* **53** (1988) 1973
- [9] P. Berberich, J. Tate, W. Dietsche and H. Kinder, *Appl. Phys. Lett.* **53** (1988) 925
- [10] M.R. Scheuermann, C.C. Chi, C.C. Tsuei, D.S. Yee, J.J. Cuomo, R.B. Laibowitz, R.H. Koch, B. Braren, R. Srinivasen and M.M. Plechaty, *Appl. Phys. Lett.* **51** (1987) 1951
- [11] N.D. Westwood, *MRS Bulletin* **13** (1988) 47
- [12] Y. Shintani, K. Nakanishi, T. Takawaki and O. Tada, *J.J. Appl. Phys.* **14** (1975) 1875
- [13] C. Plog and W. Gerhard, *Z. Phys. B* **54** (1983) 71
- [14] R.L. Sandstrom, W.J. Gallagher, T.R. Dinger, R.B. Laibowitz and R.J. Gambino, *Appl. Phys. Lett.* **53** (1988) 44
- [15] H. Koinuma, M. Kawasaki, S. Nagata, K. Takeuchi and K. Fueki, *J.J. Appl. Phys.* **27** (1988) L376
- [16] J. Geerk, X.X. Xi, H.C. Li, W.Y. Guan, P. Kus, M. Höbel, G. Linker, O. Meyer, F. Ratzel, C. Schultheiss, R. Smithey, B. Strehlau and F. Weschenfelder, *Int. J. Mod. Phys. B*, in press
- [17] B. Feldman, private communication
- [18] H.C. Li, G. Linker, F. Ratzel, R. Smithey and J. Geerk, *Appl. Phys. Lett.* **52** (1988) 1098

- [19] M.J. Cima, J.S. Schneider and S.C. Peterson, *Appl. Phys. Lett.* **53** (1988) 710
- [20] G. Linker, X.X. Xi, O. Meyer, Q. Li and J. Geerk, *Solid State Commun.* **69** (1989) 249
- [21] Q. Li, F. Weschenfelder, O. Meyer, X.X. Xi, G. Linker and J. Geerk, *J. Less Common Met.* **151** (1989) 295
- [22] M.A. Beno, L. Soderholm, D.W. Capone II, D.G. Hinks, J.D. Jorgensen, I.K. Schuller, C.U. Segre, K. Zhang, J.D. Grace, *Appl. Phys. Lett.* **51** (1987) 57
- [23] X.X. Xi, G. Linker, O. Meyer, E. Nold, B. Obst, F. Ratzel, R. Smithey, B. Strehlau, F. Weschenfelder and J. Geerk, *Z. Phys. B - Condensed Matter* **74** (1989) 13
- [24] Y. Bando, T. Terashima, K. Iijima, K. Yamamoto, K. Hirata and H. Mazaki, 5th Int. Workshop on Future Electron Devices - High Temperature Superconducting Electron Devices, June 2-4, Miyagi-Zao (1988) p. 11
- [25] A. Kapitulnik, *Physica C* **153-155** (1988) 520
- [26] H. Kajikawa, T. Hase, K. Nishimura, M. Okuda, T. Nakatsuka and Y. Kawate, 5th Int. Workshop on Future Electron Devices - High Temperature Superconducting Electron Devices, June 2-4, Miyagi-Zao (1988) p. 95
- [27] J. Fujita, T. Yoshitaka, A. Kamijo, T. Satoh and H. Igarashi, *J. Appl. Phys.* **64** (1988) 1292
- [28] J.A. Edwards, R.G. Humphreys, N.G. Chew and J.S. Satchell, *J. Phys. C: Solid State Phys.:* **21** (1988) L1055
- [29] M. Tonouchi, Y. Yoshizako, M. Iyori and T. Kobayashi, 5th Int. Workshop on Future Electron Devices - High Temperature Superconducting Electron Devices, June 2-4, Miyagi-Zao (1988) p. 68
- [30] G. Linker, X.X. Xi, O. Meyer, Q. Li and J. Geerk, *J. Less-Common Met.* **151** (1989) 357
- [31] X.X. Xi, J. Geerk, G. Linker, Q. Li and O. Meyer, *Appl. Phys. Lett.*, **54** (1989) 2367
- [32] Q. Li, O. Meyer, X.X. Xi, J. Geerk and G. Linker, *Appl. Phys. Lett.*, July 1989
- [33] *Channeling Theory, Observation and Applications*, D.V. Morgan ed., Wiley and Sons, London (1973)
- [34] D.S. Gemmel, *Rev. Mod. Phys.* **14** (1984) 129
- [35] R. Sizmann and C. Varelas, *Festkörperprobleme XVII* (1977) 261

- [36] W.K. Chu, J.W. Mayer and M.-A. Nicolet, Backscattering Spectrometry, Academic Press, N.Y. (1978)
- [37] L.C. Feldman, J.W. Mayer and S.T. Picraux, Materials Analysis by Ion Channeling, Academic Press, N.Y. (1982)
- [38] S.T. Picraux, L.R. Dawson, J.Y. Tsuo, B.L. Doyle and S.R. Lee, Nucl. Instr. Meth. B **33** (1988) 891
- [39] Y. Quéré, Phys. Stat. Sol. **30** (1968) 713
- [40] J. Lindhard, Phys. Lett. **12** (1964) 126
- [41] G. Molière, Z. Naturforschung **2A** (1947) 142
- [42] J.H. Barrett, Phys. Rev. B **3** (1971) 1527
- [43] M.L. Swanson, in Advanced Techniques for Characterizing Microstructures, F.W. Wiffen and J.A. Spitznagel eds., Metall. Soc. of AIME, NY (1982) p. 305
- [44] O. Meyer and A. Turos, Materials Science Rep. **2** (1987) 417
- [45] R. Kaufmann and O. Meyer, Phys. Rev. **28** (1983) 6216
- [46] O. Meyer, R. Kaufmann, B.R. Appleton and M. Chang, Solid State Commun. **39** (1981) 825
- [47] R.P. Sharma, L.E. Rehn, P.M. Baldo and J.Z. Liu, Phys. Rev. B **38** (1988) 9287
- [48] D.V. Morgan and D. van Vliet, Can. J. Phys. **46** (1968) 503
- [49] C. Lehmann and G. Leibfried, Z. Phys. **172** (1963) 465
- [50] O. Meyer, F. Weschenfelder, X.X. Xi, G.C. Xiong, G. Linker and J. Geerk, Nucl. Instr. Meth. B **35** (1988) 292
- [51] J. Hutton and R.J. Nelson, Acta Cryst. A **37** (1984) 916
- [52] T.O. Baldwin and C.W. Tompson, J. Chem. Phys. **41** (1964) 1420
- [53] M. Berti, A.V. Drigo, C. Cohen, J. Siejka, M.M. Tosic, Nucl. Instr. Meth. **199** (1982) 605
- [54] D. Steele and B.E.F. Fender, J. Phys. C: Solid State Phys. **7** (1974) 1
- [55] M. Tomita, T. Hayashi, H. Takaoka, Y.I. Shii, Y. Enomoto and T. Murakami, J. J. Appl. Phys. **27** (1988) L636
- [56] N.G. Stoffel, P.A. Morris, W.A. Bonner and B.J. Wilkens, Phys. Rev. B **37** (1988) 2297
- [57] H.W. Zandbergen and G. Thomas, phys. stat. sol. a **107** (1988) 825
- [58] B. Domenges, H. Hervieu, C. Michel and B. Raveau, Europhys. Lett. **4** (1987) 211
- [59] E.A. Hewat and J.C. Villegier, private communication
- [60] Y. Matsui, E. Takayama-Muramachi and K. Kato, J.J. of Appl. Phys. **27** (1988) L350

- [61] A.F. Marshall, R.W. Barton, K. Chat, A. Kapitulnik, B. Oh and R.H. Hammond, *Phys. Rev. B* **37** (1987) 9353
- [62] C.H. Chen, J. Kwo and M. Hong, *Appl. Phys. Lett.* **52** (1988) 841
- [63] N.P. Ong, Z.Z. Wang, S. Hagen, T.W. Jing, J. Clayhold and J. Horvath, *Physica C* **153-155** (1988) 1072
- [64] B. Batlogg, T.T.M. Palstra, L.F. Schneemeyer, R.B. van Dover and R.J. Cava, *Physica C* **153-155** (1988) 1062
- [65] J. Geerk, Q. Li, G. Linker, O. Meyer, X.X. Xi, Workshop: "Problems and Prospects of the Critical Current of New High T_c Superconductors", International Superconductivity Technology Center, Tokyo, Febr. 1-3 (1989) p. 67
- [66] X.X. Xi, G. Linker, O. Meyer and J. Geerk, *J. Less Common Met.* **151** (1989) 349
- [67] L.G. Aslamazov and A.I. Larkin, *Phys. Lett.* **26A** (1968) 238
- [68] I. Giaver, *Proceedings 7th Int. Conference Low Temp. Physics, Toronto, 1960*, Univ. of Toronto Press (1961) p. 327
- [69] W.L. McMillan and J.M. Rowell, *Phys. Rev. Lett.* **14** (1965) 108
- [70] G.M. Eliashberg, *Sov. Phys. JETP* **11** (1960) 696
- [71] P.W. Anderson, *Physica C* **153-155** (1988) 527
- [72] J. Geerk, X.X. Xi and G. Linker, *Z. Phys. B - Condensed Matter* **73** (1988) 329
- [73] J.R. Kirtley, R.T. Collins, Z. Schlesinger, W.J. Gallagher, R.L. Sandstrom, T.R. Dinger and D.A. Chance, *Phys. Rev.* **B35** (1987) 8846
- [74] M.F. Crommie, L.C. Bourne, A. Zettl, M.L. Cohen and A. Stacy, *Phys. Rev.* **B35** (1987) 8853
- [75] M.D. Kirk, D.P.E. Smith, D.B. Mitzi, J.Z. Sun, D.J. Webb, K. Char, M.R. Hann, M. Naito, B. Oh, M.R. Beasley, T.H. Geballe, R.H. Hammond, A. Kapitulnik and C.F. Quate, *Phys. Rev.* **B35** (1987) 8850
- [76] P.J.M. van Bentum, L.E.C. van de Leemput, L.W.M. Scheurs, P.A.A. Teunissen and H. van Kempen, *Phys. Rev.* **B36** (1987) 843
- [77] A. Fournel, I. Oujia, J.P. Sorbier, H. Noel, J.C. Levet, M. Potel and P. Gougeon, *Europhys. Lett.* **6** (1988) 653
- [78] J.-M. Imer, F. Patthey, B. Dardel, W.-D. Schneider, Y. Baer, Y. Petroff and A. Zettl, *Phys. Rev. Lett.* **62** (1989) 336
- [79] O. Meyer, B. Egner, J. Geerk, R. Gerber, G. Linker, F. Weschenfelder, X.X. Xi and G.C. Xiong, *Nucl. Instr. Meth.* **B37/38** (1989) 917